

4/11/91

**NANOCOMPOSITES FOR ELECTRONIC APPLICATIONS**

**Period January 1, 1990 thru December 31, 1991**

**AD-A267 073**  


**FINAL REPORT**

**Volume III**

**OFFICE OF NAVAL RESEARCH**

**Contract No. N00014-90-J-1558**

**APPROVED FOR PUBLIC RELEASE - DISTRIBUTION UNLIMITED**

**Reproduction in whole or in part is permitted for any purpose  
of the United States Government**

**L. Eric Cross**

**DTIC  
SELECT  
JUL 22 1993  
S B D**

**PENNSSTATE**



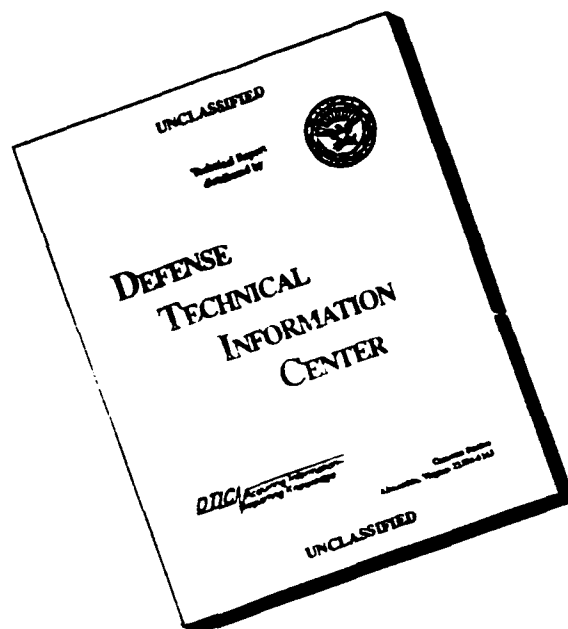
**THE MATERIALS RESEARCH LABORATORY  
UNIVERSITY PARK, PA**

**93 7 21 043**

**93-16532**

 5880

# DISCLAIMER NOTICE



THIS DOCUMENT IS BEST  
QUALITY AVAILABLE. THE COPY  
FURNISHED TO DTIC CONTAINED  
A SIGNIFICANT NUMBER OF  
PAGES WHICH DO NOT  
REPRODUCE LEGIBLY.



## GENERAL INSTRUCTIONS FOR COMPLETING SF 298

The Report Documentation Page (RDP) is used in announcing and cataloging reports. It is important that this information be consistent with the rest of the report, particularly the cover and title page. Instructions for filling in each block of the form follow. It is important to *stay within the lines* to meet optical scanning requirements.

**Block 1. Agency Use Only (Leave blank).**

**Block 2. Report Date.** Full publication date including day, month, and year, if available (e.g. 1 Jan 88). Must cite at least the year.

**Block 3. Type of Report and Dates Covered.** State whether report is interim, final, etc. If applicable, enter inclusive report dates (e.g. 10 Jun 87 - 30 Jun 88).

**Block 4. Title and Subtitle.** A title is taken from the part of the report that provides the most meaningful and complete information. When a report is prepared in more than one volume, repeat the primary title, add volume number, and include subtitle for the specific volume. On classified documents enter the title classification in parentheses.

**Block 5. Funding Numbers.** To include contract and grant numbers; may include program element number(s), project number(s), task number(s), and work unit number(s). Use the following labels:

C - Contract	PR - Project
G - Grant	TA - Task
PE - Program Element	WU - Work Unit Accession No.

**Block 6. Author(s).** Name(s) of person(s) responsible for writing the report, performing the research, or credited with the content of the report. If editor or compiler, this should follow the name(s).

**Block 7. Performing Organization Name(s) and Address(es).** Self-explanatory.

**Block 8. Performing Organization Report Number.** Enter the unique alphanumeric report number(s) assigned by the organization performing the report.

**Block 9. Sponsoring/Monitoring Agency Name(s) and Address(es).** Self-explanatory.

**Block 10. Sponsoring/Monitoring Agency Report Number.** (If known)

**Block 11. Supplementary Notes.** Enter information not included elsewhere such as: Prepared in cooperation with...; Trans. of...; To be published in... When a report is revised, include a statement whether the new report supersedes or supplements the older report.

**Block 12a. Distribution/Availability Statement.** Denotes public availability or limitations. Cite any availability to the public. Enter additional limitations or special markings in all capitals (e.g. NOFORN, REL, ITAR).

DOD - See DoDD 5230.24, "Distribution Statements on Technical Documents."  
DOE - See authorities.  
NASA - See Handbook NHB 2200.2.  
NTIS - Leave blank.

**Block 12b. Distribution Code.**

DOD - Leave blank.  
DOE - Enter DOE distribution categories from the Standard Distribution for Unclassified Scientific and Technical Reports.  
NASA - Leave blank.  
NTIS - Leave blank.

**Block 13. Abstract.** Include a brief (*Maximum 200 words*) factual summary of the most significant information contained in the report.

**Block 14. Subject Terms.** Keywords or phrases identifying major subjects in the report.

**Block 15. Number of Pages.** Enter the total number of pages.

**Block 16. Price Code.** Enter appropriate price code (*NTIS only*).

**Blocks 17. - 19. Security Classifications.** Self-explanatory. Enter U.S. Security Classification in accordance with U.S. Security Regulations (i.e., UNCLASSIFIED). If form contains classified information, stamp classification on the top and bottom of the page.

**Block 20. Limitation of Abstract.** This block must be completed to assign a limitation to the abstract. Enter either UL (unlimited) or SAR (same as report). An entry in this block is necessary if the abstract is to be limited. If blank, the abstract is assumed to be unlimited.

## ABSTRACT

This document is the final report of work on the DARPA sponsored University Research Initiative (URI) on the subject "Nanocomposites for Electronic Applications" funded under ONR Contract No. N00014-90-J-1558. Initial funding on the contract was for a three year period from 1987-1990. This document is the final report for the two year extension period finishing on December 31, 1991.

Work on this program and associated studies on the ONR program on "Piezoelectric and Electrostrictive Materials for Transducer Applications" has led to a significantly improved understanding of the fundamental mechanisms in Relaxor Ferroelectrics. For the perovskite Lead Magnesium Niobate which is the prototype for many other relaxor perovskites, the self limiting nonstoichiometric ordering of Mg/Nb ions is shown to be the symmetry breaking key to the onset of micropolar regions at the Burns temperature well above the dielectric maximum. The simple paraelectric behavior at high temperature is shown to be modified by cooperation on cooling, leading to a Vogel:Fulcher type condensation into a glass like state at low temperature.

Many tungsten bronze structure ferroelectrics e.g.  $\text{Sr}_{1-x}\text{Ba}_x\text{Nb}_2\text{O}_6$  also show relaxor ferroelectric behavior, and in the lead barium niobate family of solid solutions there is a particularly rich panoply of behaviors. Depending on composition polarization may appear along the 4 fold axis, or along one of the orthogonal 2 fold axes of the prototypic 4/mmm prototype. In PBN a pseudo morphotropic phase boundary (PMPB) exists near the 60:40 Pb:Ba composition. The intriguing feature for the PBN compositions is that for the tetragonal symmetry, the permittivity increases for directions orthogonal to the 4 fold axis and there is a second freezing (in the polar state) near 100K. At the MPB the symmetry may be switched by electric field to that with macro-polarization along 2 (orthorhombic) and now the second freezing takes place for polarization along 4. The low temperature freezing occurs whether the initial phase is glassy or ferroelectric and gives rise to fascinating families of unusual dielectric, piezoelectric, elastic and optical properties.

A second important contribution on this program stemmed from the very careful preparative studies to make ultra fine powders of simple perovskite ferroelectrics. The objective was to obtain understanding of the intrinsic size effects which must occur in ferroelectrics due to the cooperative nature of the phenomenon. From studies of spontaneous strain it was made clear that ferroelectricity in  $\text{BaTiO}_3$  did not occur in powders with particular size less than  $800\text{\AA}$  whereas in  $\text{PbTiO}_3$  ferroelectricity and spontaneous strain persists down to sizes of order  $170\text{\AA}$ .

In 0:3 type composites it is natural to have a major interest in the phenomenon of percolation, and of the critical concentrations for this phenomenon. Practical aspects of this work occur in the PTC polymer:carbon composites and in other systems.

Fundamental studies on silicon, germanium and silica germania composites using wavelength scanning ellipsometry have lead to the evolution of effective techniques for the evaluation of inhomogeneity in highly transparent oxides, in systems with uniaxial anisotropy and have validated spectroscopic ellipisometry as one of the most valuable nondestructive techniques for the study of ferroelectric surfaces and thin films.

DTIC QUALITY INSPECTED 8

<b>Accession For</b>	
DTIS GRA&I	<input checked="" type="checkbox"/>
DTIC TAB	<input type="checkbox"/>
Unannounced	<input type="checkbox"/>
Justification	
By _____	
Distribution/	
Availability Codes	
Dist	Avail and/or
A-1	Special

**NANOCOMPOSITES FOR ELECTRONIC APPLICATIONS**

**Period January 1, 1990 thru December 31, 1991**

**FINAL REPORT**

**Volume III**

**OFFICE OF NAVAL RESEARCH**

**Contract No. N00014-90-J-1558**

**APPROVED FOR PUBLIC RELEASE - DISTRIBUTION UNLIMITED**

**Reproduction in whole or in part is permitted for any purpose  
of the United States Government**

**L. Eric Cross**

**PENNSSTATE**



**THE MATERIALS RESEARCH LABORATORY  
UNIVERSITY PARK, PA**

## TABLE OF CONTENTS

ABSTRACT .....	5
1.0 INTRODUCTION .....	7
2.0 GENERAL PAPERS .....	8
3.0 RELAXOR FERROELECTRICS .....	8
4.0 MICRO COMPOSITES STUDIES .....	9
5.0 INTRINSIC SIZE EFFECTS IN FERROELECTRICS .....	10
6.0 SPECTROSCOPIC ELLISOMETRY .....	10
7.0 INVITED LECTURES .....	11
8.0 CONTRIBUTED PAPERS .....	12
9.0 HONORS TO MRL FACULTY AND STUDENTS .....	14

## APPENDICES

### *General Summary*

1. L. Eric Cross. "Ferroelectric Ceramics: Tailoring Properties for Specific Applications," Proceedings of the Summer School on Ferroelectrics, Ascona, Switzerland (September 1991).

### *Relaxor Ferroelectrics*

2. R. E. Newnham and T. R. Shrout. "Electronic Ceramics," Advanced Ceramics (Electronic), Vol. 1, pp. 601.
3. D. D. Viehland. "The Glassy Behavior of Relaxor Ferroelectrics," PhD Thesis, Solid State Science, The Pennsylvania State University (May 1991).
4. R. Guo. "Ferroelectric Properties of Lead Barium Niobate Compositions Near the Morphotropic Phase Boundary," PhD Thesis, Solid State Science, The Pennsylvania State University (December 1990).
5. D. A. McHenry. "Optical and Electrooptical Properties of Lead Magnesium Niobate-Lead Titanate," PhD Thesis, Solid State Science, The Pennsylvania State University (May 1992).
6. Jayne R. Giniewicz. "An Investigation of the Lead Scandium Tantalate-Lead Titanate Solid Solution System," PhD Thesis, Solid State Science, The Pennsylvania State University (December 1991).

## APPENDICES (*continued*)

7. A. S. Bhalla, R. Guo, L. E. Cross, G. Burns, F. H. Dacol, and R. R. Neurgaonkar. "Glassy Polarization in the Ferroelectric Tungsten Bronze (BaSr)Nb<sub>2</sub>O<sub>6</sub>," J. Appl. Phys. 71 (11), 5591 (1992).
8. C. A. Randall, R. Guo, A. S. Bhalla, and L. E. Cross. "Microstructure-Property Relations in Tungsten Bronze Lead Barium Niobate Pb<sub>1-x</sub>Ba<sub>x</sub>Nb<sub>2</sub>O<sub>6</sub>," J. Mat. Res. 6 (8), 1720 (1991).
9. R. Guo, A. S. Bhalla, and L. E. Cross. "Pyroelectric Properties of Lead Barium Niobate Single Crystals," Ferroelectrics 118, 77 (1991).
10. D. Viehland, S. J. Jang, L. E. Cross, and M. Wuttig. "The Dielectric Relaxation of Lead Magnesium Niobate Relaxor Ferroelectrics," Phil Mag B 64 (3), 335 (1991).
11. D. Viehland, S. J. Jang, L. E. Cross, and M. Wuttig. "Anelastic Relaxation and Internal Strain in Lead Magnesium Niobate Relaxors," Phil Mag A 64 (4), 835 (1991).
12. D. Viehland, S. J. Jang, L. E. Cross, and M. Wuttig. "Local Polar Configurations in Lead Magnesium Niobate Relaxors," J. Appl. Phys. 69 (1), 414 (1991).
13. D. Viehland, M. Wuttig, and L. E. Cross. "The Glassy Behavior of the Relaxor Ferroelectrics," Ferroelectrics 120, 71 (1991).
14. D. Viehland, S. J. Jang, L. E. Cross, and M. Wuttig. "Freezing of the Polarization Fluctuations in Lead Magnesium Niobate Relaxors," J. Appl. Phys. 68 (6), 2916 (1990).
15. J. R. Giniewicz, A. S. Bhalla, and L. E. Cross. "Lead Scandium Tantalate - Lead Titanate Materials for Field Stabilized Pyroelectric Device Applications," Ferroelectrics Letters 14, 21 (1992).
16. J. R. Giniewicz, D. A. McHenry, T. R. Shrout, S. J. Jang, A. S. Bhalla, and F. Ainger. "Characterization of (1-x) PbMg<sub>1/3</sub>Nb<sub>2/3</sub>O<sub>3</sub>-xPbTiO<sub>3</sub> and PbSc<sub>1/2</sub>Ta<sub>1/2</sub>O<sub>3</sub> Transparent Ceramics Prepared by Uniaxial Hot Pressing," Ferroelectrics 102, 167 (1990).
17. J. R. Giniewicz, A. S. Bhalla, and L. E. Cross. "Pyroelectric Response and Depolarization Behavior of (1-x) PbSc<sub>1/2</sub>Ta<sub>1/2</sub>O<sub>3</sub>-xPbTiO<sub>3</sub> Materials," Ferroelectrics 118, 157 (1991).
18. D. A. McHenry, J. R. Giniewicz, T. R. Shrout, S. J. Jang, and A. S. Bhalla. "Electrical and Optical Properties of Relaxor Ferroelectrics," Ferroelectrics 102, 161 (1990).
19. D. A. McHenry, J. R. Giniewicz, S. J. Jang, T. R. Shrout, and A. S. Bhalla. "Optical and Electro-optical Properties of Lead Magnesium Niobate:Lead Titanate," Ferroelectrics 107, 45, (1990).

## APPENDICES (continued)

20. D. A. McHenry, J. Giniewicz, S. J. Jang, A. S. Bhalla, and T. R. Shrout. "Optical Properties of Hot Pressed Relaxor Ferroelectrics," *Ferroelectrics* **93**, 351 (1989).
21. G. R. Fox, J. K. Yamamoto, D. V. Miller, L. E. Cross, and S. K. Kurtz. "Thermal Hysteresis of Optical Second Harmonic in Paraelectric BaTiO<sub>3</sub>," *Materials Letters* **2** (7, 8), 284 (1990).

### *Micro Composites Studies*

22. G. R. Harshe. "Magnetolectric Effect in Piezoelectric-Magnetostrictive Composites," PhD Thesis, Solid State Science, The Pennsylvania State University (August 1991).
23. G. Harshe, J. Dougherty, and R. E. Newnham. "Magnetolectric Effect in Composite Materials," Proceedings Conference on Smart Materials and Structures, SPIE, Albuquerque, NM (February 1-4, 1993).
24. G. Harshe, J. P. Dougherty, and R. E. Newnham. "Theoretical Modelling of 3-0/0-3 Magnetolectric Composites," Submitted, *Int. J. of Appl. Electromagnetics in Materials*.
25. G. Harshe, J. P. Dougherty, and R. E. Newnham. "Theoretical Modelling of Multilayer Magnetolectric Composites," Submitted, *Int. J. of Appl. Electromagnetics in Materials*.
26. R. J. Sullivan and R. E. Newnham. "Composite Thermistors," *Chemistry of Advanced Materials*, Edited by C. N. R. Rao, Blackwell Scientific Publications (1992).
27. G. R. Ruschau, S. Yoshikawa, and R. E. Newnham. "Percolation Constraints in the Use of Conductor-Filled Polymers for Interconnects," *Proc. Elect. and Comp. Tech., IEEE*, San Diego (May 18-20, 1992).
28. M. Blaszkiewicz, D. S. McLachlan, and R. E. Newnham. "The Volume Fraction and Temperature Dependence of the Resistivity in Carbon Black and Graphite Polymer Composites: An Effective Media Percolation Approach."
29. G. R. Ruschau, S. Yoshikawa, and R. E. Newnham. "Resistivities of Conductive Composites," *J. Appl. Phys.* **72** (3), 953 (1992).
30. D. M. Moffatt, J. Runt, W. Huebner, S. Yoshikawa, and R. E. Newnham. "PTC Effects in Conductor Filled Amorphous Polymer Composites," *PTC Effects in Polymer Composites*, Chapter 3, pp. 51.

### *Intrinsic Size Effects in Ferroelectrics*

31. R. E. Newnham, K. R. Udayakumar, and S. Trolier-McKinstry. "Size Effects in Ferroelectric Thin Films," Book Chapter, *Chemical Processing of Advanced Materials*, Editor L. Hench, J. K. West, John Wiley & Sons Inc. (1992).

### *Spectroscopic Ellipsometry*

32. N. Van Nguyen. "Spectroscopic Ellipsometry of Interfaces," PhD Thesis, Physics, The Pennsylvania State University (November 1989).

## APPENDICES (*continued*)

33. P. Chindaudom. "Characterization of Inhomogeneous Transparent Thin Films on Transparent Substrates by Spectroscopic Ellipsometry," PhD Thesis, Physics, The Pennsylvania State University (August 1991).
34. N. V. Nguyen, K. Vedam, and J. Narayan. "Characterization of the Interface Between Ge<sup>+</sup> -Implanted Crystalline Silicon and Its Thermally Grown Oxide by Spectroscopic Ellipsometry," *J. Appl. Phys.* 67 (2) (1990).
35. S. Trolier-McKinstry, H. Hu, S. B. Krupanidhi, P. Chindaudom, K. Vedam, and R. E. Newnham. "Spectroscopic Ellipsometry Studies on Ion Beam Sputter Deposited Pb(ZrTi)O<sub>3</sub> Films on Sapphire and on PT Coated Silicon Substrates," Submitted, *J. Appl. Phys.*
36. J. Chen, K. R. Udayakumar, K. G. Brooks, and L. E. Cross. "Dielectric Behavior of Ferroelectric Thin Films at High Frequencies," pp. 182, Proc. ISAF 92, Greenville, South Carolina.
37. K. R. Udayakumar, J. Chen, K. G. Brooks, L. E. Cross, A. M. Flynn and D. J. Ehrlich. "Piezoelectric Thin Film Ultrasonic Micromotors," *Mat. Res. Soc. Symp. Proc.*, Vol. 243, pp. 49-54 (1992 Materials Research Society).

**MICRO-COMPOSITES STUDIES**  
**(continued)**

**APPENDIX 26**

---

# 16 Composite Thermistors

R.J. SULLIVAN and R.E. NEWNHAM

*Materials Research Laboratory, The Pennsylvania State University, University Park, PA 16802, USA*

## 1 Introduction

The combination of two or more phases to form a composite is a common occurrence in modern materials engineering. By combining phases, the functional figure of merit, which usually involves more than one property coefficient, can be optimized. One such example of a functional composite is the conductive oxide-polymer positive temperature coefficient thermistor.

Thermistors, temperature-dependent resistors, are typically made from doped ceramic ( $\text{BaTiO}_3$ ). The desire for improved properties and ease of processing has spurred the development of composite thermistors. This type of composite combines a low resistivity filler powder, such as carbon black, vanadium sesquioxide, or nickel, with a high resistivity polymer matrix such as polyethylene or polystyrene. In the dormant room temperature state the thermistor has a resistivity similar to the filler. On being activated by heating, however, the resistivity increases to a value close to the polymer matrix resistivity, often an increase of eight orders of magnitude.

## 2 Thermistors

Thermistors may be classified as one of two types. Negative temperature coefficient (NTC) thermistors exhibit a decrease in resistivity as temperature increases. Positive temperature coefficient (PTC) thermistors increase resistivity as temperature increases. The temperature range over which the change in resistivity occurs, or rather the slope of the resistivity-temperature curve, is very important. In applications where the ambient temperature is to be determined by the resistivity of the thermistor, a gradual PTC transition would be required. If the thermistor is to be used as a current limiter, a very steep PTC transition is needed so that at a given thermistor temperature the switch from the low to the high resistivity state is rapid and the circuit protected. Critical temperature thermistors exhibit their change in resistivity over a very short temperature range. Resistivity curves for both NTC and PTC thermistors are shown in Fig. 16.1.

In an electrical circuit the thermistor is placed in series with the load as shown in Fig. 16.2. Configured in this way the thermistor must be invisible in the circuit, with low resistance in the dormant state. Once activated the thermistor resistance must be large enough to protect the load. Some of the many applications for thermistors are as flow sensors, liquid level sensors, current limiters and thermal sensors [1,2]. Thermistors being used for these applications may be found in hair dryers, television degaussers and window motors in automobiles.

Regardless of how a thermistor is utilized in a product, it must meet some basic requirements. The thermistor must not significantly change the total resistance of

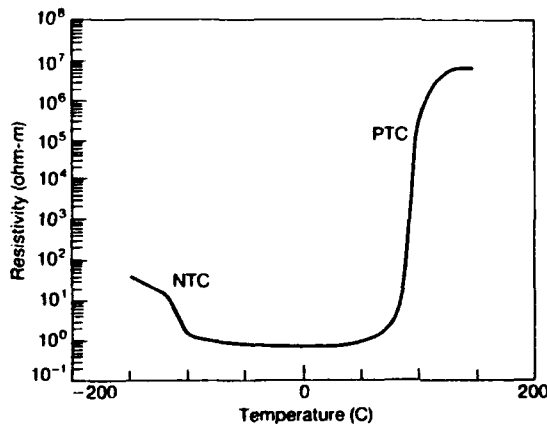


**Fig. 16.1** Thermistor resistivity dependence upon temperature for a 30 vol%  $V_2O_3$ - polymethylmethacrylate composite. NTC, negative temperature coefficient; PTC, positive temperature coefficient of resistance. Measured at 1 kHz [26].

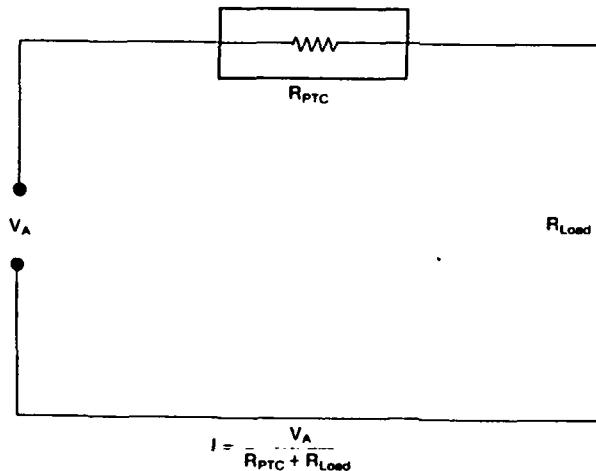


**Fig. 16.2** Circuit illustrating how a thermistor is used in series with a load. Current flowing in the circuit is calculated by the given equation.

the circuit in its dormant state (low room temperature resistance). Total change in resistivity of the thermistor and the temperature range over which it occurs must suit the needs of the application. The power handling capabilities of the thermistor must allow normal circuit operation in the dormant state without switching to the active state. And finally, as the temperature increases past the thermistor transition, the electrical behavior of the thermistor must not be detrimental to the device. For example, a decrease in resistivity after the transition in a PTC thermistor could not be tolerated in many applications.

A PTC curve and the corresponding current–voltage ( $I$ – $V$ ) curve for a PTC thermistor are shown in Fig. 16.3. Referring to Fig. 16.3, as the temperature of the thermistor is increased to  $T_1$  the resistivity remains constant, resulting in a linear  $I$ – $V$  characteristic up to point 1. As the temperature increases through the PTC transition ( $T_2$ ) the resistivity increases dramatically and the  $I$ – $V$  curve shows a nonlinear decrease in current with increasing voltage (point 2). At higher tempera-

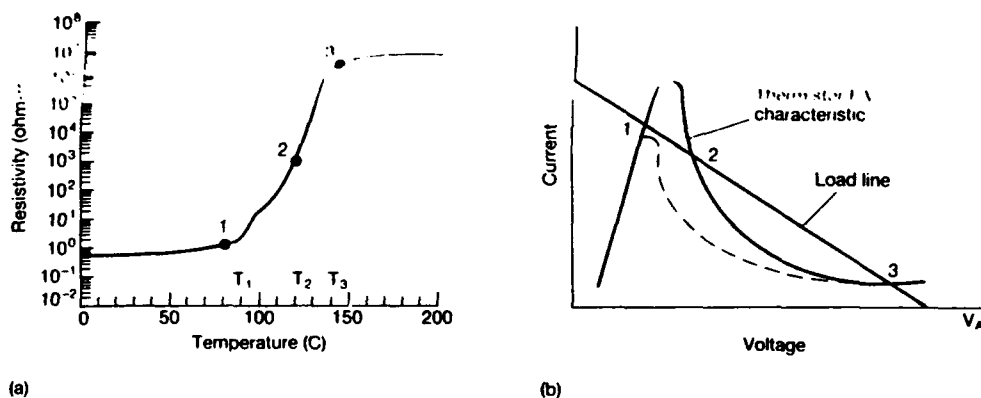


**Fig. 16.3** (a) PTC resistivity curve for a 30 vol%  $V_2O_3$ -polystyrene thermistor measured at 1 kHz [26]. (b) Thermistor  $I$ - $V$  characteristics derived from the PTC curve. Numbers denote points of importance for both curves.

tures ( $>T_3$ ) the resistivity once again becomes constant and a linear  $I$ - $V$  relationship results (point 3). Points 1 and 3 are the two stable points of operation for a thermistor.

When the PTC thermistor is in series with a load it may be switched from the high current phase to the low current phase in one of three ways [1]. If the voltage increases, the load line shifts to higher voltages while maintaining the same slope, which results in the peak of the thermistor  $I$ - $V$  curve dropping below the load line. Consequently, point 3 is the only stable point and the thermistor switches. The thermistor is therefore used as protection against high voltage. An increase in the voltage increases the power generated in the thermistor, which increases the thermistor temperature. At an elevated temperature the thermistor resistance increases and the voltage is limited. After the high voltage is removed the thermistor cools, the thermistor resistance returns to the lower value and the circuit once again operates as designed.

In the event of the loss of load resistance the load line increases in slope. Once the thermistor  $I$ - $V$  curve maxima falls below the load line the PTC thermistor switches (again point 3 is the only stable point). Current stabilization and protection against short-circuits are applications which take advantage of the PTC switching in this fashion. A short-circuit or decrease in the load resistance increases the current in the circuit. The increased current heats the thermistor and switches it into the high resistance state which limits the current in the circuit.

The third type of protection is against increases in the ambient temperature. If the ambient temperature increases, the thermistor  $I$ - $V$  curve changes (dotted line in Fig. 16.3b). Again, point 3 is the only stable point and switching occurs. The thermistor protects against overheating past the switching temperature by limiting current flow. Applications capitalizing on the thermistor switching in this fashion are protection against overheated motors, temperature control and temperature measurement [3]. For application as a temperature regulator in a hair dryer the thermistor is placed in the flow of warm air. As the air temperature heats past the

switching temperature ( $T_s$ ) the thermistor switches to the active state and limits the current to the load, in this case the heating coil. As the temperature falls below  $T_s$  the thermistor resistance decreases and allows current to flow once again to the heating coil. Hence, the air temperature becomes stabilized at  $T_s$ .

### 3 Ceramic thermistors

PTC thermistors manufactured from ceramics are typically  $\text{BaTiO}_3$  based. Other ceramics such as chromium-doped vanadium sesquioxide ( $(\text{V,Cr})_2\text{O}_3$ ) also have a PTC behavior. Both systems have their own merits.

Barium titanate, when donor doped with elements such as  $\text{La}^{+3}(\text{Ba}_{1-x}\text{La}_x\text{TiO}_3)$  or  $\text{NB}^{+5}$  exhibits PTC behavior near its Curie temperature ( $T_c$ ) [3-9]. At the Curie temperature the barium titanate switches from a ferroelectric tetragonal state to a paraelectric cubic state.

Grain boundaries are responsible for the PTC transition; hence, no PTC is seen in doped single crystal barium titanate [10,11]. The ceramic thermistor must be prepared with a dopant or under a reducing atmosphere which results in semiconducting doped barium titanate. Reoxidation of the grain boundaries leaves them insulating. Excess oxygen in the grain boundary creates an electron depletion region near the grain boundary. Consequently, electron conduction does not occur across the grain boundary.

The spontaneous polarization of the barium titanate below  $T_c$  results in compensation of the charge at the grain boundary. The result is electron flow across the grain boundary (low temperature dormant state). Once the temperature increases past  $T_c$ , the barium titanate switches to the paraelectric cubic state, which destroys the spontaneous polarization. Without the spontaneous polarization to compensate for the charge at the grain boundary, electrons cannot flow across the grain boundary and the resistance of the doped barium titanate increases.

The change in resistivity may be up to six orders of magnitude (depending on processing). As the temperature increases even further above  $T_c$ , the barium titanate thermistor exhibits a gradual NTC. This is due to the increasing number of electrons which have enough thermal energy to jump over the barrier at the grain boundary. This NTC, as mentioned earlier, may render the PTC useless in some applications. Other drawbacks to doped barium titanate thermistors include difficult processing and a relatively high room temperature resistivity (100 to 1000  $\Omega\text{-cm}$ ) [3,8].

Another ceramic which displays PTC as well as NTC thermistor behavior is chromium doped vanadium sesquioxide ( $(\text{V,Cr})_2\text{O}_3$ ) [12,13]. Both transitions, the NTC ( $-100^\circ\text{C}$ ) and the PTC (between  $-100$  and  $200^\circ\text{C}$ ) are discontinuous metal-semiconductor transitions. The PTC transition is a bulk effect seen in both single-crystal and polycrystalline samples, and is only two orders of magnitude in size. The low room temperature resistivity ( $10^{-3} \Omega\text{-cm}$ ) and high current carrying capabilities (200 A) make this composition a prime candidate for applications in which barium titanate thermistors are not suitable, but reproducible processing is difficult.

#### 4 Composite thermistors

The need for thermistors with a lower room temperature resistivity and easier fabrication has led to the development of polymer composite thermistors. Carbon black-polyethylene is the most widely used, commercially available composite thermistor. Although dependent upon specific composition and processing, the carbon black-polyethylene thermistors may exhibit a room temperature resistivity near  $1 \Omega\text{-cm}$  and PTC magnitude of up to six orders [14,15]. Fillers such as  $V_2O_3$ ,  $TiB_2$ , and Ni in polyethylene have also shown similar low room temperature resistivities with even larger PTC steps (up to eight orders in magnitude). The PTC transition occurs near the melting temperature of the semicrystalline polymer matrix.

Other systems being explored include conductive oxide as well as metal fillers in amorphous polymer matrices [16-24]. The electrical properties of these thermistors are comparable to those using a semi-crystalline matrix. With an amorphous matrix, however, the PTC transition occurs near the glass transition temperature ( $T_g$ ) of the polymer matrix. In addition, the PTC transition in the amorphous polymer composites is typically not as steep as the semi-crystalline systems.

The remainder of this chapter will describe the processing, electrical properties and mechanisms responsible for the PTC transition in the PTC composite thermistor. A significant effort has been put forth at the Pennsylvania State University Materials Research Laboratory to further understanding of composite thermistors. Electrical properties of the composite thermistor have been studied to determine how processing, filler characteristics, polymer characteristics, and additional additives affect its performance [15,16,18,25,26,34,74].

#### 5 Processing

Basic processing of conductive filler-polymer composite thermistors is illustrated by the flowchart in Fig. 16.4. Detailed descriptions of each processing step are contained in the literature [2,27-29].

The conductive filler and polymer are batched according to the polymer type. For a thermoplastic polymer (e.g. polyethylene or polystyrene) a high-temperature ( $160^\circ\text{C}$ ), high-shear mixer is used. For epoxies or other thermoset polymers, low-shear mixing is carried out at room temperature followed by curing at an elevated temperature ( $70^\circ\text{C}$ ).

In the case of a thermoplastic, the composite is further processed by using pressure (20 000 psi) and elevated temperatures ( $150^\circ\text{C}$ ) to form the desired thermistor shape. This shape may be a pellet or a sheet from which individual thermistors are punched. Attachment of metal foil electrodes, such as  $50 \mu\text{m}$  Ni foil, is also accomplished in this step. In addition to making electrical contact with the composite, the stiffness of the metal foil increases the high temperature mechanical stability of the thermistor. The side of the foil in contact with the composite should be either mechanically or chemically roughened to promote adhesion between the electrode and composite. As for the thermoset polymer

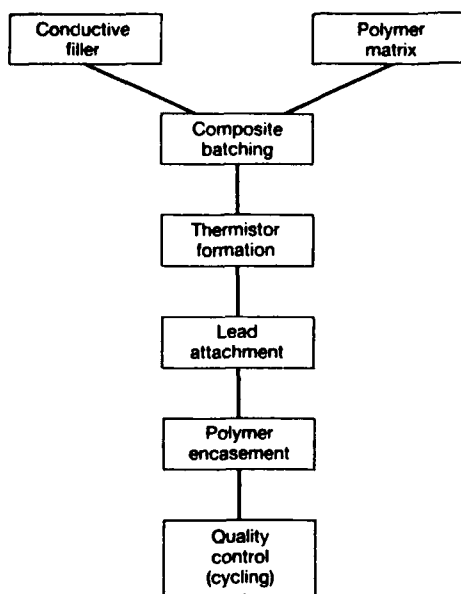


Fig. 16.4 Flowchart describing the process of conductive filler-polymer composites.

matrix, further shaping must be done by machining, as the polymer is already cross-linked into a rigid form.

Leads are attached to the thermistor, after which the thermistor is coated with another protective polymer layer. Temperature cycling at this point has two benefits. The first is that at elevated temperatures the stresses induced by processing are relieved. These stresses are responsible for the initial change in electrical properties observed upon cycling [14,23,30]. The second benefit is that cycling may be used to screen for undesirable parts.

The electrical resistivity of the thermistor at elevated temperatures is of great concern. NTC behavior is often observed after the PTC transition, similar to the barium titanate thermistors. This decrease in resistivity is the result of the conductive filler moving about in the less viscous polymer matrix to form new conductive paths [2,14,31].

To eliminate this NTC behavior several approaches have been used. The first is to cross-link the polymer matrix. Cross-linking of polyethylene may be done either chemically or by exposure to radiation [32,33]. The result of cross-linking is the elimination of the high temperature NTC and, unfortunately, an increase in the room temperature resistivity (Fig. 16.5). Cross-linking of the polymer diminishes the mobility of the polymer chains at high temperatures. Consequently, the mobility of the conducting particles is decreased and the NTC effect eliminated.

Another method used to eliminate the high temperature NTC is by adding an inert third phase such as mullite [15,34]. This third phase, when approximately two orders of magnitude larger in size than the carbon black filler, hinders the movement of the carbon black at higher temperatures. The result is the elimination of the NTC. In addition, the thermal cycling properties of the thermistor are superior to those of similar cross-linked carbon black-polyethylene composites.

Addition of a third phase which exhibits a phase change is another technique

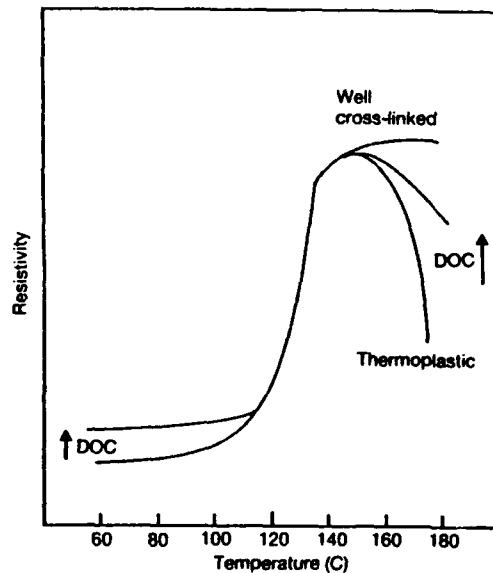


Fig. 16.5 Effect of cross-linking on the electrical properties of carbon black-polyethylene composite thermistor [32] (DOC, degree of cross-linking).

used to eliminate NTC behavior. Brodeur and associates used pentaerythritol ( $C_5H_{12}O_4$ ) as the third phase in a carbon black-polystyrene composite [25]. Pentaerythritol has a solid-solid phase transition near  $185^\circ\text{C}$  with a latent heat of transition of  $4.13\text{ kJ/mol}$ . In addition to absorbing heat at the solid-solid transition, the particle size of the pentaerythritol ( $8\text{ }\mu\text{m}$ ) aided in the mechanical stability of the composite, similar to the inert mullite phase previously mentioned. As the ambient temperature is raised to  $185^\circ\text{C}$ , the phase transition in the pentaerythritol absorbs energy and stabilizes the thermistor temperature at  $185^\circ\text{C}$ . The length of time the thermistor is held at this latch temperature is dependent upon the vol% pentaerythritol in the composite and the heating rate of the sample. For a composite with 50 vol% pentaerythritol and a heating rate of  $6^\circ\text{C}/\text{min}$ , a delay greater than 5 min was seen as shown in Fig. 16.6. The NTC behavior is eliminated because the temperature of the samples does not reach a value at which damage to the sample may occur.

## 6 Percolation

As the volume fraction of conductive filler in the polymer increases, the resistivity of the composite decreases slightly until at a certain critical volume fraction ( $V_c$ ), the resistivity decreases drastically because of the increased connectivity of the filler (Fig. 16.7). At this volume fraction, conductive chains are formed in the composite. This phenomena is often described using percolation theory. In this case, percolation is used to describe the 'richness of interconnects' in the composite thermistor. Many introductions and overviews of percolation may be found in the literature [35-37].

Percolation is often assumed to be one of three types: site, bond or continuum percolation. Site percolation describes the polymer as a lattice and the filler as being

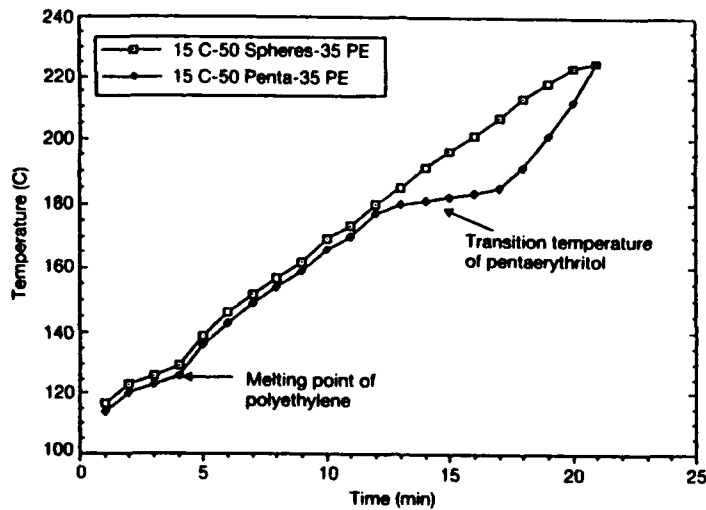


Fig. 16.6 Thermal delay seen for a composition containing 15 vol% carbon black–35 vol% polyethylene–50 vol% pentaerythritol as compared to a composition with 50 vol% inert mullite spheres in place of the pentaerythritol.

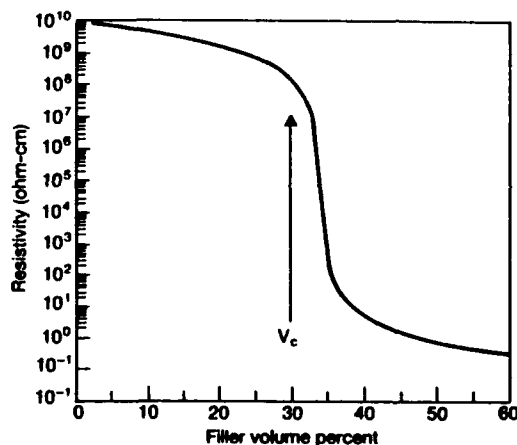


Fig. 16.7 Percolation curve for a 0.3 mm  $V_2O_3$ –polystyrene composite system [26].  $V_c$  denotes the volume fraction at which a rapid decrease in resistivity occurs.

randomly added at various lattice sites. If two adjacent sites are filled then the interface is taken to be conductive. In bond percolation the lattice is completely occupied by the filler and there is a finite probability that the 'bond' between two particles may (or may not) be conducting [38–40]. Continuum percolation does not involve a lattice but rather randomly distributes the filler phase throughout the matrix [41,42].

The value of  $V_c$  is very dependent upon the filler and polymer selected. In carbon black–polymer composites it has been shown that  $V_c$  increases as the surface tension of the polymer increases [43,44]. Sumita *et al.* attribute this to the interfacial excess energy ( $\Delta g$ ) the carbon black introduces to the system and model it with the following equation [44]:

$$V_c = \Delta g^* R / (1 + 3(\gamma c^{1/2} - \gamma p^{1/2})^2) \quad (1)$$

Where  $V_c$  is the critical volume fraction,  $\Delta g^*$  the critical interfacial excess energy beyond which the filler coagulates,  $R$  the filler radius, and  $\gamma_c$  and  $\gamma_p$  the surface tension of the carbon black and polymer, respectively. This relation is valid when the difference between  $\gamma_c$  and  $\gamma_p$  is not small due to assumptions made during its derivation.

Moffatt has shown the contrary to be true for the  $V_2O_3$  filled polymer system [16]. She saw that as the wetting between the filler and polymer increased,  $V_c$  is shifted toward higher values. The increased  $V_c$  was attributable to better dispersion of the filler in the systems having superior wetting. The major differences between the two fillers is the particle size and the particle surface energy. In the  $V_2O_3$ -polymer system the relation in Equation 1 is not valid due to a small difference between the surface tensions of the filler and polymer, as mentioned above.

Several studies have shown that carbon blacks with small particle size and high surface area have a lower percolation threshold than other carbon blacks [45-49]. This result is also predicted by Equation 1. Similar results have been reported for systems in which a metal powder is mixed with a polymer powder at room temperature and then pressed [50,51]. When the polymer particle size was held constant, a decrease in the metal powder particle size decreased  $V_c$ . In this case the metal powder coats the polymer particles. The smaller the metal powder the less volume needed to coat the polymer. Kusy showed these trends for the nickel-polyethylene mixture where the particle size of the polymer ranged from 2 to 30 times the particles size of the metal [51].

Sullivan saw the opposite particle size effect in the  $V_2O_3$ -polystyrene system [26]. Varying the  $V_2O_3$  particle size from 325  $\mu\text{m}$  down to 0.3  $\mu\text{m}$  increased  $V_c$  from 0.04 to 0.34. These results further emphasize the differences between the carbon black-semicrystalline and conductive filler-amorphous polymer systems brought about by the large difference in the filler particle size and surface energy.

In addition, a dependence of  $V_c$  on the sample geometry was also shown. Increasing the sample thickness from 0.06 cm to 0.2 cm increased  $V_c$  from 0.04 to 0.08 for the 325  $\mu\text{m}$   $V_2O_3$  particle size. This increase was attributed to the increased difficulty in forming a conductive chain across the thicker sample.

## 7 Carbon black-semicrystalline composite thermistors

The most widely studied and commercially available composite thermistor system is that of a carbon black-semicrystalline polymer such as polyethylene. Several reviews have been written about this system describing processing, possible conduction mechanisms and filler property effect [52,53]. Doljack describes the properties and uses of the commercially available carbon black-polyethylene based PolySwitch® [14]. A PolySwitch® CO2R006 thermistor with a low temperature resistance of 0.042  $\Omega$  can dissipate 0.95 W of power at an ambient temperature of 40°C before switching to the high resistance state. Room temperature resistivities of 1-5  $\Omega\text{-cm}$  with PTC magnitudes of six orders have been reported for this type of thermistor.

The electrical properties are very dependent upon the type of carbon black, polymer, and processing of the thermistor [14,54,55]. Smaller sized (less struc-

tured) carbon blacks exhibit the lowest room temperature resistivity. The magnitude of the PTC transition also decreases as the size of carbon black decreases.

A polymer with a higher degree of crystallinity exhibits a larger PTC anomaly. Low density polyethylene has a PTC magnitude of 3.5 orders of magnitude while high density polyethylene has a PTC of 4.5 orders [56]. In addition, a polymer with a narrow melting temperature range has a steep PTC transition [45]. PTC effects are seldom seen in carbon black–amorphous rubber composites. In these systems the anomaly occurs only at filler concentrations very near the critical volume fraction [57].

The mechanism responsible for the PTC transition in the carbon black–semicrystalline polymer composites has not been positively identified, though several models have been proposed. At temperatures below the melting temperature ( $T_m$ ) of the polymer, carbon black is excluded from the crystalline polymer regions. This segregation results in a low resistivity composite. At higher temperatures the crystalline regions melt and the polymer matrix becomes less viscous. Rearrangement of the conductive particles into these new amorphous regions disrupts the conductive paths and increases the composite resistivity [33,45].

Kohler explains the increase in resistivity as conductive chains being pulled apart by the thermal expansion of the polymer [58]. At the melting temperature a discontinuous increase in volume would account for the large increase in resistivity. Figure 16.8 shows the increase in volume and resistivity with temperature for a carbon black–polyethylene composite as reported by Doljack [14]. The rapid change in resistance of the thermistor shadows the change in the composite volume, supporting the views of Kohler.

Further support for the importance of the polymer thermal expansion for a PTC transition was given by Sullivan [26]. Working with the  $V_2O_3$ -polystyrene system the thermal expansion of the composite above  $T_g$  was varied by increasing the

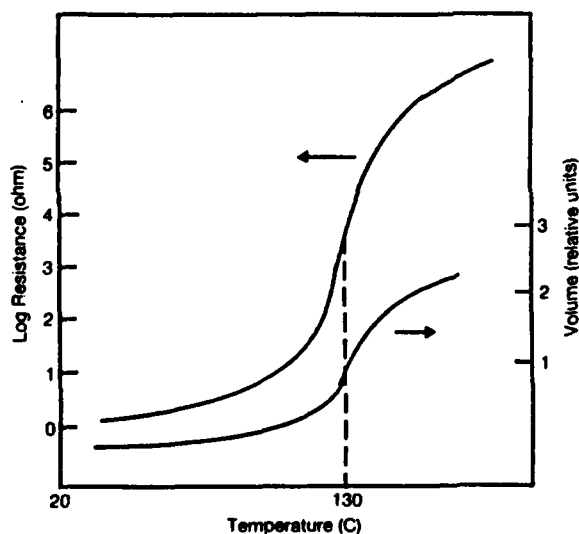


**Fig. 16.8** Composite resistivity and volume expansion of the matrix polymer as a function of temperature for a carbon black–polystyrene thermistor [14].  $T_m$  of polystyrene is approximately 130°C.

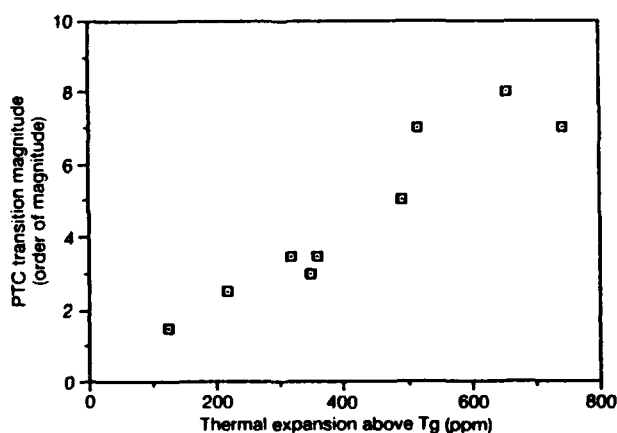


**Fig. 16.9** Dependence of PTC transition magnitude on the composite thermal expansion above  $T_g$ . Samples were 30 vol%  $V_2O_5$ -polystyrene irradiated with varying doses of gamma radiation. Doses of 250 and 50 MRad resulted in thermal expansions of approximately 200 and 700 ppm, respectively [26].

cross-link density of the polymer. Figure 16.9 shows the dependence of the PTC magnitude on the thermal expansion of the system.

Two other possible mechanisms involve electron tunneling through a very thin ( $<100 \text{ \AA}$ ) polymer layer between carbon black particles. Ohn and Natio state that large gaps influence the resistivity of a conducting chain more than small gaps [59]. At low temperatures ( $<T_m$ ) the average gap width is small enough to permit tunneling. Above  $T_m$  the distribution of the gap widths increases due to some particles being pulled apart while others are pushed together. The larger gap widths resulting from particles moving apart do not allow tunneling, effectively increasing the chain resistivity. Consequently, the composite resistivity increases.

Meyer assumes that crystalline polymer regions ( $300 \text{ \AA}$ ) separate the conduction particles [56,60]. Electron tunneling through these regions is easier than tunneling through similar amorphous regions. Consequently, as the crystalline regions melt, the probability of tunneling decreases and the composite resistivity increases. The NTC behavior above the PTC transition, Meyer explains, is due to the compressed carbon black expanding and once again making electrical contact to decrease the resistivity.

## 8 Conductive filler-amorphous polymer composites

The newest class of thermistor materials are the amorphous polymer based composites. Although not seen in carbon black-amorphous polymer composites, a PTC transition is present in some metal and many conductive oxide-amorphous polymer composites [16,18,20,23,24,61]. The transition occurs near the glass transition temperature ( $T_g$ ) of the polymer.

As with the carbon black-polyethylene thermistors, selection of the filler is very important for a low resistivity at room temperature. Filler resistivity must be less than the desired composite resistivity. The particle size of the filler is also critical due to the particle-particle contact resistance [62]. As the particle size decreases, the number of particles required to form a conducting chain increases, as does the

number of contacts. As a result, the composite resistivity increases.

With transition metal oxides such as  $V_2O_3$ ,  $Ti_2O_3$  and  $VO_2$ , a low temperature NTC transition may be incorporated into the thermistor in addition to a somewhat larger high temperature PTC effect [18]. This NTC is associated with the semiconductor to metal phase transition in the filler. The resulting resistivity behavior is a square well effect as seen in Fig. 16.1.

Hu and co-workers batched  $V_2O_3$  with polyethylene and epoxy [61]. The PTC seen in the  $V_2O_3$ -polyethylene composite was very steep ( $\Delta T = 5^\circ C$ ) and occurred at  $130^\circ C$  ( $T_m$ ). The PTC for the  $V_2O_3$ -epoxy composites occurred near  $100^\circ C$  ( $T_g$ ) and was not as steep ( $\Delta T = 20^\circ C$ ). The PTC magnitude was 10 and eight orders for the polyethylene and epoxy systems, respectively.

Littlewood and Briggs report a PTC of greater than five orders for a silver-coated copper-epoxy composite [23]. They also report a lower room temperature resistivity with a higher epoxy curing temperature. The higher curing temperature results in greater internal stresses (greater shrinkage upon curing), which increase the contact pressure and area between the conductive particles.

## 9 Dispersion

Composite thermistors show a decrease in the high temperature resistivity with increasing frequency as shown for the  $V_2O_3$ -polymethylmethacrylate system in Fig. 16.10 [16]. The origin of this dispersive behavior stems from the relaxation of polarization mechanisms with increased frequency and has been reported by several authors [49,63-65].

At filler concentrations above  $V_c$  and at temperatures below the PTC transition, no frequency dependence was observed. As the thermistor switches to the high resistivity state, the conducting particles are presumably separated by an insulating layer [66,67]. This insulating layer controls the conduction of the composite.

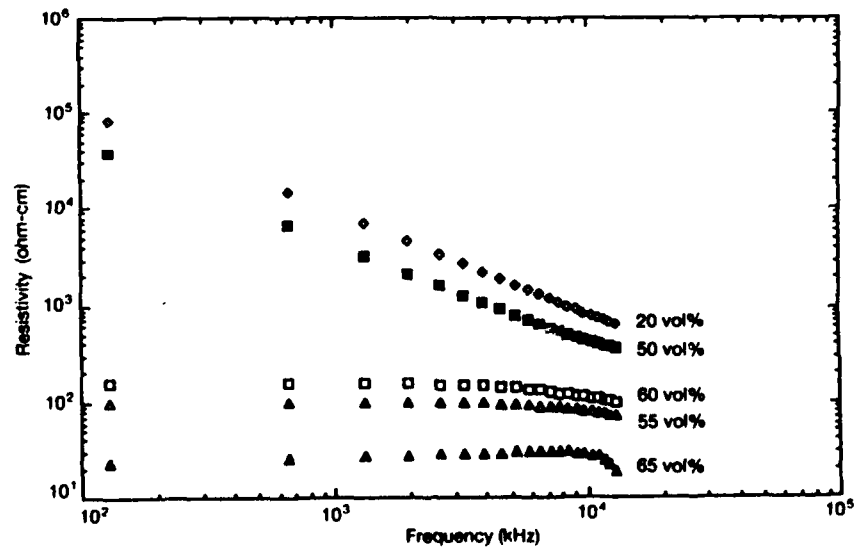


Fig. 16.10 Resistivity behavior of  $V_2O_3$ -polymethylmethacrylate thermistors showing frequency dispersion; vol% indicates the volume percent  $V_2O_3$  [67].

As the frequency increases, polarization mechanisms in the insulating layer begin to relax out. Two types of polarization that relax in the frequency range of the experimental values are space charge (up to  $10^3$  Hz) and dipolar (orientational, up to  $10^9$  Hz). Space charge polarization occurs when two materials of unequal conductivity are brought together. This is the result of charge building up at the interface. Dipolar polarization is due to the rotation of permanent dipoles in an electric field. As seen in many other systems where inhomogeneity results in barriers for charge movement, space charge polarization is most important [68].

Maxwell-Wagner theory is used to model this behavior [68,69]. The dielectric constant ( $K'$ ), loss ( $K''$ ), and resistivity ( $\rho$ ) are predicted by this theory using the following equations:

$$K' = K'_0 + \left( \frac{K'_0 - K'_\infty}{1 + \omega^2\tau^2} \right) \quad (2)$$

$$K'' = \frac{(K'_0 - K'_\infty)\omega\tau}{1 + \omega^2\tau^2} \quad (3)$$

$$\rho = \rho_\infty + \frac{(\rho_0 - \rho_\infty)}{1 + \omega^2\tau^2} \quad (4)$$

where

$\omega$  = frequency (Hz)

$\tau$  = time constant

$K'_0$  = static dielectric constant

$K'_\infty$  = optical dielectric constant

$\rho_0$  = low frequency resistivity ( $\Omega$ -cm)

$\rho_\infty$  = high frequency resistivity ( $\Omega$ -cm)

Figure 16.11 illustrates the Maxwell-Wagner capacitor model as applied to composites. At low frequencies the resistance of the gap ( $R_c$ ) is responsible for the high resistivity. At higher frequencies, relaxation of the polarization mechanisms in the polymer decreases the impedance due to the capacitance of the polymer and as a result, the resistance of the composite is due to the filler resistance ( $R_a$ ) [67].

## 10 Conduction

Three regions of conduction can be identified on a percolation curve. At low volume fraction filler, the composite is resistive and conducts primarily by ionic movement (impurities) and space charge effects. The filler at this concentration is dispersed throughout the composite at distances too great to facilitate electron tunneling [66].

As the volume fraction increases past  $V_c$ , the composite resistivity decreases sharply. In this region the conduction mechanism changes from one of ionic movement to electron tunneling. At higher fields, electron tunneling may be further enhanced by thermal fluctuations. At higher loadings the conductive particles are in contact or separated by only a very thin film of polymer. This results in the low resistivity [70,71].

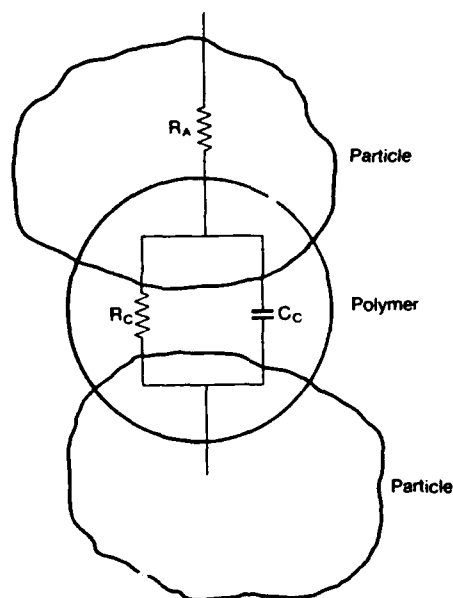


Fig. 16.11 The Maxwell-Wagner capacitor model is applied to the composite thermistor [67].

Variations in the gap width of the polymer affect the resistivity and type of conduction [72]. An increase in the gap width with temperature would decrease the probability of electron tunneling and increase the composite resistivity. Sherman *et al.* modeled the PTC transition behavior with electron tunneling [73]. Their results predicted a large PTC transition over a very small filler concentration for the nickel-polyethylene system. Moffatt *et al.* applied this model to the  $V_2O_3$ -polyethylene and  $V_2O_3$ -epoxy systems [74]. Qualitatively the model predicted the PTC behavior but did not quantitatively fit the data. The probability of this mechanism being responsible for the PTC transition is greatest in the semicrystalline polymer composite thermistors. These materials have a large volume expansion at the melting temperature which could separate conducting particles to the point where tunneling across the gap does not occur.

Another possible mechanism for the PTC transition is a decrease in the space charge region at  $T_g$  or  $T_m$  (depending on the polymer matrix) [16]. When a polymer and conductor are placed into contact, electrons are injected from the conductor into the polymer to align the Fermi energies [75,76]. At sufficient loadings ( $>V_c$ ) the space charge regions resulting between two conductive filler particles are close enough to allow conduction across the gap. As the temperature increases through  $T_g$  or  $T_m$  the number of energy states close to the filler surface that may be occupied by injected electrons increases. Consequently, the effective gap width increases due to the electrons not being injected as far into the polymer [16].

Ionic conduction may also be responsible, in part, for the PTC transition. At low temperatures the mobility of impurity ions in the composite is low. At temperatures greater than  $T_g$  (or  $T_m$ ) impurity ions migrate to oppose any applied electric field. This, in effect, cancels the field in local areas which limits conduction. As a result, the resistivity increases.

## 11 Summary

PTC thermistors are ideal for applications such as current stabilization, temperature control, and high voltage protection. Until recently, thermistors were manufactured primarily from ceramics. Developments in composites have produced thermistors with much lower dormant resistivities ( $1 \Omega\text{-cm}$ ) and easier fabrication than their ceramic counterparts. Because of this, composite thermistors are being used in applications which require low resistances and cost.

Although the mechanism responsible for the PTC transition is not agreed upon, it has been determined that in the low resistivity (dormant) state the resistivity is determined by the conductive filler. In the active, high resistivity, state the resistivity is controlled by the polymer matrix. The mechanism responsible for the rapid change in resistance is triggered by the phase transition in the polymer at  $T_g$  or  $T_m$ .

Additions of a third phase or cross-linking have been used to ensure that the properties of the thermistor do not degrade at high temperatures. The idea behind these steps is to either prevent the thermistor from reaching elevated temperatures, or limit the motion of the filler particles at these temperatures. These processing steps have been very successful in stabilizing the electrical properties of the thermistor with repeated cycling.

## 12 References

- 1 R.F. Blaha. *Proceedings of the Electronic Component Conference* (1971).
- 2 J.M. Taylor. US Patent 4,426,633, January 17, 1984.
- 3 P.D. Levett. *Ceram Age* **83**, 44 (1967).
- 4 H.A. Sauer & J.R. Fisher. *J Am Ceram Soc* **43**, 297 (1960).
- 5 W.T. Peria, W.R. Bratschum & R.D. Fenity. *J Am Ceram Soc* **44**, 249 (1961).
- 6 O. Saburi. *J Am Ceram Soc* **44**, 54 (1961).
- 7 V.J. Tennery & R.L. Cook. *J Am Ceram Soc* **44**, 187 (1961).
- 8 O. Saburi & K. Wakino. *IEEE Trans Compon Parts* **53** (1963).
- 9 B.M. Kulwicki. *Adv Ceram 1*, Am Ceram Soc, Columbus (1981).
- 10 W. Heywang. *J Am Ceram Soc* **47**, 484 (1964).
- 11 G.H. Jonker. *Adv Ceram 1*, Am Ceram Soc, Columbus (1981).
- 12 A. Ruegg, R.S. Perkins & P. Streit. *Sci Ceram* **11**, 559 (1981).
- 13 R.S. Perkins, A. Ruegg, M. Fischer, P. Streit & A. Menth. *IEEE Trans Compon Hybrids Manufact Technol* **5** (1982).
- 14 F.A. Doljack. *IEEE Trans Compon Hybrids Manufact Technol* **4**, 372 (1981).
- 15 L.L. Rohlfing, R.E. Newnham, S.M. Pilgrim & J. Runt. *J Wave-Mater Interact* **3**, 273 (1988).
- 16 D. Moffatt. *Electrical Properties of  $V_2O_5$ -Polymer Composite Thermistors*. PhD Dissertation, The Pennsylvania State University, December (1989).
- 17 F.F.T. De Araujo & H.M. Rosenberg. *Proceedings of the 1975 International Conference on Composite Materials* **2**, 560 (1975).
- 18 K.A. Hu, J. Runt, A. Safari & R.E. Newnham. *Ferroelectrics* **68**, 115 (1986).
- 19 R.R. Singh & R.W. Roberts. *Polym Compos* **6**, 58 (1985).
- 20 R. Matsushita, M. Senna & H. Kuno. *J Mater Sci* **12**, 509 (1977).
- 21 R. Mukhopadhyay, S.K. De & S. Basu. *J Appl Polym Sci* **20**, 2575 (1976).
- 22 S.K. Bhattacharya, S. Basu & S.K. De. *J Appl Polym Sci* **19**, 21 (1980).
- 23 S. Littlewood & B.F.N. Briggs. *J Phys D: Appl Phys* **11**, 1457 (1978).
- 24 L. Nicodemo, L., Nicolais, G. Romeo & E. Scafara. *Polym Eng Sci* **18**, 293 (1978).

- 25 S.A. Brodeur W. Huebner, J.P. Runt & R.E. Newnham. *J Mat Res* 6, 175 (1991).
- 26 R.J. Sullivan. *Processing Effects on PTC Composite Thermistors*. PhD Dissertation, The Pennsylvania State University (1991).
- 27 L.T. Toy, W.W. Moyer, B.J. Lyons & D.A. Horsma. US Patent 4,388,607, June 14, 1983.
- 28 L.J. Middleman, J. Evans & D. Pettengill. US Patent 4,238,812, Dec. 9, 1980.
- 29 S.K. Bhattacharya & A.C.D. Chakklader. *Polym Plast Technol Eng* 19, 21 (1982).
- 30 V.E. Gul', L.Z. Shenfil', G.K. Mel'nikova & N.L. Maslennikova. *Sov Plast (Eng Transl)* 4, 46 (1966).
- 33 P.V. VanKonynenburg, A. Au, C. Rauwendaal & A.J. Gotcher. US Patent 4,237,441, December 2, 1980.
- 32 M. Narkis, A. Ram & Z. Stein. *J Appl Polym Sci* 25, 1515 (1980).
- 33 M. Narkis, A. Ram & Z. Stein. *Polym Eng Sci* 21, 1049 (1981).
- 34 L.L. Rohlfing, S.M. Pilgrim, R.E. Newnham & J. Runt. *J Wave-Mater Interact* 3, 301 (1988).
- 35 D. Stauffer. *Introduction to Percolation Theory*. Taylor & Francis, London (1985).
- 36 V.K.S. Shante & S. Kirlpatrick. *Adv Phys* 20, 235 (1971).
- 37 R. Zallen. *The Physics of Amorphous Solids*. Wiley, New York (1983).
- 38 V.A. Vyssotsky, S.B. Gordon, H.L. Frisch & J.M. Hammersley. *Phys Rev* 123, 5, (1961).
- 39 M. Nakamura & M. Mizuno. *J Phys C: Solid State Phys* 15, 5979 (1982).
- 40 H. Scher & R. Zallen. *J Chem Phys* 53, 3759 (1970).
- 41 S. Lee, Y. Song, T.W. Noh, X. Chen & J.R. Gaines. *Phys Rev B* 34, 10 (1986).
- 42 I. Balberg. *Philos Mag B* 56, 991 (1987).
- 43 K. Miyasaka, K. Watanabe, E. Jojima, H. Aida, M. Sumita & K. Ishikawa. *J Mater Sci* 17, 1610 (1982).
- 44 M. Sumita, S. Asai, N. Miyadera, E. Jojima & K. Miyasaka. *Colloid Polym Sci* 264, 212 (1986).
- 45 A. Voet. *Rubber Chem Technol* 54, 42 (1980).
- 46 C. Klason & J. Kubat. *Int J Polym Mater* 11, 47 (1985).
- 47 E.O. Forster. *IEEE Trans Power Appar Syst* 90, 913 (1971).
- 48 M. Narkis & A. Vaxman. *J Appl Polym Sci* 29, 1639 (1984).
- 49 L. Benguigui, J. Yacubowicz & M. Narkis. *J Polym Sci* 25, 127 (1987).
- 50 A. Malliaris & D.T. Turner. *J Appl Phys* 42, 614 (1971).
- 51 R.P. Kusy. *J Appl Phys* 48, 5301 (1977).
- 52 T.M. Aminabhavi, P.E. Cassidy & C.M. Thompson. *Rubber Chem Technol* 63, 451 (1975).
- 53 F. Carmona. *Ann Chim Fr* 13, 395 (1988).
- 54 C. Klason & J. Kubat. *J Appl Polym Sci* 19, 831 (1975).
- 55 E.V. Harris, F.E. Jones & F.C. Church. *Cabot Technical Report* RG-130.
- 56 J. Meyer. *Polym Eng Sci* 13, 462 (1973).
- 57 D. Wolfer. *Eur Rubber J* 159, 16 (1977).
- 58 F. Kohler. US Patent 3,243,753 (1966).
- 59 K. Ohn & Y. Natio. *J Appl Phys Jap* 10, 99 (1971).
- 60 J. Meyer. *Polym Eng Sci* 14, 706 (1974).
- 61 K.A. Hu, D. Moffatt, J. Runt, A. Safari & R.E. Newnham. *J Am Ceram Soc* 70, 583 (1987).
- 62 G.R. Ruschau, S. Yoshikawa & R.E. Newnham. *Int J Hybrid Microelectron* 13, 100 (1990).
- 63 K.T. Chung, A. Sabo & A.P. Pica. *J Appl Phys* 53, 6867 (1982).
- 64 F. Bueche. *J Appl Phys* 44, 532 (1973).
- 65 F. Bueche. *J Polym Sci* 11, 1319 (1973).
- 66 A.I. Medalia. *Rubber Chem Technol* 59, 432 (1986).
- 67 H. Kawamoto. *Carbon Black-Polymer Composites*. Marcel Dekker, New York, Ch. 5 (1982).
- 68 F. Bungenet & M. Popescu. *Physics of Solid Dielectrics, Materials Science Monographs* 19. Elsevier, New York (1984).
- 69 A. Von Hippel. *Dielectrics and Waves*. Wiley, New York, (1954).
- 70 R.M. Scarisbrick. *J Phys D: Appl Phys* 6, 2098 (1973).

- 71 F.J. Balta Calleja, T.A. Ezquerro, D.R. Rueda & J. Alonso-Lopez. *J Mater Sci Lett* 3, 165 (1984).
- 72 A.K. Sichel, J.I. Gittleman & P. Sheng. *J Electron Mater* 11, 699 (1982).
- 73 R.D. Sherman, L.M. Middleman & S.M. Jacobs. *Polym Eng Sci* 23, 36 (1983).
- 74 D.M. Moffatt, J.P. Runt, A. Halliyal & R.E. Newnham. *J Mater Sci* 24, 609 (1989).
- 75 F.J. Blatt. *Physics of Electronic Conduction in Solids*. McGraw-Hill, New York (1968).
- 76 A.R. Blythe. *Electrical Properties of Polymers*. Cambridge University Press, Cambridge (1979).

**APPENDIX 27**

## Percolation Constraints in the Use of Conductor-Filled Polymers for Interconnects

G.R. Ruschau, S. Yoshikawa, and R.E. Newnham  
Materials Research Laboratory  
Pennsylvania State University  
University Park, PA 16802

### ABSTRACT

Conductor-filled polymers are used in the microelectronics industry for conductive epoxies, solderless interconnects, and electrode contacts. The electrical properties of these materials are described by conventional percolation theory, which states that at a certain critical volume fraction of conductive filler, the composite transforms from an insulator to a conductor, due to the formation of the first continuous chain of filler particles.

However, theoretical percolation predictions ignore the realities encountered in the electronic fabrication. While percolation models involve statistical probabilities based on randomly-filled isometric matrices, the filling of polymeric materials with conductive filler is far from random, and the geometry of the conductive pattern is far from isometric.

In this investigation, the electrical properties of Ag-filled silicone rubber composites were studied with an emphasis on the properties of thin, flexible sheet-type samples. It was found that the critical volume fraction for conduction for a given composite system was highly dependent on the measurement geometry for a given composite component. As a consequence, the resistivity across thin composite tapes differed from the resistivity through the thickness of the tape. In some extreme cases, composites were insulators in one direction and conductors in another direction.

The two important variables in deciding the degree of anisotropy in conduction are the geometry factor,  $G$  (=area of electrode contact/distance between electrodes) and  $\Gamma$ , the ratio of the particle size to the smallest sample dimension. As  $G$  and  $\Gamma$  increased, the percolation probabilities deviated from bulk samples of the same composite. A Monte Carlo-type computer simulation of the random filling of geometrically anisotropic matrices verified that the variation in critical volume fraction with  $G$  and  $\Gamma$  in otherwise identical compositions was an expected result, following the laws of statistical probability. Thus, when formulating conductive composite compositions, the critical volume fraction for conduction is characteristic of a given system only for small values of  $G$  and  $\Gamma$ .

When the geometric restrictions are minimized, the critical volume fraction for conduction can be estimated by considering the loose packing density of the filler powder. In this way, conductive composites may be thought of as a conductive skeleton of a certain packing geometry rather than as a randomly filled particle matrix.

### INTRODUCTION

Composites consisting of highly conductive filler powder dispersed in a flexible, insulating polymer matrix are commonly used in electronic applications for die attach<sup>[1]</sup>, solderless connectors<sup>[2]</sup>, thermistors<sup>[3-4]</sup>, and pressure sensing elements<sup>[5]</sup>. Other uses of such composites include electromagnetic shielding and anti-static devices<sup>[6]</sup> as well as chemical sensors<sup>[7]</sup>.

The properties of composite systems are understood in terms of percolation phenomena: when a sufficient amount of conductive filler is loaded into an insulating polymer matrix, the composite transforms from an insulator to a conductor, the result of continuous linkages of filler particles (See Figure 1). The critical volume fraction at which this transformation occurs,  $V_c$ , is the focus of this investigation.

For percolation in a model system,  $V_c$  has been predicted for different packing geometries as a function of the lattice

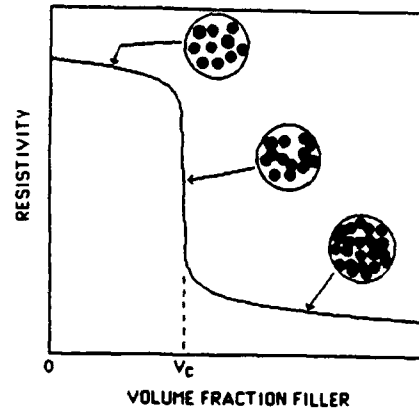


Figure 1: Percolation theory as applied to conductive composites, showing the development of conductive pathways with an increase in volume fraction of filler.

coordination, as shown in Table 1.  $V_c$ 's are given for both two-dimensional and three-dimensional systems; despite the variations in lattice packing, all  $V_c$ 's are roughly equivalent within both sets of numbers.

The predicted  $V_c$  for different packing geometries varies

Table 1: Critical volume fractions concentrations for bond ( $p_c^{bond}$ ) and site ( $p_c^{site}$ ) percolation on a variety of lattices.<sup>[8]</sup>

Lattice Type	$p_c^{bond}$	$p_c^{site}$	Lattice Coordination	Maximum Packing $\phi_m$	$\phi_m p_c^{site} = V_c$
<b>2-Dimensional</b>					
triangular	0.347	0.500	6	0.907	0.450
square	0.500	0.593	4	0.785	0.470
kagome	0.450	0.653	4	0.680	0.440
honeycomb	0.653	0.698	3	0.605	0.420
<b>3-Dimensional</b>					
Face-centered cubic	0.119	0.198	12	0.741	0.147
Body-centered cubic	0.179	0.245	8	0.680	0.167
Simple cubic	0.247	0.311	6	0.524	0.163
Diamond	0.388	0.428	4	0.340	0.146
Random cubic	---	0.270*	---	0.637	0.160

\*empirically derived

slightly depending on the type of percolation assumed. "Site" percolation assumes that the lattice sites are randomly filled until a continuous linkage is formed; continuity is assumed when adjacent lattice sites are filled. "Bond" percolation assumes that the lattice sites are filled but that adjacent lattice sites do not necessarily form a continuous linkage, but rather are randomly bonded (electrically contacted in this case) as more filler is loaded into the matrix. Predicted  $V_c$ 's for site percolation are generally higher than for bond percolation; percolation in real systems is thought to be a mixture of both site and bond percolation.

One problem with the predicted  $V_c$ 's is that real systems seldom follow these rules of lattice packing and percolation: systems which show  $V_c$  in the range of 15-17% (the predicted range from Table 1) are no more prevalent than systems showing much higher  $V_c$ 's. This makes it difficult to produce experimental results to which an appropriate mathematical model can be applied. Table 2

Table 2: Critical volume fractions for conductive composite systems by other investigators.

Filler	Polymer	$V_c$	Reference
Cu	Polyvinylchloride	.01	[9]
Cu	Polyvinylchloride	.20	[10]
Cu	Polystyrene	.15	[11]
Cu	Polystyrene	.35	[11]
Ag	Polystyrene	.36	[12]
Ag	Rigid Epoxy	.09	[13]
Ag	Rigid Epoxy	.30	[14]
Ag	Silicone Rubber	.15	[14]
Ag	Silicone Rubber	.27	[15]
Sb:SnO <sub>2</sub>	Flexible Epoxy	.30	[16]
Sb:SnO <sub>2</sub>	Flexible Epoxy	.40	[16]
Fe	Styrene / acrylonitrile	.20	[17]
Al	Styrene / acrylonitrile	.40	[17]

lists  $V_c$  for a number of conductor-filled polymers studied by other investigators, showing how  $V_c$  can vary even within the same filler/polymer system.

An important limitation on the predicted  $V_c$ 's is that the probability of percolation must be the same in all directions; i.e., the overall lattice in the two-dimensional case is a square, and the overall lattice in the three-dimensional case is a cube. For microelectronic applications, the focus is nearly always on sample geometries in which at least one dimension is exaggerated relative to the other dimensions, such as thin sheets or wires. The scaling factors involved in this type of percolation throw another variable into the system.

In this investigation, we concentrate on the properties of some silver-filled silicone rubber composites, and show how the artificial percolation restrictions effect both the critical volume fraction and resistivity of the composite. A computer simulation of the two dimensional case shows that these restrictions effect  $V_c$  in a predictable manner. An empirical method to predict  $V_c$  for non-restricted systems is presented.

### EXPERIMENTAL PROCEDURE

Silicone rubber (G.E. 845 silicone elastomer) was the matrix material used in this investigation. Relatively monosize distributions ( $\pm 10\%$ ) of each of the conductive filler powders were

used. After weighing all samples to the proper volume loading using a mixture of about 16% silicone in trichloroethylene (TCE) solvent the batches were mixed for one minute with a polyethylene propeller blade at 800 rpm.

Approximately 20% excess TCE was added to obtain the proper viscosity ( $\sim 10,000$  CPS) for tape casting. The slip was cast onto 6"x8" borosilicate glass sheets using a doctor blade thickness of 1.5mm, which resulted in a final sample thickness of 0.25-0.30mm. After air drying for 4 hours, the samples were cured at 180°C for 2 hours then removed from the glass sheets with a razor blade and cut into 2cm x 5cm rectangular samples.

Percolation was verified by measuring the d.c. electrical resistance of three to six samples of each formulation and thickness was measured across each sample by a 4-probe measurement technique using gold-plated leads and a digital multimeter. Percolation was assumed when the resistivity was closer to the resistivity of the filler material (ranging from  $10^{-6}$  to  $10^{-4}$   $\Omega$ -cm) than to the resistivity of the silicone rubber ( $10^{12}$   $\Omega$ -cm). SEM analysis was used to verify the random dispersion of the filler within the system.

In order to determine the scaling effects on model percolation systems, critical volume fraction variations with sample geometry and particle size were calculated for a square lattice using a two-dimensional Monte Carlo-type program, written in BASIC language. All simulations were performed on a Macintosh SE computer.

The basic parts of the program were as follows:

1. The desired dimensions of the overall sample (vertical and horizontal lengths of a rectangle) were entered.
2. The desired filler "particle" size was entered.
3. An internal random number generator was used to randomly select a lattice site and place a "particle" on that lattice site; the output was displayed graphically on screen.
4. After filling a lattice site, the program automatically checked for percolation in the vertical direction. If the system was percolated, the critical volume percent (actually, an area percent since the program was two-dimensional) was calculated by the following:

$$V_c(\%) = \frac{(\pi/4) (\# \text{filled lattice sites})}{(\text{total } \# \text{ lattice sites})} \times 100\% \quad (1)$$

5. If percolation was not detected, more lattice sites were filled until percolation was detected.
6. After recording the critical volume percent, the program was repeated with the same parameters for a total of twenty separate simulations for each geometry and particle size variation.

This computer simulation was very similar to the traditional Monte Carlo statistical analyses of random processes, although the graphics output and percolation detection algorithm were limited to two-dimensional simulations only.

The packing densities for all fillers used were measured using a 10 cc graduated cylinder with 0.1 cc graduations. Approximately 5 cc of the powder was weighed in the cylinder, then caused to settle by rattling the cylinder lightly on the counter top for 30 seconds (approximately 500 "taps") to simulate the technique used commercially for tap density measurements. The volume of the settled powder was estimated to the nearest 0.05 cc. Thus the packing fraction,  $\phi_p$ , was calculated by the formula:

$$\phi_p = (w_f/V_t) / \rho_f \quad (2)$$

where  $w_f$  = measured weight of powder sample  
 $V_t$  = volume of tapped powder  
 $\rho_f$  = theoretical density of filler powder

### RESULTS AND DISCUSSION

#### A. Geometry Ratios

Figure 2 illustrates (with 9.0  $\mu\text{m}$  Ag powder-filled silicone rubber) how  $V_c$  can vary with sample thickness (which was varied

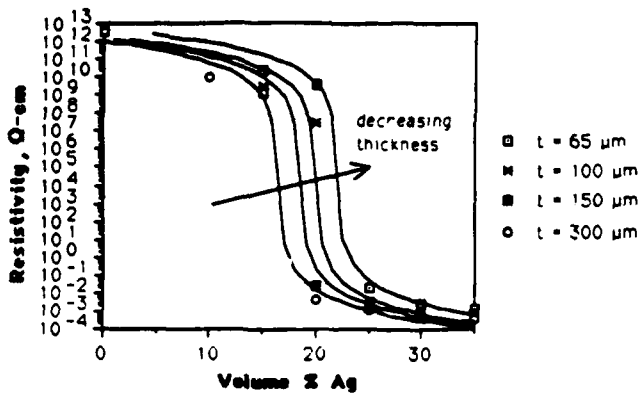


Figure 2: Percolation curves (with mathematical curve fits) for 9.0  $\mu\text{m}$  Ag powder-filled silicone rubber composites.

by casting with different doctor blades) for otherwise identical samples. While the thickest samples appear to percolate at ~18 vol%, the thinnest samples require more filler to reach a low resistivity. This effect is much less pronounced in Figure 3, which

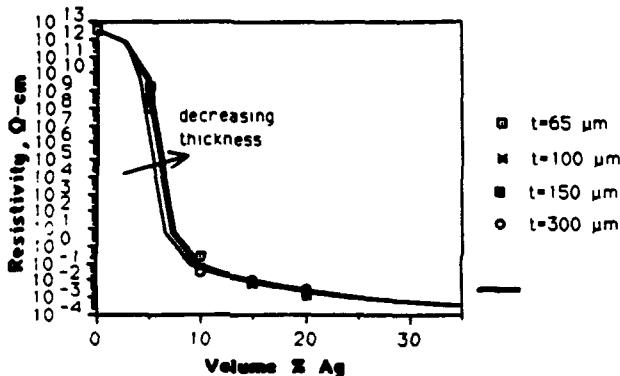


Figure 3: Percolation curves (with mathematical curve fits) for 0.5  $\mu\text{m}$  Ag powder-filled silicone rubber composites.

shows the same thickness variations for 0.5  $\mu\text{m}$  Ag powder-filled silicone rubber.

This same trend was seen repeatedly in samples of other compositions. As the average particle size ( $d$ ) decreased relative to the sample thickness ( $t$ ) the limitations imposed by sample geometry were not as severe. When one dimension of the sample was the same order of magnitude as the particle size, the greatest variation in properties occurred. In terms of site percolation, the probability of continuing a percolation path (i.e., filling an adjacent lattice site) was always greater for a particle in the bulk of the composite than for a particle at the surface, simply because there were more possible directions (i.e., more adjacent lattice sites) for the path to continue. The larger the particle size relative to the sample thickness (or the lower the  $t/d$  ratio, which we call  $\Gamma$ ), the greater the percentage of particles occupying positions at the surfaces.

Clearly, the overall geometric factor for the resistivity calculation was the most important number to consider. This geometric factor,  $G$ , for any sample is given by:

$$G = A/L \quad (3)$$

where  $A$  is the effective electrode area, and  $L$  is the distance between the electrodes. For samples such as those in Figs. 2 and 3,

$L$  was a constant (2.5 cm) and  $A = (\text{sample thickness} \times \text{width})$ , where width = 1.5 cm. The sample thickness varied from 50  $\mu\text{m}$  to 250  $\mu\text{m}$ , so the overall geometry factor varied from 0.0024 cm to 0.0150 cm. Geometry factors less than 1.0 cm may be termed as "unfavorable" geometries for percolation, especially when  $\Gamma$  is small.

Conversely, geometries with  $G > 1.0$  cm may be termed as "favorable" geometries for percolation. This implies that the samples in Figure 3 would show very different behavior if measured through the thickness rather than across the thickness. Figure 4 shows the variation in  $V_c$  for the samples in Figure 3 as the

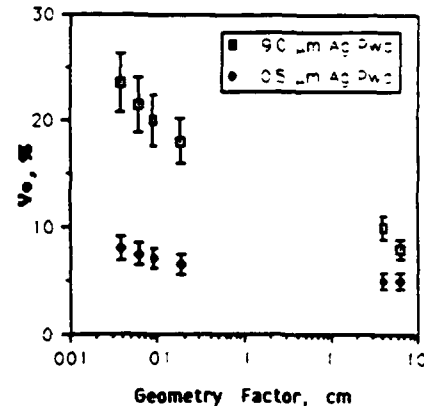


Figure 4: Variation in  $V_c$  for the samples shown in Figures 2 and 3 as a function of geometry factor.

geometry factor goes from unfavorable to favorable for percolation. With  $G > 1$ , a small  $\Gamma$  becomes more favorable for percolation.

### B. Monte Carlo Simulation

Monte Carlo percolation simulations, in which a lattice of a given geometry is filled randomly, are useful due to their ability to generate an accurate distribution of percolation probabilities. In this case, a Monte Carlo-type algorithm was used to illustrate what happens to percolation probabilities for a square lattice when  $G$  and the  $\Gamma$  are altered.

Figure 5 is an example of the graphics of the program output for the Monte Carlo algorithm, with percolation checked between the cross-hatched "electrodes" for each simulation. Since

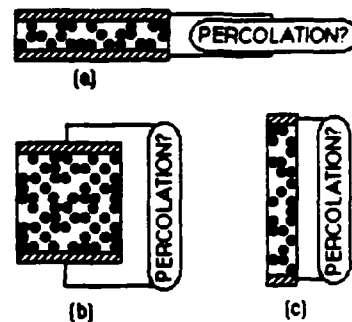


Figure 5: Graphics output from the Monte Carlo percolation simulation for (a) favorable percolation geometry ( $G=5.0$ ), (b) neutral geometry ( $G=1.0$ ), and (c) unfavorable percolation geometry ( $G=0.2$ ).

the program was a two-dimensional simulation only, the geometry factor was the vertical dimension of the "sample" divided by the horizontal dimension.

Figure 6 shows the calculated two-dimensional critical

volume fractions (actually, critical area fractions for two dimensions) as a function of (a)  $\Gamma$ , and (b)  $G$ . Clearly, as the

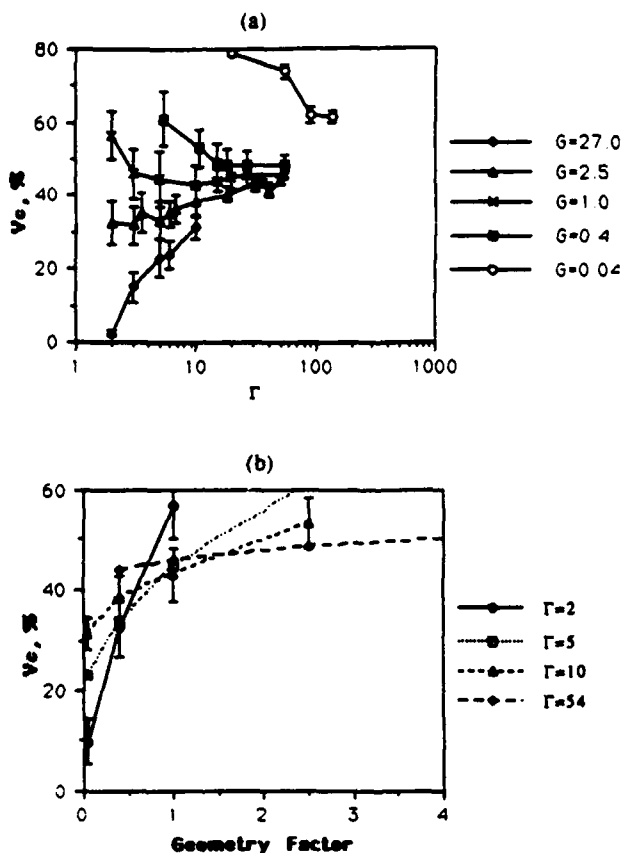


Figure 6: Results from the two-dimensional Monte Carlo percolation simulation of  $V_c$  as a function of (a) the particle size/sample thickness ratio,  $\Gamma$ , and (b) the geometry factor,  $G$ .

geometry factor increases, the critical volume fractions increase for all  $\Gamma$ , with the most dramatic changes occurring for low  $\Gamma$  (relatively large particles in thin samples, which is the case in Fig. 2). As  $\Gamma$  increases, as indicated in Fig. 6(b), the curves for all the geometric factors converge to a value near 47%, which is the predicted  $V_c$  for the square lattice from Table 1. Similar trends would be expected for a Monte Carlo simulation of the three-dimensional case, with the predicted  $V_c$ 's converging to the value of 16.3% for simple cubic packing.

It was also interesting to note that the standard deviation in the data consistently decreased as  $\Gamma$  increased; this was consistent with the theory of statistics, which implies that higher accuracy is always obtained when the sampling lot (in this case, the number of lattice sites) is greater. This also had implications for the reproducibility behavior of many of the samples; reproducibility improved as  $\Gamma$  increased and as  $G \rightarrow 1$ .

The predicted critical volume fractions in Table 1 assume not only specific packing geometries, but also assume that each system percolates in all directions with equal probability. In all cases, the overall lattice must have  $G=1.0$ . In practice, therefore, "the" critical volume fraction for conduction in a conductor-filled polymer can be compared to the predicted values in Table 1 only when cube-shaped samples are measured, in which  $G=1.0$ , and when  $\Gamma$  is very large.

### C. Geometry Effect on Resistivity

As shown in the previous section,  $G$  and  $\Gamma$  can have a profound effect on the measured properties of a composite sample because of the inhomogeneous nature of the composite. The choice of direction across which the electrical resistivity is measured can determine if a composite appears to be an insulator or a conductor. Thus, sometimes sample resistivities are not directly comparable.

These data are readily explained by considering the general behavior of a composite near the percolation threshold. Figure 7

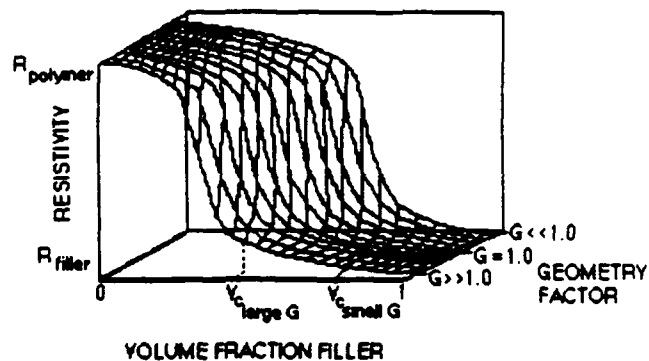


Figure 7: Qualitative representation of the percolation behavior of composites as a function of the geometry factor, illustrating the effects of a shift in  $V_c$  on the resistivity for a given volume fraction of filler.

illustrates the percolation curve for a typical composite as a function of  $G$ . The resistivity drops sharply when percolation first occurs. At the base of the percolation threshold, there is a broad region in which the connectivity is incomplete. It is in this region that samples with smaller  $\Gamma$  were often found; thus potentially low resistivity samples are limited by the incomplete percolation.

### D. Packing Fractions, Morphology, and $V_c$

Even if  $G=1$  and  $\Gamma$  is large,  $V_c$  is rarely in the predicted range of 14-17%. Janzen first introduced the notion that critical volume fractions could not be adequately treated by traditional percolation theory (even for isotropic matrices), in which perfect spheres arranged in ideal packing geometries are assumed.<sup>(18)</sup> He proposed that  $V_c$  for carbon black-filled polymers used as anti-static mats must be related to the specific void space for a pure filler material, that is, the ability (or inability) of a filler to pack to a certain density. Thus the critical volume fraction for a certain filler material can be estimated by knowing this variation.

Table 3 lists the results of the measured packing fractions,  $\phi_p$ , and the observed critical volume fractions for a number of Ag and Ag-coated powders investigated, along with average particle sizes. A very good correlation between  $\phi_p$  and  $V_c$  was observed for all samples;  $V_c$  was normally about 0.05 below  $\phi_p$ . Thus, conductive composites may be thought of as a conductive skeleton of a certain packing lattice; this packing lattice is the distinguishing feature for most powders.

Figure 8 shows the relationship between  $\phi_p$  and particle size for polygonal Ag powders of a narrow size distribution, and very spherical Ag-coated powders of a narrow size distribution;  $V_c$  values were left off for clarity. The trend in both cases is the same: smaller particles pack less densely than larger particles, and as such result in lower  $V_c$  when composites are formulated (as indicated by the data in Table 3). The actual  $\phi_p$  values for the polygonal powders are not comparable to  $\phi_p$  for spherical powders, however. Spheres tend to pack much more densely than the more irregularly-shaped

Table 3: Packing fractions and critical volume fractions for Ag and Ag-coated filler in silicone rubber.

Filler	Avg. Particle Size, $\mu\text{m}$	$\phi_p$	Observed $V_c$
<b>Polygonal powders</b>			
Ag <sup>†</sup>	0.5	0.07	0.05
Ag <sup>†</sup>	1.0	0.11	0.10
Ag <sup>†</sup>	4.0	0.17	0.16
Ag <sup>†</sup>	5.0	0.22	0.15
Ag <sup>†</sup>	9.0	0.27	0.20
<b>Spherical powders</b>			
Ag:TiO <sub>2</sub> <sup>‡</sup>	1.0	0.19	0.15
Ag:Ni <sup>‡</sup>	5.0	0.31	0.25
Ag:Phenolic Resin <sup>‡</sup>	5.0	0.29	0.25
Ag:Phenolic Resin <sup>‡</sup>	12.0	0.39	0.30
Ag:Phenolic Resin <sup>‡</sup>	15.0	0.46	0.40
Ag:Phenolic Resin <sup>‡</sup>	35.0	0.56	0.50

<sup>†</sup> Metz Metallurgical Corp.  
<sup>‡</sup> Mitsubishi Metal Corp.  
<sup>\*</sup> Novamet Specialty Products Corp.

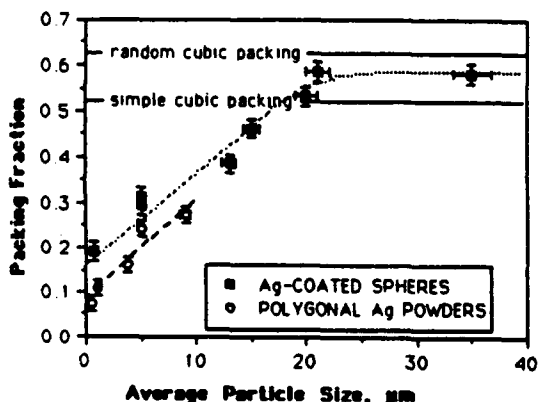


Figure 8: Measured packing fractions for spherical and polygonal fillers as a function of average particle size.

polygonal powders. Non-spherical powders normally show a greater tendency for "bridging" in compacts. Bridging led to lower packing densities and lower  $V_c$  in all cases. This bridging is especially significant when fibers and flakes are used as fillers.

This was consistent with the theory of particle packing.<sup>(19)</sup> Packing density decreases with smaller particle size due to an increase in surface area, lower particle mass, and a greater significance of the weak short-range forces. These short range forces include electrostatic fields and surface adsorption of moisture and other wetting liquids leading to agglomeration.

An additional effect was the shifting in  $V_c$  to lower volume fractions which occurred when the particle size was decreased, as illustrated in Figure 9. Near  $V_c$  for a coarse filler, the same volume fraction filler will produce lower resistivity composites with fine powders. As the volume fraction of filler is increased beyond the  $V_c$  region, the coarse fillers will eventually produce lower resistivity composites. The reasons for this<sup>(20)</sup> will not be described here.

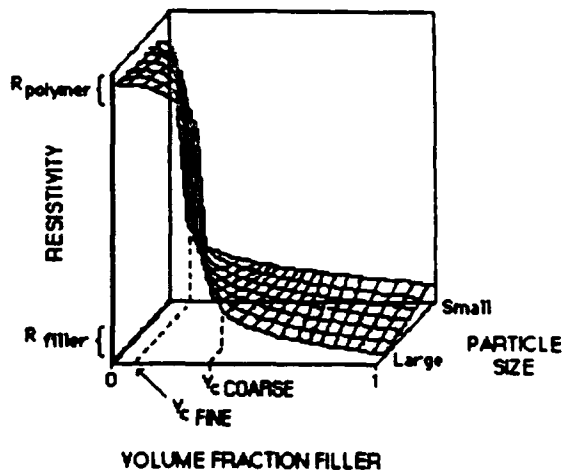


Figure 9: Qualitative representation of the percolation behavior of composites of identical chemical composition but varying particle size.

### CONCLUSIONS

Critical volume fractions for one conductor/polymer system can be compared to another system only when a neutral geometry is measured, and when the filler particle size is very small relative to any one dimension of the sample. Minimizing  $\Gamma$  also minimizes the effects of sample geometry. As  $G \rightarrow 1$  and  $\Gamma$  increases, the reproducibility improves and  $V_c$  can be estimated by measuring the packing fraction of the loose filler material. The rules of particle packing then apply to composites, and trends in  $V_c$  with filler variation can be predicted. In the same way that sample geometry restrictions affected  $V_c$ , the same restrictions affected resistivity. Samples with small geometry factors tended to have larger resistivities, particularly when  $\Gamma$  was relatively large.

Thus, when considering the use of conductor-filled polymers for electrical interconnects, in which the geometry of the conductor is often specified by circuit design, the size and morphology of the conductive filler material should be chosen specifically for the application. Fine particle sizes produce the most geometry-independent samples for these applications, but when the lowest possible resistivity is desired, there is an optimum particle size for the stated geometry.

### REFERENCES

- R.L. Opila, and J.D.Sinclair, "Electrical Resistivity of Silver-Filled Epoxies for Die Attach," *Ann.Proc.Reliab.Phys.Symp.* 23, 164 (1985).
- G.E. Pike, "Electrical Properties of Conducting Elastomers," *Sandia Lab.Tech.Rep* 81-0263 (1981).
- K.A. Hu, D.Moffatt, J.Runt, A.Safari, and R.E.Newnham, " $V_2O_5$ -Polymer Composite Thermistors," *J.Am.Cer.Soc.* 70, 583-585 (1987).
- L.L. Rohlifing, R.E.Newnham, S.M.Pilgrim, and J.Runt, "Multiphase Composite PTC Thermistors," *J.Wave-Mat.Int.* 3, 273-281 (1988).
- S. Yoshikawa, T.Ota, and R.E.Newnham, "Piezoresistivity in Polymer-Ceramic Composites," *J.Am.Ceram.Soc.* 73, 263-267 (1990).
- S.K. Bhattacharya, *Metal-Filled Polymers*, Marcel-Dekker, New York, 1986.
- G.R. Ruschau, R.E.Newnham, J.Runt, and B.E.Smith, "0-3 Ceramic-Polymer Composite Chemical Sensors," *Sens. & Act.* 20, 269-275 (1989).

8. Zallen, R., The Physics of Amorphous Solids, Wiley, New York, 1983.
9. Das, D., S. Basu, and A. Paul, "PVC-Cu Composites with Chemically Deposited Ultrafine Copper Particles," J. Mat. Sci. 15, 1719-1723 (1980).
10. Bhattacharya, S.K., S. Basu, and S.K. De, "Effect of Temperature on the Electrical Conductivity of Poly(vinyl Chloride)-Copper Composites," J. Appl. Pol. Sci. 25, 111-118 (1980).
11. Pierre, C., R. Deltour, A.J. Perenboom, and P.J.M. Van Bentum, "Electrical Conduction Mechanisms in Polymer-Copper Particle Composites. I. Temperature and High-magnetic Field Dependence of the Conductivity," Phys. Rev. B. 42, 3380-3385 (1990).
12. Matsushita, R., M. Senna, H. Kuno, "Electrical Resistivity of Hot-Pressed Silver-Polystyrene Powder Mixture," J. Mat. Sci. 12, 509-516 (1977).
13. Pujol, J.M., C. Prud'homme, M.E. Quenneson, and R. Cassat, "Electroconductive Adhesives: Comparison of Three Different Polymer Matrices. Epoxy, Polyimide, and Silicone," J. Adhes. 27, 213-229 (1989).
14. Schoch, K.F., and A.I. Bennett, "Electrical Evaluation of Conductive Adhesives," IEEE Proc., 291-293 (1985).
15. Miller, B., "Polymerization Behavior of Silver-Filled Epoxy Resins by Resistivity Measurements," J. Appl. Poly. Sci. 10, 217-228 (1966).
16. Ota, T., I. Yamai, J. Takahashi, S. Yoshikawa, and R.E. Newnham, "Effects of Filler Particle Size on the Electrical Resistance of Conductor-Polymer Composites," presented at the Second International Ceramic Science and Technology Congress, 1990.
17. Nicodemo, L.L. Nicolais, G. Romeo, and E. Scafora, "Temperature Effect on the Electrical Resistivity of Metal/Polymer Composites," Polymer Eng. and Sci. 18, 293-298 (1978).
18. Janzen, J., "On the Critical Conductive Filler Loading in Antistatic Composites," J. Appl. Phys. 46, 966-968 (1975).
19. German, R.M., Particle Packing Characteristics, Metal Powders Industries Federation, Princeton, N.J., 1989.
20. Ruschau, G.R., and R.E. Newnham, "Critical Volume Fractions in Conductive Composites," J. Comp. Matl., in press.

**APPENDIX 28**

**The Volume Fraction and Temperature  
Dependence of the Resistivity in Carbon Black  
and Graphite Polymer Composites: An Effective  
Media - Percolation Approach**

*Michael Blaszkiwicz, David S. McLachlan\*, and  
Robert E. Newnham*

Materials Research Laboratory,  
The Pennsylvania State University,  
University Park, Pa 16802.

\* Permanent address: Department of Physics,  
University of the Witwatersrand,  
Johannesburg, South Africa

## ABSTRACT

A quantitative general effective media (GEM) equation is used to describe a broad range of experimental resistivity-volume fraction results for graphite-polymer and carbon black-polymer composites. The parameters used are the resistivities of each component and the two percolation morphology parameters, a critical volume fraction,  $\phi_c$ , and an exponent,  $t$ . A preliminary model, also based on the GEM equation, is used to describe the temperature variation of the resistivity of the diphasic material near the critical volume fraction.

## INTRODUCTION

Since the 1930's carbon black fillers in resistive polymer matrices have been used to make commercial conductive and antistatic compounds.<sup>1</sup> The resistivity of the diphasic composites varies as a function of the volume fraction of the conducting material. A resistivity-volume fraction graph has three major regions: (1) the low-loading region of carbon black in which the resistivity of the polymer dominates, (2) the percolation region where a small increase in the loading can bring about a large decrease in the resistivity of the composite, and (3) the high loading region of carbon black in which the resistivity approaches that of carbon black.<sup>2</sup>

## THE GENERAL EFFECTIVE MEDIA (GEM) EQUATION

Considerable experimental and theoretical work has been done to examine and to explain how the volume fractions and the morphology of the components affect the electrical behavior of the composite materials (see for example Reference 2). Previous theoretical work has relied on percolation and effective media theories. Percolation theory<sup>3,4</sup> is limited in that it is valid only when the ratios of the resistivities of the two components are infinite.<sup>5</sup> This can be a problem when dealing with real systems where all components have finite resistivities.

Effective media theories<sup>4</sup> are used to try to predict the effective or large-volume average of the electrical conductivity, dielectric constant, thermal conductivity, gaseous diffusion, and magnetic permeability of composites. There are two special cases for which effective media theories exist, the

symmetric and asymmetric cases.<sup>4</sup> The symmetric case assumes that a random mixture of spherical (oriented ellipsoidal) particles of two (or more) components completely fill all space. In the asymmetric case the surfaces of the particles of one component (the filler) are always completely covered by the other component (the matrix). The filler or particle sizes are assumed to have an infinite range in the derivation of both theories. When one component is a perfect insulator, the symmetric media theory contains a conductor-insulator transition at a specific conductor volume fraction, which depends on the shape of the particles, whereas the asymmetric theory does not.<sup>4</sup> In practice, conductor-insulator transitions occur over a wide range of volume (or area in two dimensions) fractions (see for instance References 6-11).

A generalized effective media (GEM) equation with two morphology parameters,  $\phi_c$  and  $t$ , has been proposed by McLachlan.<sup>6</sup> It was derived as an interpolation between the symmetric and asymmetric effective media theories. The GEM equation written in terms of electrical conductivity is:

$$\frac{(1-\phi)\left(\sigma_l^{1/t} - \sigma_m^{1/t}\right)}{\sigma_l^{1/t} + \left(\frac{1-\phi_c}{\phi_c}\right)\sigma_m^{1/t}} + \frac{\phi\left(\sigma_h^{1/t} - \sigma_m^{1/t}\right)}{\sigma_h^{1/t} + \left(\frac{1-\phi_c}{\phi_c}\right)\sigma_m^{1/t}} = 0 \quad (1)$$

where  $\phi$  is the volume fraction of the high conductivity component, and  $\phi_c = 1 - f_c$  is the critical volume fraction of the high conductivity component at which a percolation path is formed through the media by the high conductivity component. Here,  $\sigma_l$  is the conductivity of the low conductivity component,  $\sigma_h$  is the conductivity of the high conductivity component,  $\sigma_m$  is the conductivity of the medium itself, and  $t$  is an exponent. Equation 1 reduces to the symmetric and

asymmetric theories and has the mathematical form of the percolation equation in the appropriate limits.<sup>6</sup>

The GEM equation can also be viewed as a matched asymptotic expression as it interpolates between the two percolation equations given below. When  $\sigma_l = 0$ , the GEM equation reduces to:

$$\sigma_m = \sigma_h (1 - f / f_c)^t \quad (2)$$

and when  $\sigma_h = \infty$ ,  $\rho_h = 1/\sigma_l$ ,  $\rho_l = 1/\sigma_h$  it becomes:

$$\rho_m = \rho_h (1 - \phi / \phi_c)^t \quad (3)$$

where the critical volume fraction is  $\phi_c = 1 - f_c$  and where  $\phi = 1 - f$ . This is illustrated in Fig. 1 where Eqs. 1, 2, and 3 are plotted for the typical three dimensional morphology parameters  $f_c = 0.84$  ( $\phi_c = 0.16$ ) and  $t = 1.7$  with  $\sigma_h = 1 = \rho_l$  and  $\sigma_l = 10^{-6}$  or  $\rho_h = 10^6$ . This figure clearly indicates where the percolation equations will not suffice and the GEM equation must be used.

When  $f_c = 1$  or  $\phi_c = 1$  equations (2) and (3) are both forms of the Bruggeman asymmetric equation<sup>4</sup> which allows values for  $L$ ,  $L'$ ,  $m$ , and  $m'$  to be calculated from the corresponding exponent in the asymmetric media theory [6,12,13], which gives:

$$L = 1 - f_c / t, L' = f_c / t, m = t / f_c, m' = t / \phi_c. \quad (4)$$

Values of  $m$  and  $m'$  as functions of the demagnetization coefficient  $L_c \neq (L_b = L_a)$  calculated for  $\sigma_l = 0$  and  $\sigma_h = \infty$ , respectively, from equation (23) in Reference 13, are plotted in Reference 6.

The GEM equation has been used to accurately fit a vast amount of conductivity data.<sup>6-11</sup> It has also been used to fit the electrical and thermal conductivities, and the experimental permeability data from a series of sintered nickel samples (0.14 - 0.95 volume fraction of nickel) while using the same two morphology parameters,  $f_c$  and  $t$ .<sup>7</sup>

This article reports how the GEM equation was used to quantitatively fit the resistivity versus volume fraction data for carbon black-eccogel and graphite-eccogel composites. Also, the temperature coefficient of resistivity for a 47 volume percent graphite sample was modelled using the GEM equation.

### FITTING PROCEDURE

The experimental resistivity vs. volume fraction data for the graphite- and for the carbon black (Vulcan XC-72R)- eccogel (1365-0) epoxy systems<sup>14</sup> were fitted to the GEM equation. The parameters  $f_c$ ,  $t$ ,  $\rho_h$  (the resistivity of the polymer) =  $1 / \sigma_l$ , and  $\rho_l$  (the resistivity of the conductive filler) =  $1 / \sigma_h$  were varied freely. The computer program uses an IMSL non-linear regression fitting program, the experimental conductivity (volume fraction) and the variable parameters to calculate a volume fraction (conductivity) called Calc from Eq.1. Calc is then compared to the actual volume fraction (conductivity) called Expt. The sum of the squares of the residuals, called SSQ:

$$SSQ = \sum_n [(Calc - Expt)]^2 \quad (5)$$

is minimized by the computer program for the  $n$  data points.

## RESISTIVITY-VOLUME FRACTION RESULTS

Figure 2 shows the experimental data<sup>14</sup> for the resistivities measured at 25° C for varying volume fractions of carbon black and of graphite in eccogel and the corresponding theoretical fits of the GEM equation.

The parameters used to generate the theoretical curves are:  $\rho_{gr} = 0.087 \Omega \cdot \text{cm}$ ,  $\rho_{poly} = 1.30 \times 10^{10} \Omega \cdot \text{cm}$ ,  $\phi_c = 0.421$  and  $t = 3.00$  for the graphite composites, and  $\rho_c = 1.15 \times 10^{-4} \Omega \cdot \text{cm}$ ,  $\rho_{poly} = 8.30 \times 10^9 \Omega \cdot \text{cm}$ ,  $\phi_c = 0.074$  and  $t = 4.50$  for the carbon black composites.

Note that the values of the exponent  $t$  are higher than that of the universal value of  $t$  ( $= 1.65$  for three dimensions) in percolation theory.<sup>3</sup> However, the non-universality of  $t$  is not anomalous as the value of  $t$  has been shown to be dependent upon the particular conduction mechanism of the composite.<sup>15</sup>

The two systems examined in this article show behavior similar to the systems of segregated and random distributions of filler particles in a polymer matrix.<sup>16</sup> The carbon black composites show segregated distribution behavior which occurs in systems in which the filler particles are much smaller than those of the polymer.<sup>17,18</sup> (The value of  $\phi_c = 0.074$  is within the practical limit of  $\phi_c \leq 0.03$  given by Kusy.<sup>18</sup>) The graphite composites have a  $\phi_c$  higher than the expected value of 0.16 for random distribution behavior which occurs in systems in which the filler particles are of comparable size to those of the polymer.<sup>17,18</sup> The probable reasons for this are discussed in the conclusion. However, note that the critical volume fractions of composites have been shown to be dependent upon the number of contacts per filler particle.<sup>3,19</sup>

The carbon black composite has a low value of  $L' = 0.0165$  or a high value of  $m' = 61$  which corresponds to a very large prolate  $c/a$  or length-to-cross-section ratio (see Reference 6, Fig. 1). The carbon black particles can be

viewed as forming long aggregate chains with the large  $c/a$  ratios corresponding not to the individual carbon black particles, but to the aggregate chains formed by the particles. This kind of fine filler network structure is clearly shown by the carbon black in the carbon black-polymer composites of Michels et al.<sup>20</sup> which have a percolation threshold below 0.02 weight percent carbon black and a  $t$  of 2.1, as determined by percolation theory.

The graphite composite has a higher value of  $L' = 0.14$  or a lower value of  $m' = 7.1$ . These values of  $L'$  or  $m'$  could correspond to "prolate" graphite chains, with a shorter length-to-area ratio than the carbon black chains, but it is more likely that it represents the intrinsic demagnetization factor of random oblate or flake-like graphite particles (see Reference 6, Fig. 1). The  $\phi_c$  for the graphite (0.421) is very similar to that of  $Fe_3O_4$  particles in eccogel.<sup>21</sup> The  $Fe_3O_4$ -eccogel system can be modelled as random spherical-like  $Fe_3O_4$  particles ( $L' = 0.333$ ,  $m' = 3.0$ ) in which the interparticle contacts are somewhat limited due to a partial wetting of the  $Fe_3O_4$  by the polymer. The number of contacts per particle is certainly greater for carbon black than for graphite, as the greater the number of contacts per particle, the lower the value of  $\phi_c$ .<sup>3,19</sup>

### MODELLING OF THE TEMPERATURE COEFFICIENT OF RESISTIVITY

The GEM equation was used to model the positive temperature coefficient of resistivity (PTC) in a 47 volume percent graphite-eccogel composite. Since the resistivity of these composites depends upon the average number of contacts per particle, it is assumed that the average number of contacts per particle changes with the temperature. In percolation theory the pure bond problem predicts the average number of contacts per particle to be

$P_b z$  (or  $\phi_c z$ ) = 1.5 at  $\phi_c$ ,<sup>3,19</sup> where  $P_b$  is the critical bond percolation probability and  $z$  is the number of nearest neighbor particles in the "lattice" or random packing of spheres. Therefore, it will be the number of contacts between nearest neighbors,  $z$  ( $\propto 1/\phi_c$ ), which changes as a function of temperature.

In the first attempt to model the PTC in a composite, a linear dependence of the number of contacts per particle on the temperature was assumed. The equation used to model the PTC effect assumes that at some critical temperature,  $T_c$ , the critical volume fraction,  $\phi_c$ , becomes equal to the actual volume fraction  $\phi$ :

$$\phi_c(T) = \phi / (1 - m(T - T_c)) \quad (6)$$

where  $m$  is a multiplier and  $\phi$  is the volume fraction of graphite. The experimental data are fitted by substituting Eq. 6 for  $\phi_c$  in the GEM equation (Eq. 1). The five variable parameters for the fit are  $t$ ,  $\sigma_l$ ,  $\sigma_h$ ,  $T_c$ , and  $m$  with  $\phi$  being fixed. Initially, the equation used to attempt to fit the data was:

$$\phi(T) = \phi_c (1 - m(T - T_c)) \quad (7)$$

where at some temperature  $T_c$ , the volume fraction at room temperature,  $\phi$ , which is a function of temperature, would become equal to the critical volume fraction,  $\phi_c$ . Equation 7 did not fit the data satisfactorily. Equation 6 followed when the temperature dependence was improperly shifted from  $\phi$  to  $\phi_c$ . Although Eq. 6 is empirical, it fit the data quite reasonably and was used to analyze the data.

## EXPERIMENTAL RESULTS

Figure 3 shows the experimental data and two theoretical fits for the resistivity temperature dependence of a 47 volume percent graphite composite.<sup>14</sup> The data are only shown over the limited temperature range where the resistivity does not change rapidly with temperature because the simplistic linear model was only valid in this region.

The parameters used to generate the solid line in Figure 3 are  $\rho_{gr} = 3.29 \Omega \cdot \text{cm}$ ,  $\rho_{poly} = 10^{12} \Omega \cdot \text{cm}$ ,  $t = 3.67$ ,  $T_c = 72.5^\circ \text{C}$ , and  $m = 0.0141$ . These parameters are obtained using the starting values of  $t$ ,  $\rho_{gr}$ , and  $\rho_{poly}$  from the resistivity-volume fraction data of the graphite composite, a  $T_c$  in the mid-temperature range, and an appropriately small value of  $m$ . The resistivities of the graphite and of the polymer derived from this fit are inconsistent with the values derived from the volume fraction results in that the above resistivities ( $\rho_{gr}$  and  $\rho_{poly}$ ) are two orders of magnitude higher than those used to generate the theoretical lines in Fig. 2. In an attempt to have consistency in these resistivities for both the temperature dependent results and the volume fraction results, the resistivities of the graphite and the polymer were fixed to the resistivities given by the volume fraction results ( $\rho_{gr} = 0.087 \Omega \cdot \text{cm}$  and  $\rho_{poly} = 1.30 \times 10^{10} \Omega \cdot \text{cm}$ ) in the fitting program; this results in the dashed line shown in Figure 2. The results of this three parameter fit to the data are  $t = 8.89$ ,  $T_c = 66.2^\circ \text{C}$ , and  $m = 0.0460$ . Given the crudeness of the model, (i.e., a linear approximation and not accounting for the resistivity temperature dependence of the separate components of the composite), the theoretical fits to the experimental data are reasonable. Although the values of  $t$  for the PTC effect seem to be high, they cannot be compared to other values of  $t$  since they may not describe a physical

process. However, a more realistic model for  $\phi_c(T)$  may result in lower values of  $t$ .

## CONCLUSION

The general effective media (GEM) equation has been used to quantitatively fit the resistivity-volume fraction data for graphite-polymer and carbon black-polymer composites. The low values of  $\phi_c$  and the demagnetization coefficients,  $L'$  and  $m'$ , (and the associated  $c/a$  ratios) strongly suggest a segregated or fine network distribution for the carbon black composite. Structures of this nature have been observed in a similar system by Michels et al.<sup>20</sup> The high value of  $\phi_c$  and the values of  $L'$  and  $m'$  for the graphite suggests a random array of graphite flakes ( $L' \approx 0.14$  or  $c/a \approx 1/6$ ), which do not always contact each other at the points of closest approach. In the language of percolation theory, this means that the bond probability between adjacent sites (filler particles) is less than one, due to the partial wetting of the graphite by the polymer, to give site-bond percolation.

A more detailed account of effective media and percolation theories as well as the derivation and properties of the GEM equation are given in a review article.<sup>21</sup>

A preliminary attempt to model the positive temperature coefficient of resistivity (PTC) of a graphite composite near the critical volume fraction,  $\phi_c$ , using a simplistic linear model produced reasonable fits to the experimental resistivity-temperature data. The model assumed that the number of contacts per particle changed linearly with temperature. However, the large values of

the  $t$  parameter suggest that better theoretical models for  $\phi_c(T)$  are needed to fully elucidate this effect.

### ACKNOWLEDGEMENT

One of the authors, DSM, would like to thank Professor R.E. Newnham, the staff, and the students of the Materials Research Laboratory of the Pennsylvania State University for their support and hospitality during the period in which much of this work was carried out.

## References

1. Norman, R.H., Conductive Rubbers and Plastics, p. 3, Applied Science Publishers Ltd., London (1970).
2. Medalia, A.I., *Rubber Chemistry and Technology* **59**, 432 (1987).
3. Zallen, R., The Physics of Amorphous Solids, Chapter 4, Wiley, New York (1983).
4. Landauer, R., in Electrical Transport and Optical Properties of Inhomogeneous Media, Vol. 5, pp. 2-45, Edited by Garland, J.C., and Tanner, D.B., American Institute of Physics Conference Proceedings, No. 40 (1978).
5. Straley, J.P., in Percolation Processes and Structures, Vol. 5, pp.353-366, Edited by Deutscher, G., Zallen, R., and Adler, J., Annals of the Israel Physical Society (1983).
6. McLachlan, D.S., *J. Phys. C* **20**, 865 (1987).
7. Deprez, N., McLachlan, D.S., and Sigalas, I., *Solid State Comm.* **66**, 869 (1988).
8. McLachlan, D.S. and Burger, J.P., *Solid State Comm.* **65**, 159 (1988).
9. McLachlan, D.S., *Jpn. J. Appl. Phys.* **26**, Suppl. 26-3, 901 (1987).
10. McLachlan, D.S., *Solid State Comm.* **69**, 925 (1989).
11. McLachlan, D.S., *J. Phys. C* **21**, 1521 (1988).
12. Sen, P.N., Scala, C., and Cohen, M.H., *Geophysics* **46**, 781 (1981).
13. Meredith, R.E., and Tobias, C. W., in Advances in Electrochemistry and Electrochemical Engineering, Vol. 2, p.15, Edited by Tobias, C.W., Interscience, New York (1962).
14. Ota, T., and Yoshikawa, S., unpublished data.
15. Carmona, F., Conet, R., and Delhaus, P., *J. Appl. Phys.* **5282** (1987).
16. Bhattacharya, S.K., and Chaklader, A.C.D., *Polym.-Plast. Technol. Eng.* **19**, 21 (1982).
17. Malliaris, A., and Turner, D.T., *J. Appl. Phys.* **42**, 614 (1971).
18. Kusy, R.P., *J. Appl. Phys.* **48**, 5301 (1978).

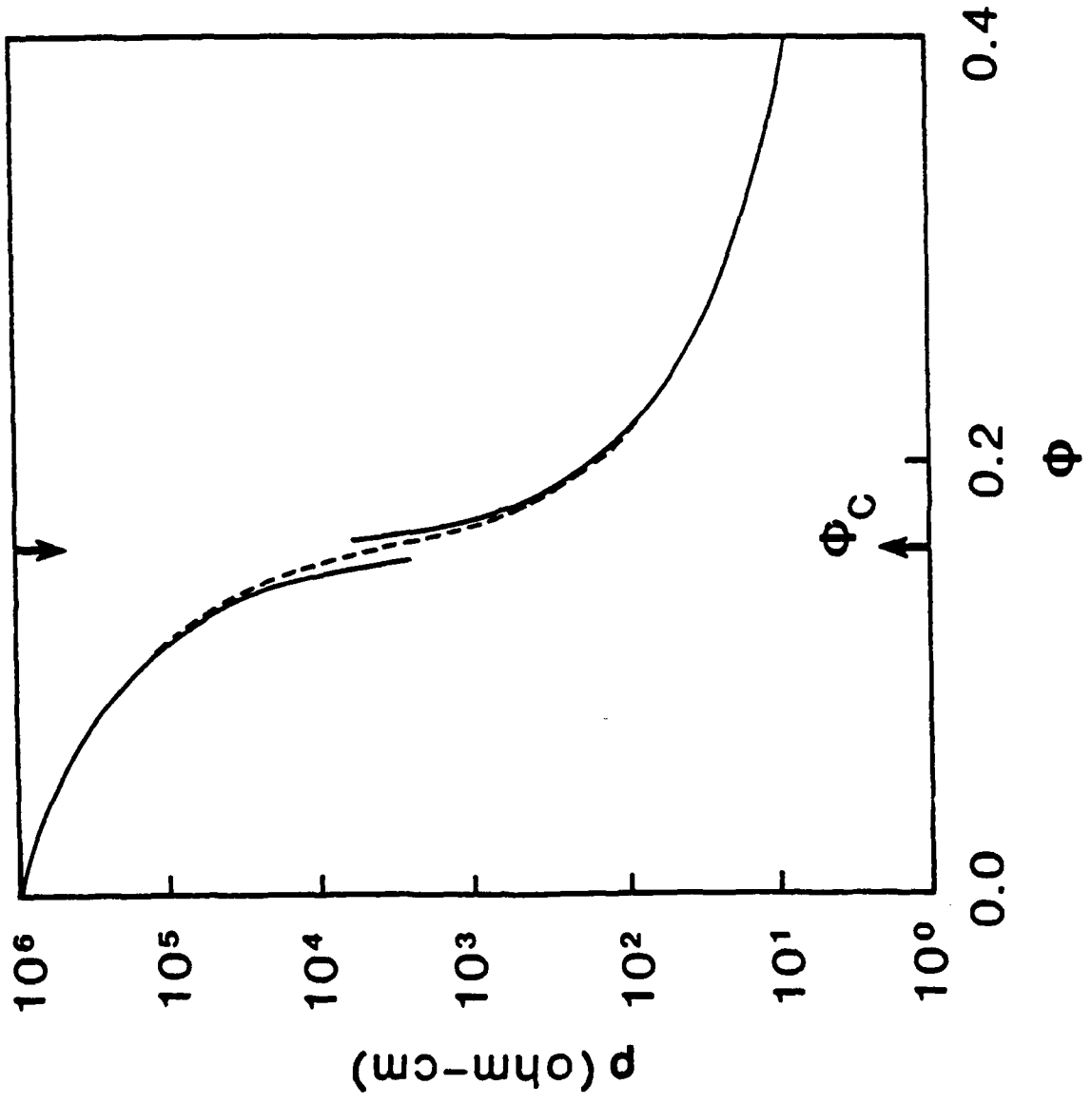
19. Gurland, J., *Trans. Met. Soc. AIME* **236**, 642 (1966).
20. Michels, M.A.J., Brokken-Zÿn, J.C.M., Groenwond, W.M., and Knoester, A., *Physica* **A157**, 529 (1989).
21. Blaszkiewicz, M., McLachlan, D.S., and Newnham, R.E., submitted to press.
22. McLachlan, D.S., Blaszkiewicz, M., Newnham, R.E., accepted *J. Am. Ceram. Soc.*

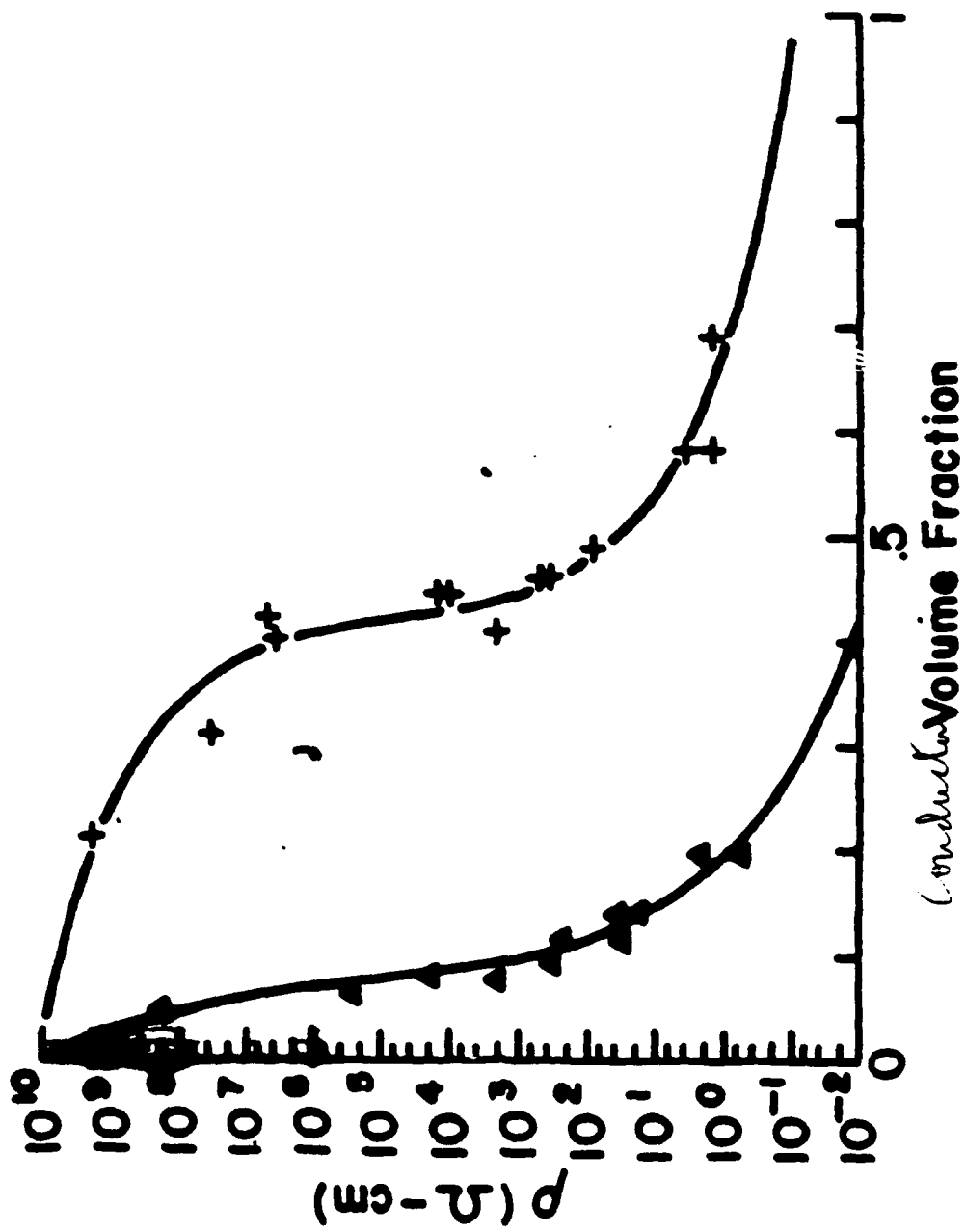
## Captions

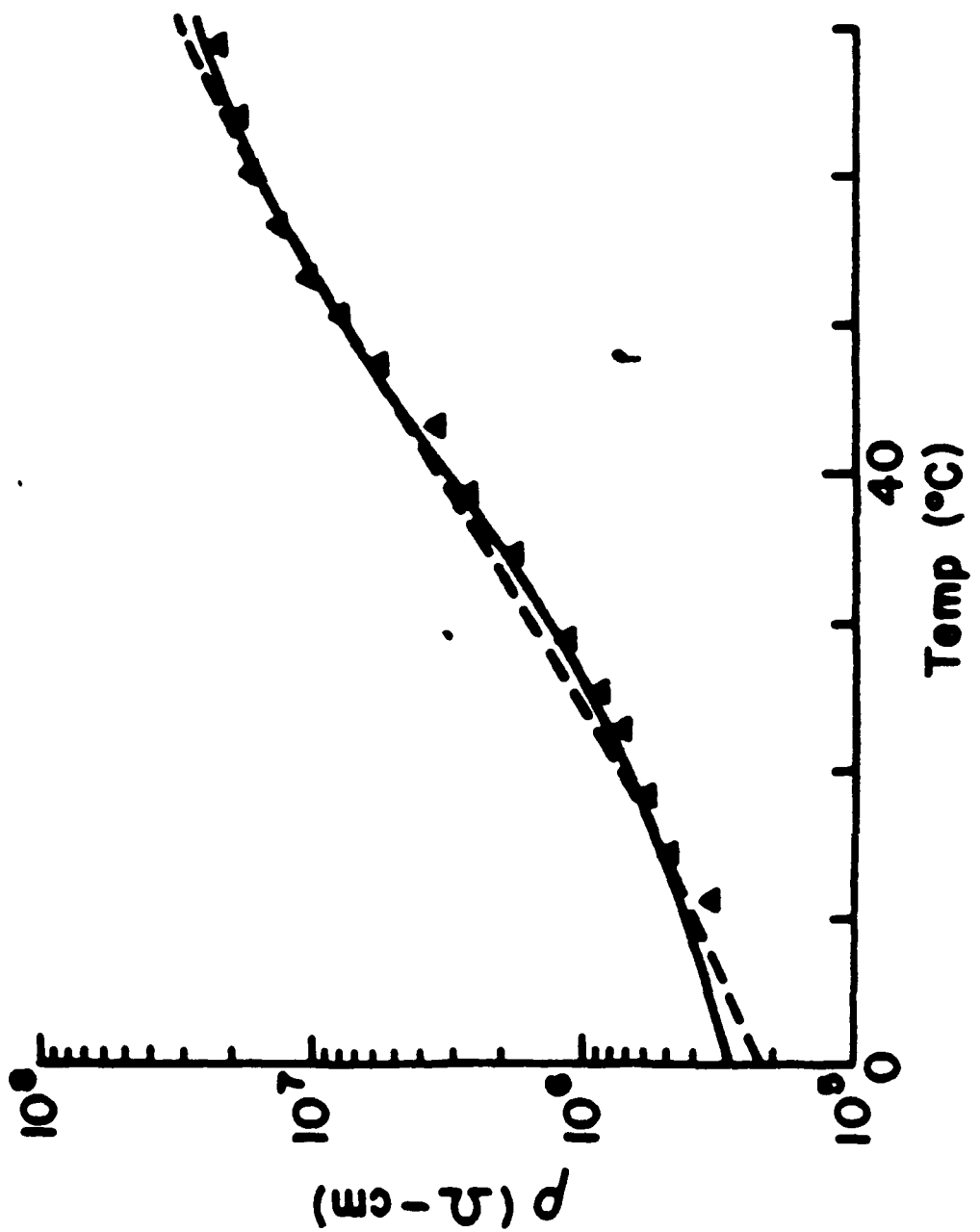
Figure 1. In this figure Eq. 1, Eq. 2, and Eq. 3 are plotted for  $\sigma_l = 10^{-6}$  ( $\rho_h = 10^6$ ),  $\sigma_h = 1$  ( $\rho_l = 1$ ),  $\phi_c = 0.16$  ( $f_c = 0.84$ ), and  $t = 1.7$  as a function of  $\phi$  or  $1-f$ .

Figure 2. The resistivity versus volume fraction of filler material for carbon black-eccogel ( $\Delta$ ) and for graphite-eccogel (+) composites. The solid lines through the data points were generated using the GEM equation. The parameters used are given in the text.

Figure 3. The resistivity versus temperature for a 47 volume percent graphite-eccogel composite. The solid line was generated using the GEM equation and a five parameter fit and the dashed line was generated using the GEM equation and a three parameter fit to the data. The model and the parameters are given in the text.







**APPENDIX 29**

# Resistivities of conductive composites

G. R. Fuschau,<sup>a)</sup> S. Yoshikawa, and R. E. Newnham

Materials Research Laboratory, Pennsylvania State University, University Park, Pennsylvania 16802

(Received 10 February 1992; accepted for publication 22 April 1992)

A steady-state model for the resistivity of composites is presented, based on the idea that the resistance through a composite is the result of a series of a large number of resistors combined in series and parallel. There are three separate contributions to the resistance: constriction resistance at the contacts, tunneling resistance at the contacts, and the intrinsic filler resistance through each particle, with tunneling resistance generally dominating the magnitude of the overall resistance. The model predicts resistivity increases with increasing filler hardness and/or elastic modulus and insulating film thickness, while resistivity decreases with increasing particle size and intrinsic stress. The room-temperature dc resistivity behavior of conductor-filled silicone rubber composites was investigated to verify the model. Comparison of the model to this experimental data showed that good agreement could be obtained for filler materials in which the tarnish layer was a known quantity for a given powder; for other cases, the experimental values were higher than predicted.

## I. INTRODUCTION

Composites consisting of highly conductive filler powder dispersed in a flexible, insulating polymer matrix are commonly used in electronic applications for die attach,<sup>1</sup> solderless connectors,<sup>2</sup> thermistors,<sup>3,4</sup> and pressure-sensing elements.<sup>5</sup> Other uses of such composites include electromagnetic shielding and antistatic devices<sup>6</sup> as well as chemical sensors.<sup>7</sup>

The properties of composite systems are understood in terms of percolation phenomena; when a sufficient amount of conductive filler is loaded into an insulating polymer matrix, the composite transforms from an insulator to a conductor, the result of continuous linkages of filler particles. This is shown graphically in Fig. 1; as the volume fraction of filler is increased, the probability of continuity increases until the critical volume fraction, beyond which the electrical conductivity is high, comparable to the filler material. Effective-media theories attempt to quantify the resistance of these systems, based on the idea that the contribution of each phase to the conductivity depends not only on the relative amount of that phase present but also its degree of self-connectivity. A number of effective-media equations have been derived to model the shape of this curve,<sup>8-11</sup> while these equations can successfully mimic this shape, they are not useful for describing the magnitude of the electrical resistivity of the composite.

Once percolation is "complete," i.e., a significant number of percolated linkages has formed, the differences in conductivity between samples with the same degree of self-connectivity and the same volume fraction of filler but with different filler materials can be unpredictably large. All particle-filled composites have resistivities several orders of magnitude higher than the resistivities of the pure filler materials. This has been well documented for a variety of conductive fillers, as shown in Table I. In many cases, it is

difficult to obtain composites with resistivities within five orders of magnitude of the pure material.

In a previous paper,<sup>14</sup> the authors presented a model showing the dependence of composite resistivity on filler particle size to help quantify the differences. In this investigation, this model has been expanded to include the fundamentals of contact resistance; a more accurate model was derived from these principles.

## II. DERIVATION OF THE MODEL

### A. Fundamentals of contact resistance

When speaking of effective-media approximations in electrically conductive composites, a continuous linkage of conductive particles is often thought of as a single conductive filament; however, this is not accurate. Rather, each percolated linkage should be thought of as a series of resistors, with each particle and each particle-particle contact contributing to the total resistance in the filament. There are two important contributions to the particle-particle contact resistance: constriction resistance and tunneling resistance.

#### 1. Constriction resistance

When two conductive spheres meet, there is a resistance associated with the constriction of electron flow through the small area. This resistance, known as the constriction resistance  $R_{cr}$ , can be derived from the principles of ohmic conduction and electric fields, and has been shown<sup>15</sup> to be

$$R_{cr} = \rho_i / d, \quad (1)$$

where  $\rho_i$  is the intrinsic filler resistivity and  $d$  is the diameter of the contact spot. Intuitively, this is a surprising result in that  $R_{cr}$  is inversely proportional to the diameter, rather than the area, of the contact spot. For a composite with a filler of a given particle size  $D$ , the important relationship is the ratio of  $D/d$ ; when this ratio  $> \sim 10$ , Eq.

<sup>a)</sup>Permanent address: ARCO Oil & Gas, 2300 W. Plano Pkwy, Plano, TX 75075.

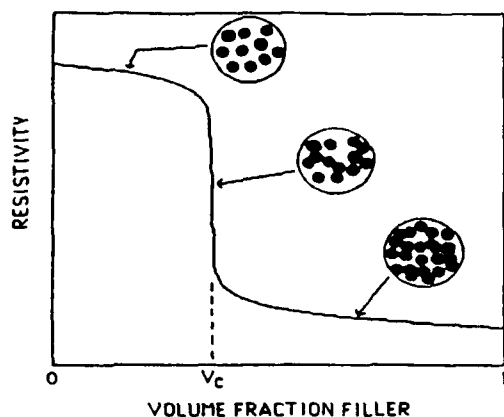


FIG. 1. Percolation theory, as applied to conductive composites. The formation of the first complete particle linkage results in a sharp drop in resistivity at  $V_c$ .

(1) begins to diverge so that very high resistances result even though the spheres may still be in physical contact.

## 2. Tunneling resistance

The other important limitation to the conductivity of two spheres is the resistance associated with any insulating film which may be completely coating each filler particle. The origin of this film may vary somewhat depending on the system. Tarnish films on metals are known to form almost instantly upon exposure of a pristine metal surface to normal atmospheric conditions.

Such oxide films, over a reasonably short period of time, may be somewhat protective so that a limiting, transient film thickness may be assumed for a given metal. For metals that obey the logarithmic law, the oxide is very protective and the transient film thicknesses (and their contribution to the tunneling resistivity) are easier to predict. In reality, the initial oxide formation is a very complicated issue, depending on the partial pressure of oxygen, the crystallographic orientation of the metal surface, the stoichiometry of the oxide formed (i.e.,  $\text{Cu}_2\text{O}$  vs  $\text{CuO}$ ), the relative humidity, etc.<sup>16</sup>

TABLE I. Resistivities of conductor-filled polymers by other investigators.

Filler	Polymer	Filler resistivity ( $\text{m}\Omega\text{ cm}$ ) <sup>a</sup>	Composite resistivity ( $\text{m}\Omega\text{ cm}$ ) <sup>b</sup>	Vol % loading
C black	Polyethylene	1.0	2000	30 <sup>c</sup>
$\text{V}_2\text{O}_5$	Polyethylene	0.1–10.0	100 000	50 <sup>d</sup>
$\text{MoSi}_2$	Polyethylene	0.021	500 000	50 <sup>e</sup>
$\text{TiB}_2$	Polyethylene	0.028	60 000	40 <sup>e</sup>
Fe	Styrene/Acrylonitrile	0.010	1 000 000	50 <sup>f</sup>
Al	Polypropylene	0.003	20 000	25 <sup>f</sup>
Cu	Polyvinyl chloride	0.002	600	20 <sup>f</sup>
Ag	Epoxy resin	0.002	1.0	50 <sup>h</sup>

<sup>a</sup>Theoretical.

<sup>c</sup>See Ref. 12

<sup>b</sup>Experimental.

<sup>d</sup>See Ref. 6.

<sup>e</sup>See Ref. 4.

<sup>f</sup>See Ref. 13.

<sup>h</sup>See Ref. 3.

<sup>g</sup>See Ref. 1

For processed powders, residual organic films may remain on the powder surface after milling, sometimes purposely deposited for dispersion or dedusting reasons. Further processing in organic solutions may or may not remove these films. In a conductor-filled polymer composite, the polymer itself may completely cover the powder surface, resulting in a thin film of polymer separating the powders.

All three of these films may be present in varying thicknesses, providing an insulating layer between two spheres. According to classical mechanics (and the Bruggeman asymmetric effective media<sup>9</sup> or Hashin coated-spheres models<sup>10</sup>), this would result in a high series resistance, but this is not the case. For thin films on the order of 100 Å or less, quantum-mechanical tunneling can occur, resulting in lower resistivities.

The physics of quantum-mechanical tunneling show that the relative probability that an electron will "tunnel through," rather than surmount, a potential barrier is proportional to the work function of the conductor, the thickness of the film, and the relative dielectric permittivity of the film. The surprising result is that the resistivity of the film is not a factor in tunneling, so that organics, polymers, and oxides, most with similar work functions and permittivities, will have similar tunneling resistivities for similar film thicknesses.

The dependence of tunneling resistivity on the insulating film thickness has been derived mathematically. Dietrich<sup>17</sup> pioneered the work on this problem, and presented a general tunneling curve (based on  $\text{TiO}_2$  films on Ti), empirically derived but thought to be approximately applicable to all materials (see Fig. 2).

Thus a tunneling resistivity  $\rho_t$  may be applied to the contact if the insulating film thickness is known. The tunneling resistance associated with a contact  $R_t$  is, unlike constriction resistance, inversely proportional to the contact spot area  $a$ , so

$$R_t = \rho_t / a. \quad (2)$$

The resistance of a contact therefore is the sum of these two separate effects,

$$R_c = \rho_c / d + \rho_t / a. \quad (3)$$

In general, the tunneling resistance term dominates  $R_c$  except in the cases of noble metals or carefully cleaned and protected metal contact surfaces.

## 3. Contact spots

There is still an unknown quantity in Eq. (3), that being the contact spot area [or diameter, but obviously  $d = (4a/\pi)^{1/2}$  for spherical particles with circular contact spots]. This area must be a function of the applied pressure between particles  $F$  and the deformation that occurs as a result of this applied pressure.

There are two types of deformation that can occur when two particles come into contact, elastic (recoverable) and plastic (permanent) deformation. Wagar<sup>18</sup> showed that in the case of electrical contacts, the strains necessary to reduce the constriction resistance below the critical

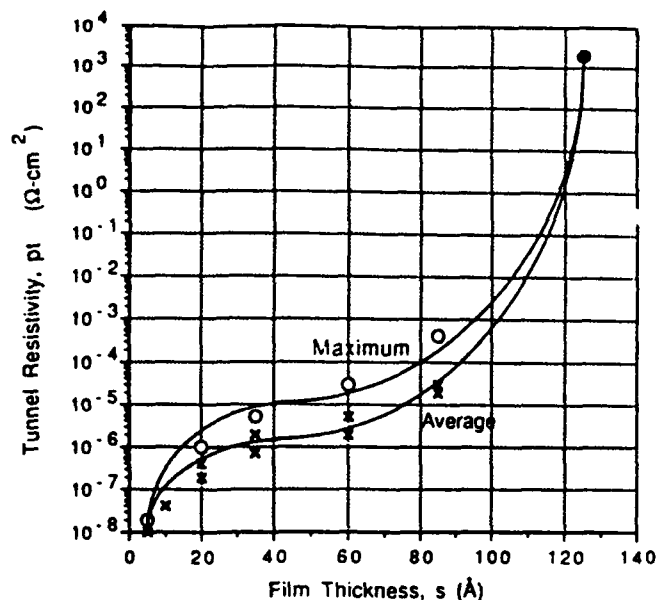


FIG. 2. Tunnel resistivity for thin films of TiO<sub>2</sub> on Ti as a function of film thickness (Ref. 17).

value of  $\sim 10$  are larger than the elastic yield strain; that is, if "good" electrical contact is made, both elastic and plastic deformation occur.

The magnitude of the deformation for a given force is controlled by a material parameter, the contact hardness  $H$ , which is either measured by observing areas of indentation under applied load or approximated by taking  $H = 3\sigma_y$ , where  $\sigma_y$  = the 0.2% offset yield stress. Though "hardness" is generally defined as a measure of the tendency of a material to bulk or volume flow, contact hardness is not always easy to define. When thick oxide films grow on metals, for example, the measured hardness will vary depending on the method used for measurement; microhardness techniques would obviously be more sensitive to thin oxide film properties than ordinary stress/strain curve approximations. In addition, work hardening of metals results in harder, stiffer materials due to an increase in dislocation densities, so the history of a specific metal powder is important.

Despite these inconsistencies, the area of contact between two spheres can be fairly accurately determined by one of the following:

$$a = F/H \quad (\text{plastic case}), \quad (4a)$$

$$a = 2.43(FD/E)^{2/3} \quad (\text{elastic case}), \quad (4b)$$

where  $D$  is the sphere diameter and  $E$  is the elastic modulus. Since in most cases the deformation is a combination of plastic and elastic regions, the empirical term  $\xi$ , called the elasticity factor, is introduced. For the combination of elastic and plastic deformation the contact area becomes

$$a = F/\xi H. \quad (5)$$

$\xi$  ranges from a value of 0.2 for purely elastic deformation to 1.0 for purely plastic deformation. For most systems, a value of  $\xi = 0.7$  has been found to be quite reliable.

Substituting Eq. (5) into Eq. (3) gives

$$R_c (\text{plastic}) = 0.89\rho_i(\xi H/F)^{1/2} + \rho_i \xi H/F. \quad (6a)$$

while substituting Eq. (4b) into Eq. (3) for elastic deformation gives

$$R_c (\text{elastic}) = 0.57\rho_i(E/FD)^{1/3} + 0.26\rho_i(E/FD)^{2/3}. \quad (6b)$$

This describes the resistance at an electrical contact in terms of some known material parameters and the (variable) applied force.

### III. APPLYING CONTACT RESISTANCE TO COMPOSITES

In composite conductors the total resistance is a function of both the resistance through each particle and the particle-particle contact resistance. The number of contacts between electrodes thus becomes a factor in this relationship, as well as the number of conduction paths. If contact resistance at the electrodes is also considered, the resistance may be described by the following relation, developed by Yasuda and Nagata:<sup>19</sup>

$$R_c = 2R_e + \frac{(M-1)R_p + MR_i}{N}, \quad (7)$$

where  $R_c$  is the composite resistance,  $R_e$  the lead resistance to electrodes,  $R_p$  the particle-particle contact resistance,  $R_i$  the resistance across one particle,  $M$  the number of particles forming one conduction path, and  $N$  the number of conduction paths. If a four-point-probe resistance measurement is used,  $R_e$  is eliminated from Eq. (7).

For highly conductive composites, the volume loading is high enough to avoid percolation threshold effects, and in this case the maximum number of particles is involved in the electrical conductivity. Thus, this type of composite may properly be thought of as a true conductive skeleton of a certain packing geometry.

Consider the simplest form of skeleton geometry, simple cubic packing. For a composite of length  $L$ , width  $w$ , and thickness  $t$  with electrodes at both ends (see Fig. 3) and monosized spheres arranged in simple cubic packing, the number of conductive chains between the electrodes is simply the cross-section area of the sample divided by the cross-section area of one chain. If the particle diameter is given by  $d$ , then the cross-section area of one chain and its surrounding insulation is  $d^2$ , and thus

$$N = wt/d^2. \quad (8)$$

Similarly, the number of particles in one chain is given by the distance between electrodes divided by the particle diameter, or

$$M = L/d. \quad (9)$$

These simplifying assumptions do not adequately describe the arrangement of conductive chains in a real composite. In an actual sample, the conductive pathways may meander from the straight, parallel arrangement assumed above. For comparison purposes, however, the assumptions are necessary.

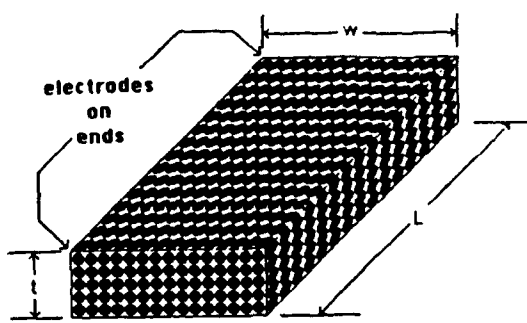


FIG. 3. Composite sample with simple cubic packing.

For samples in which the  $L/d$  ratio is large, it is convenient to make the simplifying assumption

$$M - 1 \approx M. \quad (10)$$

The intrinsic resistance of an individual particle may be estimated assuming an equivalent cross-sectional area of a sphere, that is, the cross-sectional area of a cylinder whose volume is equal to the sphere. By geometry, this cross-sectional area can be shown to be  $0.524d^2$ . Given that the resistance across the particle is related to the intrinsic resistivity  $\rho_i$ , by  $R_i = \rho_i/(wt/L)$ , with  $wt = 0.524d^2$  and  $L=d$ , this leads to the relation

$$R_i = \rho_i(d/0.524d^2) = \rho_i/0.524d. \quad (11)$$

The validity of the equivalent cross-sectional area assumption may be questionable but, as will be shown, it is of little significance in the model.

Substituting Eqs. (8), (9), (10), and (11) into Eq. (7) gives

$$R_c = (Ld/wt)R_p + (L/wt)\rho_i/0.524. \quad (12)$$

From Eq. (6a),  $R_p$  may be assumed to be equivalent to the general case for contact resistance of plastically deformed spheres,

$$R_p \text{ (plastic)} = 0.89\rho_i(\xi H/F)^{1/2} + \rho_i \xi H/F, \quad (13a)$$

where  $\xi$  is the elasticity factor ( $0.2 < \xi < 1.0$ ),  $H$  is the contact hardness, and  $F$  is the applied contact force.

The strains associated with electrical contact in a composite may be purely elastic in nature; certainly this is the case for ceramic fillers that undergo little or no plastic deformation. In this case Eq. (6b) applies,

$$R_p \text{ (elastic)} = 0.57\rho_i \left(\frac{E}{FD}\right)^{1/3} + 0.26\rho_i \left(\frac{E}{Fd}\right)^{2/3}. \quad (13b)$$

Equations (13a) and (13b) describe the resistance of each particle-particle contact for the elastic/plastic and pure elastic cases, respectively. Applied to a composite that contains  $N$  contacts in its cross-sectional area,  $M$  contacts in series, and a contact force of  $F/N$ ,  $R_p$  can be expressed as  $R_p' [= (Ld/wt)R_p]$ , the total resistance due to all particle-particle contacts. Equations (13a) and (13b) then become

$$R_p' \text{ (plastic)} = 0.89\rho_i L(\xi H/Fwt)^{1/2} + \rho_i \xi HL/Fd, \quad (14a)$$

$$R_p' \text{ (elastic)} = 0.57\rho_i L(E/F)^{1/3} [1/(wt)^{2/3}] + 0.26\rho_i L [1/d(wt)^{1/3}] (E/F)^{2/3}. \quad (14b)$$

Substituting into Eq. (12) yields

$$R_c \text{ (plastic)} = 0.89\rho_i L(\xi H/Fwt)^{1/2} + \rho_i \xi HL/Fd + (L/wt)\rho_i/0.524, \quad (15a)$$

$$R_c \text{ (elastic)} = 0.57\rho_i L(E/F)^{1/3} [1/(wt)^{2/3}] + 0.26\rho_i L [1/d(wt)^{1/3}] (E/F)^{2/3} + (L/wt)\rho_i/0.524. \quad (15b)$$

This describes the resistance of a composite in terms of sample geometry, particle size, applied force, and the intrinsic properties of the conductive filler.

To express this in terms of the specific electrical resistivity of the composite  $\rho_c$ , multiplying both sides of Eqs. (15a) and (15b) by  $(wt/L)$  yields

$$\rho_c \text{ (plastic)} = 0.89\rho_i(\xi Hwt/F)^{1/2} + \rho_i \xi Hwt/Fd + \rho_i/0.524 \quad (16a)$$

$$\rho_c \text{ (elastic)} = 0.57\rho_i(Ewt/F)^{1/3} + (0.26\rho_i/d)(Ewt/F)^{2/3} + \rho_i/0.524. \quad (16b)$$

Equation (16a) may be more appropriate for metal and polymer fillers, while Eq. (16b) applies to ceramics.

The following assumptions are inherent in this model.

(i) The volume fraction occupied by the filler is 0.524 and is independent of particle size; this is not true for real systems, but it is true under the stated ideal conditions (perfect spheres with simple cubic packing). This is not the critical volume fraction for conduction as described by percolation theory, but is instead the volume fraction for the complete conductive skeleton. Rough estimates of percolation effects on resistivity based on the volume fraction for a particular sample  $V_f$  can be made by multiplying the calculated resistivities by  $0.524/\phi_p$ . This accounts for the decreased number of percolated pathways in the less heavily loaded yet highly conductive composites. The model is only meant to offer a qualitative look at the factors affecting resistance and a quantitative comparison of two different filler materials with regard to their intrinsic properties.

(ii) All particles are involved in conduction, i.e., no "cul de sacs" (nonpercolated chains) exist. Therefore, the model is only valid for samples that are thick enough to avoid the effects of cul de sacs (large ratio of  $t/d$ ). The conduction paths are straight chains, not meandering randomly through the composite.

(iii) The tunneling resistivity and contact force are the same for any two particles of the same material, independent of particle size; only the contact areas are different (i.e., all contacts within a composite are the same).

(iv) The electrical resistivity of the polymer and tunneling conduction through regions other than at the particle-particle interface do not significantly figure into the resistivity of the composite when there is percolation.

The sample dimensions  $wt$  appear in both Eqs. (16a) and (16b), indicating that resistivity is a function of sample geometry. This, however, is purely a mathematical consequence of the model; resistivity is a function of  $wt$  only in cases where a known constant contact force  $F$  is applied (e.g., a fixed weight placed on top of a loose powder). For composites, the geometry dependence of the resistivity can be eliminated by substituting an induced stress  $\sigma$ , into the model for resistivity.

There are several contributions to  $\sigma$ . First of all, when a filler that has a lower coefficient of thermal expansion than the polymer matrix is introduced into the matrix, tensile stress will be induced in the polymer when the composite is cooled. The thermally generated stress  $\sigma^*$  can be calculated directly for polymers that are below  $T_g$  or  $T_m$  and spherical fillers.<sup>20</sup> In the case of thermally cured composites or composites that are mixed in the molten state of the polymer,  $\sigma^*$  is a function of the difference in thermal-expansion coefficients and the reference temperature in the form.

$$\sigma^* = KE(\alpha_p - \alpha_f)(T_0 - T), \quad (17)$$

where  $K$  is a constant ( $\approx 1$ ),  $E$  is the composite modulus in an unstressed state, [many different approximations available—series model:  $E = V_f E_f + (1 - V_f) E_p$ ],  $\alpha_p$  is the thermal-expansion coefficient of the polymer,  $\alpha_f$  is the thermal-expansion coefficient of the filler,  $T_0$  is the temperature at which thermal stresses set in (usually  $T_g$  or  $T_m$ ), and  $T$  is the reference temperature.

For example, 25% silver filler ( $\alpha_f = 57 \times 10^{-6}/^\circ\text{C}$ ,  $E_f = 76 \times 10^9 \text{ N/m}^2$ ) in polystyrene ( $T_0 = T_g \sim 105^\circ\text{C}$ ,  $\alpha_p = 1.9 \times 10^{-4}/^\circ\text{C}$ ,  $E_p = 3.4 \times 10^9 \text{ N/m}^2$ ) produces a thermal stress of  $2.3 \times 10^8 \text{ N/m}^2$  at  $25^\circ\text{C}$ .

When  $T > T_g$ , which is the case with elastomers, the thermally induced stress is relaxed out of the composite with time. Nonetheless, stresses that were quickly relieved may be large enough to cause the initial deformation in the filler material. In addition, when sufficiently crosslinked, complete stress relaxation cannot occur even well above  $T_g$ ; this is why rubber bands maintain their elasticity over long periods of time.<sup>21</sup> For elastomers, therefore,  $\sigma^*$  depends on the cooling rate and the dynamic mechanical properties of the polymer; if the time to cooling is faster than the relaxation time of the polymer, an initial stress will occur.

Another source of internal stress is capillary action. When two particles have an intervening bridge of liquid between them, the particles will be pulled together with sufficient force so as to minimize the liquid-vapor surface area. The magnitude of the force depends on the curvature of the liquid surface, the surface energy, and the liquid volume. The greater the curvature and surface energies, and the smaller the liquid volume, the greater the capillary force.<sup>22</sup>

In addition to thermally generated stresses and stresses induced by capillary action, the stress induced by shrinkage crosslinking provides another contribution to  $\sigma$ . This

Because crosslinking decreases the free volume of a polymer, an increase in  $T_g$  can be seen for crosslinked systems, with the increase proportional to the crosslink density. Therefore, crosslinking also increases the thermally generated stress, as calculated by Eq. (17).

Substituting  $\sigma$ , for  $F/wt$  in the models leaves

$$\rho_{c(\text{plastic})} = 0.89\rho_i(\xi H/\sigma_i)^{1/2} + \rho_i \xi H/d\sigma_i + \rho_i/0.524, \quad (18a)$$

$$\rho_{c(\text{elastic})} = 0.57\rho_i(E/\sigma_i)^{1/3} + (0.26\rho_i/d)(E/\sigma_i)^{2/3} + \rho_i/0.524. \quad (18b)$$

In the case of only elastic deformation of the filler in an elastomer matrix, the force due to  $\sigma$ , must be greater than the elastic restoring force of the filler, or else only point contact is possible. Electron tunneling is still possible over a distribution of gap widths, but this is not accounted for in the model, as noted in the model assumptions given previously.

The implications of this model for producing composites are clear, and the number of controlling parameters is surprisingly low (although percolation considerations, not discussed here, present a separate set of variables which depend on several other factors<sup>8</sup>). The model predicts resistivity increases with increasing filler hardness and/or elastic modulus and insulating film thickness, while resistivity decreases with increasing particle size and intrinsic stress. Thus to produce the most highly conductive composite, it is necessary to choose relatively soft, large particle size fillers; conductor-coated polymeric fillers provide a good combination of softness without losing the intrinsic conductivity of the metal, while long, fibrous fillers result in fewer particle-particle contacts in series to reduce the overall contribution of the contact resistance. Small transient oxide or tarnish layers are especially critical, particularly for large-scale sample preparation in which the powders cannot be cleaned before processing. Finally, it is beneficial to use polymer matrices that undergo considerable shrinkage during processing, such as semicrystalline polymers which generally undergo a large, abrupt volume change at the crystalline melting point.

## B. Coated fillers

For situations in which a nonconductive filler material is coated with a conductor, each particle becomes a more complex version of two individual resistors combined in parallel. Hashin<sup>10</sup> developed the relationship to predict the resistivity  $\rho_{cs}$  of conductor-coated spheres. This coated-spheres model (which has also been used as an effective-media approximation for composites as a whole) is as follows:

$$\rho_{cs} = \rho_{\text{coat}} \left( 1 + \frac{V_{\text{core}}}{[(\rho_{\text{coat}}/\rho_{\text{core}}) - 1]^{-1} + (1 - V_{\text{core}})/3} \right)^{-1}, \quad (19)$$

where  $V_{\text{core}}$  is the volume fraction of the sphere occupied by core,  $\rho_{\text{core}}$  is the resistivity of the coating material, and

TABLE II. Intrinsic properties of filler materials and substrates used in model for resistivity.

Filler	Manufacturer	$\rho_i$ ( $\mu\Omega$ cm)	Vickers hardness (GN/m <sup>2</sup> )	Estimated insulator thickness (Å)	$\rho_i^a$ ( $\mu\Omega$ cm <sup>2</sup> )
Ag <sup>b</sup>	Metz	1.6	0.26	10 <sup>c</sup>	0.3
Ni <sup>b</sup>	Novamet	6.9	0.69	25 <sup>c</sup>	3.0
Al <sup>b</sup>	Alfa	2.6	0.18	50 <sup>d</sup>	3000
Cu <sup>b</sup>	Aldrich	1.7	0.39	50 <sup>d</sup>	3000
Substrates for coated fillers:					
TiO <sub>2</sub>	Mitsubishi	...	9.00 <sup>e</sup>	...	...
Phenolic resin	Mitsubishi	...	0.05 <sup>f</sup>	...	...

<sup>a</sup>All values taken from Fig. 1, based on two times the given film thickness.

<sup>b</sup>All values (except as noted) from Ref. 18.

<sup>c</sup>Values from product literature.

<sup>d</sup>Values from Ref. 16.

<sup>e</sup>Values from Ref. 24.

<sup>f</sup>Values from Ref. 25.

$\rho_{\text{core}}$  is the resistivity of the core material. Since information regarding the coating thickness on a powder is often more easily attainable than the volume fraction, it may be more convenient to express Eq. (15) in terms of the coating thickness;  $V_{\text{coat}} (= 1 - V_{\text{core}})$  is related to the coating thickness  $\tau$  by the following:

$$V_{\text{coat}} = (d^3 - 3d^2\tau + d\tau^2 + \tau^3) / d^3. \quad (20)$$

Thus, for coated fillers, we substitute Eqs. (19) and (20) for  $R_i$  in the model. Since the coatings are normally quite thin relative to the particle size, the physical properties ( $E$ ,  $H$ , and  $\xi$ ) of the substrate material, rather than the coating material, should be used in the model, while the electrical properties ( $\rho_i$  and  $\rho_j$ ) of the coating material should be used.

#### IV. EXPERIMENTAL VERIFICATION OF THE MODEL

##### A. Experimental procedure

Several different filler materials were used in this investigation to determine the accuracy of the model for resistivity. These materials, along with the physical properties used in the calculations, are listed in Table II. Relatively monosize distributions of all powders were used; all powders were roughly spherical. Several different volume fraction loadings were made for each powder; when the resistance of a sample no longer decreased appreciably with additional filler loading, this resistance was taken to be the resistance of the sample. Continued loading of filler beyond this bottom end volume fraction results in highly porous samples with poor mechanical properties but no improvement in resistivity. Silicone rubber (G.E. 845 silicone elastomer) was the polymer matrix material used in this investigation.

After weighing all samples to the proper volume loading using a mixture of about 16% silicone in trichloroethylene (TCE) solvent the batches were mixed for 1 min with a polypropylene propeller blade at 800 rpm. The slip was cast onto 6 x 8 in.<sup>2</sup> borosilicate glass sheets into 250–300  $\mu\text{m}$  sheets and cut into 2 x 5 cm<sup>2</sup> rectangular samples.

The dc electrical resistance of three to six samples of each formulation and thickness was measured across each sample by a four-probe measurement technique using the gold-plated leads and a fluke digital multimeter. The resistivity was calculated using the measured sample thickness while the length and width of the samples were held constant at 5.0 and 2.0 cm, respectively. Resistivities for volume fractions other than 0.524 were predicted by multiplying the predicted resistivity by 0.524/(volume fraction), thus compensating for the lesser number of conductive pathways at volume fractions less than 0.524. For all cases, a nominal value of  $\sigma_i = 5.0 \times 10^8$  N/m<sup>2</sup> was assumed; this was approximated from the data for previous samples. This value of  $\sigma_i$  was not verifiable but is greater than the elastic yield strength for the Ag and Ni fillers ( $\sigma_y = 5-7 \times 10^7$  N/m<sup>2</sup> for Ag and Ni) so the assumption of plastic deformation of the filler in these composites was valid.

##### B. Results and discussion: Comparison to model

Table III shows how the calculated resistivities for some of the filler materials compares to the predicted resistivities at the given volume fraction, using the material parameters from Table II.

Good agreement was seen for Ag- and Ni-filled composites, but Cu and Al were off by several orders of magnitude. This was probably due to the presence of a much thicker oxide layer on the Cu and Al powders than the value reported in Table II; the values of transient oxide thickness for a given metal are highly dependent on the oxidizing conditions. Powders that have spent years on the shelf in humid and/or corrosive atmospheres would be expected to have thick oxide layers. Quantifying this oxide for an individual powder is not a trivial matter, and requires very sophisticated and expensive analytical equipment, such as electron spectroscopy for chemical analysis or secondary-ion mass spectroscopy, along with a skilled operator.

The Ag-coated fillers showed reasonably good agreement with the model as well, indicating that the assump-

based on Eq. (16a) and the material parameters given in Table II ( $\sigma_c = 5 \times 10^4 \text{ N/m}^2$ ).

Filler	Particle size		$\rho_{\text{predicted}}$ (m $\Omega$ cm)	$\rho_{\text{exp}}$ (m $\Omega$ cm)	Standard deviation (m $\Omega$ cm)
	( $\mu\text{m}$ )	Vol %			
Ag	0.5	10	19.0	31.0	$\pm 7.50$
	0.5	15	13.0	12.0	$\pm 3.60$
	1.0	15	6.40	7.10	$\pm 0.13$
	1.0	20	4.80	2.90	$\pm 1.90$
	5.0	20	0.96	0.49	$\pm 0.015$
	5.0	25	0.77	0.21	$\pm 0.077$
	9.0	30	0.36	0.67	$\pm 0.036$
	9.0	35	0.31	0.40	$\pm 0.048$
Ni	1.0	20	180	190	$\pm 41.0$
	1.0	25	140	80	$\pm 9.9$
Al	5.0	25	110 000	5 100 000	$\pm 140 000$
	5.0	30	88 000	690 000	$\pm 32 000$
Cu	1.0	25	110 000	$1.5 \times 10^{11}$	$\pm 6.1 \times 10^{10}$
	1.0	30	95 000	$6.7 \times 10^{10}$	$\pm 4.9 \times 10^{10}$
Ag:Ni	5.0	25	2.10	19.0	$\pm 0.66$
Ag:Ni	5.0	30	1.70	3.70	$\pm 0.50$
Ag:PR	15	40	0.23	3.80	$\pm 0.072$
Ag:PR	15	45	0.20	1.70	$\pm 0.084$
Ag:PR	15	50	0.19	0.98	$\pm 0.026$
Ag:TiO <sub>2</sub>	1.0	20	170.0	61.0	$\pm 19.0$
Ag:TiO <sub>2</sub>	1.0	25	130.0	16.0	$\pm 1.7$

tion that the mechanical properties of the substrate material and the electrical properties of the coating material controlled the composite resistivity was accurate.

## V. CONCLUSIONS

The steady-state model for the resistivity minima of composites is based on the notion that the composite is the result of a series of a large number of resistors combined in series and parallel. There are three separate contributions to the resistance: constriction resistance at the contacts, tunneling resistance at the contacts, and the intrinsic filler resistance through each particle. Tunneling resistance generally dominates the magnitude of the overall resistance; the intrinsic filler resistance becomes significant for conductor-coated insulating filler.

The model-predicted resistivity increases with increasing filler hardness and/or elastic modulus and insulating film thickness, while resistivity decreases with increasing particle size and intrinsic stress. Ag and Ag-coated fillers provided the best combination of low tunneling resistivity and low filler hardness. For the silicone elastomer used, the

exact origin of the contact force was unknown but believed to have been provided by a combination of intrinsic stress due to thermal-expansion differences in the matrix, capillary forces between particles, and crosslinking shrinkage. Comparison of the model to experimental data showed that good agreement could be obtained for filler materials in which the tarnish layer was a known quantity for a given powder; for other cases, the experimental values were higher than predicted.

## ACKNOWLEDGMENTS

The authors would like to thank the Ben Franklin Partnership and Elastomeric Technologies for their support of this research.

- <sup>1</sup>R. L. Opila and J. D. Sinclair, *Ann. Proc. Reliab. Phys. Symp.* 23, 164 (1985).
- <sup>2</sup>G. E. Pike, Sandia Laboratory Technical Report 81-0263, 1981.
- <sup>3</sup>K. A. Hu, D. Moffatt, J. Runt, A. Safari, and R. E. Newnham, *J. Am. Ceram. Soc.* 70, 583 (1987).
- <sup>4</sup>L. L. Rohlfling, R. E. Newnham, S. M. Pilgrim, and J. Runt, *J. Wave Mater. Int.* 3, 273 (1988).
- <sup>5</sup>S. Yoshikawa, T. Ota, and R. E. Newnham, *J. Am. Ceram. Soc.* 73, 263 (1990).
- <sup>6</sup>S. K. Bhattacharya, *Metal-Filled Polymers* (Marcel-Dekker, New York, 1986).
- <sup>7</sup>G. R. Ruschau, R. E. Newnham, J. Runt, and B. E. Smith, *Sens. Act.* 20, 269 (1989).
- <sup>8</sup>S. Kirkpatrick, *Rev. Mod. Phys.* 45, 574 (1973).
- <sup>9</sup>R. Landauer, in *Electrical Transport and Optical Properties of Inhomogeneous Media*, edited by J. C. Garland and D. B. Tanner (American Institute of Physics, New York, 1978).
- <sup>10</sup>Z. Hashin, *J. Comp. Mater.* 2, 284 (1968).
- <sup>11</sup>D. S. McLachlan, M. Blaskiewicz, and R. E. Newnham, *J. Am. Ceram. Soc.* 73, 2187 (1990).
- <sup>12</sup>T. R. ShROUT, D. Moffatt, and W. Huebner, *J. Mater. Sci.* 26, 145 (1991).
- <sup>13</sup>S. K. Bhattacharya, A. S. Basu, and K. D. Sadhan, *J. Appl. Poly. Sci.* 25, 111 (1980).
- <sup>14</sup>G. R. Ruschau, S. Yoshikawa, and R. E. Newnham, *Intl. J. Hybrid Microelectron.* 13, 100 (1990).
- <sup>15</sup>R. Holm, *Electric Contacts* (Springer, Berlin, 1967).
- <sup>16</sup>U. R. Evans, *The Corrosion and Oxidation of Metals: First Supplementary Volume* (St. Martin's, New York, 1968).
- <sup>17</sup>I. Dietrich, *Z. Phys.* 132, 231 (1952).
- <sup>18</sup>H. Wagar, *Physical Design of Electronic Systems* (Prentice Hall, Englewood Cliffs, NJ, 1971), Vol. 3.
- <sup>19</sup>N. Yasuda and M. Nagata, in *Proceedings of the First International Hybrid Microelectronics Symposium, Japanese Branch*, edited by T. Soto, 1985, p. 90.
- <sup>20</sup>L. E. Nielsen and T. B. Lewis, *J. Poly. Sci. A 2*, 1705 (1969).
- <sup>21</sup>L. E. Nielsen, *Mechanical Properties of Polymers and Composites* (Marcel-Dekker, New York, 1974).
- <sup>22</sup>R. M. German, *Particle Packing Characteristics* (Metal Powders Industries Federation, Princeton, NJ, 1989).
- <sup>23</sup>B. Miller, *J. Appl. Poly. Sci.* 10, 217 (1966).
- <sup>24</sup>W. J. Lackey, D. P. Stinton, G. A. Cerny, A. C. Schaffhauser, and L. L. Fehrenbacher, *Adv. Ceram. Mater.* 2, 24 (1987).
- <sup>25</sup>R. A. Flinn and P. K. Trojan, *Engineering Materials and Their Applications* (Houghton Mifflin, Boston, 1981).

**APPENDIX 30**

# PTC EFFECTS IN CONDUCTOR-FILLED AMORPHOUS POLYMER COMPOSITES

D. M. MOFFATT, J. RUNT, W. HUEBNER,  
S. YOSHIKAWA, and R. NEWNHAM

*Materials Research Laboratory  
The Pennsylvania State University  
University Park, Pennsylvania 16802*

---

## 3.1. INTRODUCTION

In general, thermistors can exhibit two primary resistance effects (see Fig. 3.1): the so-called NTC (negative temperature coefficient) and PTC (positive temperature coefficient) effects, for which an increase in temperature leads to a decrease or increase in resistivity, respectively. In composites, these transitions can arise from an individual component, such as the semiconductor-metal transition exhibited by  $V_2O_5$  or  $VO_2$  metallic filler, or result from a "product property," such as that exhibited in composite thermistors. PTC thermistors have been traditionally prepared from  $BaTiO_3$ , doped such that the grains are semiconducting and the grain boundaries are insulating. The PTC effect occurs during heating through the Curie point [1]. At this temperature, the crystal structure changes from tetragonal to cubic, accompanied by a ferroelectric-paraelectric transition. In the ferroelectric state, the spontaneous polarization compensates for the insulating grain boundary, resulting in a "low" resistivity. Although  $BaTiO_3$  thermistors exhibit relatively large changes in resistivity with temperature (up to six orders), they have relatively high room temperature resistivities ( $< 100 \Omega \cdot cm$ ) and are expensive to produce [2].

During the past three decades composite materials have been used increasingly for resistance applications. Generally, composites for PTC appli-

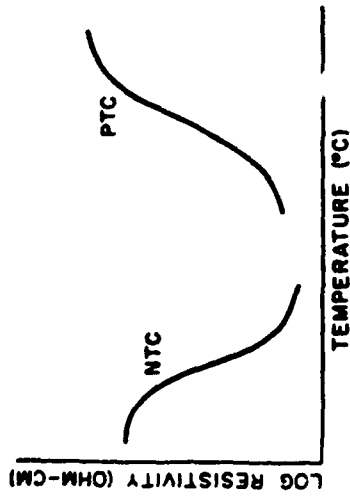


FIGURE 3.1  
General character of NTC (negative temperature coefficient) and PTC (positive temperature coefficient) transitions.

cations (such as circuit protection and self-regulating heaters) are based on a combination of a conductor in a semicrystalline polymer, with mixtures of carbon black and polyethylene as the prototypical example. In these composites there is a relatively sharp increase in resistivity near the melting temperature ( $T_m$ ) of the polymer, at which point a discontinuous change in the specific volume occurs. The PTC phenomena in such composite materials is believed to be a result of the separation of the conducting particles due to the thermal expansion of the polymer. Because the transition occurs at the melting point, one may control the PTC transition temperature by changing the polymer matrix. Composites prepared with crystalline polymer matrices can also exhibit dramatic NTC effects just above the melting point, due to the relaxation of the polymer structure. This effect may be eliminated by crosslinking the polymer or adding a third filler to stabilize the matrix [3-5].

There has been an extensive amount of research that has focused on the electrical properties of conductor-filled amorphous polymers as well. Carbon black has been utilized in a majority of these studies, but other fillers (such as copper, iron, or silver) have also been used. A wide variety of resistance trends have been noted in these composites, especially as a function of temperature. This is not surprising when one considers the many parameters that can influence the resistivity of conductor-amorphous polymer composites. With respect to the filler, important factors include its electrical conductivity, particle size, distribution, and morphology, thermal expansion coefficient, and surface properties (e.g., surface energy and oxidation state). Important polymer characteristics include the glass transition temperature ( $T_g$ ), electrical conductivity, and thermal expansion coefficient. The surface chemistry of the conductor and polymer can play a dramatic role with respect to not only the wetting behavior and resultant dispersion, but also the ultimate electrical properties (i.e., resistivity and the PTC effect).

### 3.2. PERCOLATION IN AMORPHOUS POLYMER COMPOSITES

Percolation theory deals with the number and properties of groups of neighboring entities and the existence of a sharp transition at which long-range connectivity in the system appears (or disappears). With respect to conductor-insulator mixtures, it describes the change in resistivity as a function of volume fraction conducting filler [6-9]; a typical percolation curve is shown in Fig. 3.2. There are three regions of importance. At low filler concentrations, the high resistivity is due to the insulating phase. As the volume fraction is increased, conducting paths start to form, resulting in a decrease in resistivity. This region is known as the percolation threshold. At higher filler concentrations, a saturation region is reached wherein the resistivity is relatively constant due to extensive interparticle contacts, and eventually approaches the value of the pure conductor.

The literature offers a detailed description of the percolation behavior of amorphous polymer composites and its relationship with the important filler and polymer properties. For example, the electrical conductivity, particle size, and morphology vary widely with the type of carbon black and these factors substantially impact the percolative properties [10-18]. Similar research involving these parameters in metal-filled polymers [19-21] has shown that for a given composition, the percolation threshold shifts to lower values the smaller the particle size of the filler. Furthermore, there is evidence that a broad particle size distribution leads to a higher percolation threshold [22].

The surface energy of the matrix and filler has a significant effect on the wetting behavior and, in turn, the degree of dispersion and electrical proper-

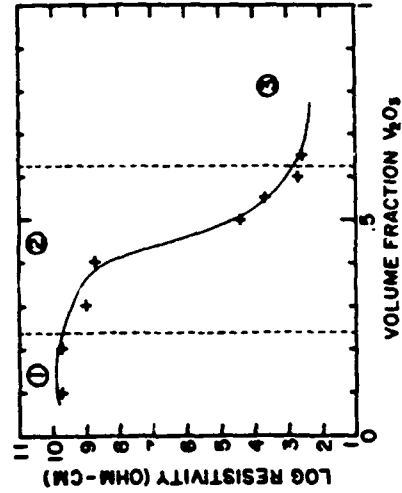


FIGURE 3.2  
Resistivity vs. volume fraction filler for  $V_2O_5$ -PMMA composites at 25°C and 1 kHz.

ties [22-28]. For a specific carbon black dispersed in a variety of polymers, it was found that the higher the surface energy of the polymer, the higher the critical concentration or threshold [19].

### 3.3. TEMPERATURE DEPENDENCE OF THE RESISTIVITY IN AMORPHOUS POLYMER COMPOSITES

The temperature dependence of the resistivity has been explored for a number of conductor-amorphous polymer composites. Generally, most conductor-filled amorphous polymers exhibit only a slight PTC transition, usually less than one order in magnitude, over a given temperature range. It is generally expected that there will not be a "high" PTC effect in composites with amorphous polymer matrices except over a very narrow concentration range near the percolation threshold [29]. In line with this expectation, there are many cases where no significant increase in resistivity with temperature is experimentally observed [14, 30, 31]. For example, in studies of particle agglomeration and particle contact, carbon black-ethylene-propylene rubber [32], carbon black-polystyrene (PS) [33], and carbon black-poly(butyl methacrylate) [33] composites showed no significant PTC effects. The resistive levels of resistivity attained by each of these systems are a function of the morphology of the filler and the ability of the polymer to wet the carbon black particles. Similarly, for silver-PS composites, no substantial increase in resistivity is seen over a temperature range that includes the  $T_f$  [34]. Other composites have exhibited a very modest (less than one order) increase in resistivity near  $T_f$ . This has been evidenced in carbon black-polycarbonate (PC) [35], carbon black-PS [14, 16, 23], carbon black-poly(methylmethacrylate) (PMMA) [36], and carbon black-polyvinylchloride [23] composites.

There are a few examples, however, where significant PTC effects have in fact been observed. In one case, amorphous polymer composites which exhibit a PTC effect are described in the U.S. Patent 4,534,889 [37]. According to the patent, all previously explored amorphous polymer composites failed to exhibit useful PTC resistance effects. They state that it is possible to prepare a PTC composite by dispersing conductive particles in an amorphous polymer then cross-linking the composite. It is proposed that the PTC transition in these composites will appear at the curing temperature of the polymer or enhance an already existent PTC near the curing temperature. They illustrate their findings with PTC effects in carbon black composites, but state that it is possible to see these effects in composites with metal powders and conductive metal salts and oxides. Other authors have also observed similar behavior in mixtures of carbon black and a styrene-butadiene rubber [38]. For composites filled with 0.50 and 0.60 phr (parts per hundred resin) carbon black, there was an increase in resistivity from two to four orders in magnitude at a temperature between 110 and 130°C. In

addition, a change in electrical conductivity of approximately 10 orders in magnitude has been observed in carbon black-polyester resin composites, but the location and nature of this transition were not described [39].

There are other instances in which a substantial PTC effect is observed in amorphous polymer composites documented prior to the patent. In Al- and Fe-filled poly(styrene-co-acrylonitrile) (SAN), a PTC of nearly three orders in magnitude occurs in a 40 vol % Fe composite, while in the Al-SAN systems, a PTC effect of eight orders is observed [40]. In both composites the PTC anomaly occurs near the  $T_g$  is SAN. In addition, composites of silver-coated copper particles in an epoxy resin exhibit a PTC transition of close to four orders in magnitude slightly below the polymer's  $T_g$  [41].

### 3.4. METAL OXIDE-POLYMER COMPOSITES

While a majority of the research concerning composites for resistance application focuses on the use of carbon black as the conducting filler, it is not necessarily the most practical material to characterize and control in terms of particle size, distribution, and morphology. In a move toward using conductors that are more easily managed, we have recently shown that composite materials containing ceramic fillers, transition metal oxides in particular, can exhibit unique electrical properties. These composites exhibit a PTC effect when combined with either a semicrystalline or amorphous polymer. A distinct advantage to using a ceramic material is that it is possible to control the parameters that dictate the percolation and PTC behavior. By altering the particle size, distribution, and shape of the ceramic particles, it is possible to achieve a particular behavior (i.e., specific percolation threshold, breadth of the percolation region, room temperature resistivity).

Various metal oxides, including TiO<sub>2</sub>, VO<sub>2</sub>, and V<sub>2</sub>O<sub>5</sub>, incorporated into a rigid epoxy matrix show large PTC anomalies (from six to eight orders of magnitude) in the vicinity of  $T_f$  [42-45]. We also found these same results for V<sub>2</sub>O<sub>5</sub> in other epoxies as well as in a polyurethane matrix [46]. It is interesting to note that in all of these metal oxide composite systems, a substantial PTC effect is seen over a wide range of filler concentrations.

The appearance of significant PTC resistance effects in certain amorphous polymer composites, but not in others, suggests that several combined factors may be responsible in part for this unusual phenomenon. A systematic study of a particular filler; in a number of amorphous polymers has been performed in order to help determine the nature of this transition. Vanadium (III) oxide, V<sub>2</sub>O<sub>3</sub>,\* has been combined with several amorphous polymer matrices and the resulting behavior has been analyzed. The polymers used

\* In V<sub>2</sub>O<sub>3</sub>, a transition occurs near -100°C and is a result of a change in crystal structure and is accompanied by delocalization of electrons in the structure. In addition to the PTC behavior, this transition may be incorporated into the electrical characteristics of the composite, resulting in an NTC near -100°C.

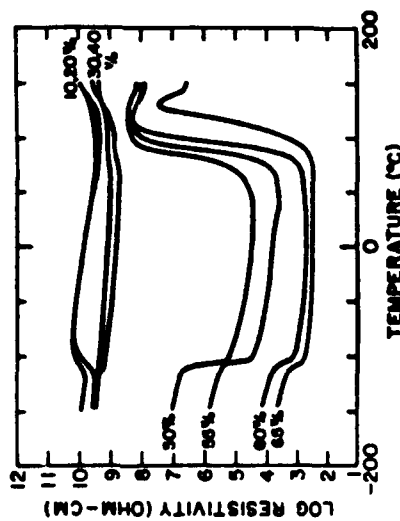


FIGURE 3.3  
Resistivity vs. temperature for  $V_2O_5$ -PMMA composites at 1 kHz.

include: PMMA ( $T_g = 100^\circ\text{C}$ ); two flexible epoxies, Eccogel-0 and Eccogel-45 ( $T_g < -30$  and  $T_g = -30^\circ\text{C}$ , respectively); a rigid epoxy ( $T_g = 80^\circ\text{C}$ ); a silicone elastomer ( $T_g = -100^\circ\text{C}$ ); a polyurethane ( $T_g = 15^\circ\text{C}$ ); bisphenol A polycarbonate ( $T_g = 150^\circ\text{C}$ ); and polystyrene ( $T_g = 100^\circ\text{C}$ ). The  $V_2O_5$ -PMMA system was chosen to illustrate the resistance behavior observed in these amorphous polymer composites. Very similar percolation and temperature behavior is exhibited by the other  $V_2O_5$ -filled amorphous polymers. The percolation behavior of these composites is shown in Fig. 3.2. Here, the threshold is located near 40 vol %  $V_2O_5$ . The threshold concentration is a function of the choice of polymer matrix and the interactions between the filler and polymer. In a system in which the polymer wets the particles well, a higher concentration of filler is required to obtain a large decrease in room temperature resistivity.

The resistivity versus temperature behavior of several  $V_2O_5$ -PMMA composites is illustrated in Fig. 3.3. When the NTC transition in the  $V_2O_5$  is combined with the composite PTC effect, a resistivity-temperature curve with a square-well appearance results. In this case there exists a window of temperatures within which the resistivity can be quite low; beyond this window the resistivity is dramatically higher. As the amount of  $V_2O_5$  in the composite is increased, a PTC effect begins to appear near 50 vol %  $V_2O_5$ . This resistivity increase is more significant for the 60%  $V_2O_5$  composite, the composition with the largest resistance increase for this composite system. This optimum composition yields the lowest room temperature resistivity and the largest PTC effect. In addition, as the amount of conducting filler in the composite increases, the temperature at which the PTC effect occurs moves to somewhat higher temperatures. This illustrates that when there are more

conducting particles in the composite, a larger temperature increase is needed to cause disruption of the percolation pathways and cause an increase in resistivity. Similarly behavior has been noted in the other conductor-filled amorphous polymer composites [46].

In research that has stemmed from the success of transition metal oxides as conducting fillers in composite thermistors, Shrouf et al. have utilized borides, carbides, and silicides of transition metals in order to obtain composites with lower room temperature resistivities and better current handling capabilities [47]. These fillers, such as TiC, TiB<sub>2</sub>, and NbSi<sub>3</sub>, have been incorporated into several amorphous polymer matrices, including epoxies, PMMA, and a silicone elastomer. Although there are some exceptions, the results they obtained are similar to those seen in the transition metal oxide composites: Significant PTC effects over a wide range of concentrations.

The analysis of the nature of the PTC transition in amorphous polymer composites involves several issues. These relate to the key properties of both the filler material and the polymer matrix. The first important question is whether there is a correlation between the PTC transition temperature and the glass transition temperature of the polymer. This may be addressed by analyzing Fig. 3.4, which illustrates the resistance-temperature behavior of a number of 50 vol %  $V_2O_5$ -amorphous polymer composites. Here it is evident that the character of the PTC in these eight systems is quite diverse. Some of the composites exhibit a fairly broad PTC (polystyrene, polyurethane, polycarbonate, Eccogel-0, and Eccogel-45), while others exhibit a reasonably steep transition (PMMA, silicone rubber, Spurr epoxy). The overall appearance of the curves, including the room temperature resistivity, varies from one polymer matrix to another. The PTC transition temperatures for all of these composites except Eccogel-0 and Eccogel-45 fall very near the corresponding polymer's glass transition temperature. It seems apparent, then, that the PTC switching temperature is related in some way to the  $T_g$ , as been indicated earlier [40, 41].

A second important issue involved in understanding the PTC effect is whether the difference in thermal expansion between the polymer and filler is a driving force for the transition. In the literature, this resistivity enhancement has been attributed to the volumetric expansion of the polymer matrix near the polymer's glass transition [40, 41]. Although, as noted earlier, the location of the PTC transition increases with filler concentration (see Fig. 3.3), the importance of differential thermal expansion is not clear at this time. Also of relative importance is the impact of changes in the electrical properties of the polymer as it passes from the glassy to rubbery state at  $T_g$ . Perhaps the barrier height associated with electron transport in the polymer accompanies this change of state. Provided that this or a similar argument is relevant, it would explain why these amorphous polymer composites exhibit PTC anomalies near their glass transition temperature and why this effect seemingly occurs regardless of the level of differential thermal expansion.

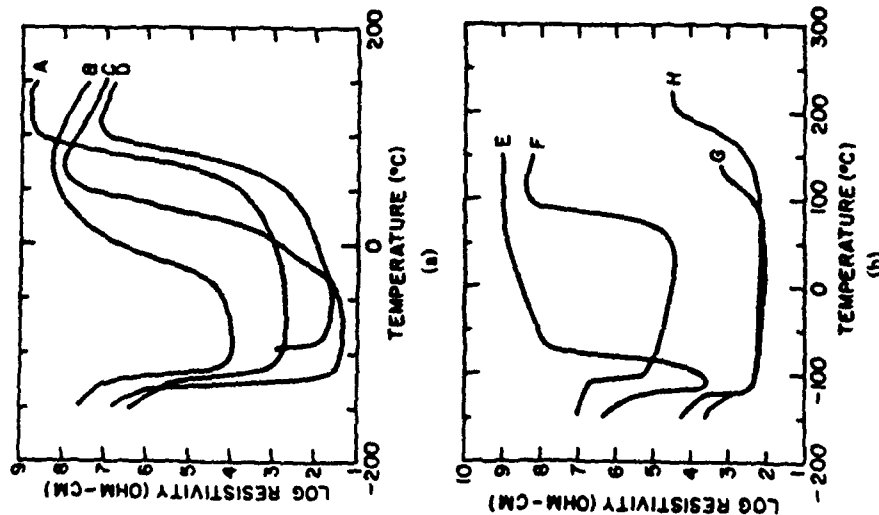


**FIGURE 3.4**  
Resistivity vs. temperature for several  $V_2O_5$ -amorphous polymer composites. (a) A—Spurr B, rigid epoxy; B—polyurethane; C—Eccogel-45, flexible epoxy; and D—Eccogel-0, flexible epoxy. (b) E—silicone elastomer; F—PMMA; G—polystyrene; and H—polycarbonate.

Another issue that arises is the effect of the surface interactions between the conducting filler and insulating matrix. The percolation threshold and therefore the composition at which the optimum PTC effect is observed is related to the ability of the polymer to effectively wet the conducting particles. The 50 vol % filled composite is not necessarily the "best" composition in every system because the percolation behavior varies with the

properties of the polymer matrix and the ceramic-polymer interface. The composition exhibiting the largest PTC effect for a composite with a low percolation threshold will be lower than that of a composite that has a higher critical volume fraction. This also explains the drastic differences in room temperature resistivity from one polymer to another for a given concentration of filler.

In order to better understand the resistivity behavior of these composite thermistors, a theoretical model developed by Sherman et al. [48] was examined. Other models exist [12, 18, 49-52], but this one was chosen because it directly incorporates both temperature and concentration effects on the resistivity. This model, which was originally utilized for carbon black and metal-filled composite systems, incorporates three physical phenomena: percolation, thermal expansion, and quantum mechanical tunneling. It has been previously applied to describe the behavior of nickel particles and carbon black in a polyethylene matrix [48]. We applied this model to  $V_2O_5$ -polyethylene and  $V_2O_5$ -rigid epoxy composites, the details of which are described in a previous publication [46]. The results showed that the model provides a reasonable description of the percolation behavior of the composites, but fell short in predicting the temperature dependence of the resistivity. For example, the model suggests that there would be a PTC effect present in a range of only 5 vol % filler concentration near the percolation threshold in each of these systems. Our experimental results for several polymer composites show that a PTC effect is, in fact, evident over a much wider range of concentrations well above the percolation threshold.

### 3.5. CURRENT RESEARCH

The thrust of our current research is to better understand the mechanism behind the PTC transition observed in amorphous polymer composites, particularly those with transition metal oxide fillers. We are currently focusing on (1) the surface characteristics of the filler, (2) the dispersive behavior of the electrical properties, and (3) current-voltage characteristics. By combining the results of these three studies, we hope to draw some conclusions about the conduction mechanism responsible for the PTC effect in these as well as other composite systems.

Since vanadium is a multivalent ion, there is a chance of a change of valence of the vanadium during procession. To determine the surface valence of the vanadium in the  $V_2O_5$  particles, XPS (X-ray photoelectron spectroscopy) studies of the surface characteristics of the  $V_2O_5$  have been performed. It was determined that there exists a very thin (approximately 50 Å) skin of  $V_2O_5$  surrounding the  $V_2O_5$  particles used in our studies. Since the +5 valence state of vanadium is more stable at room temperature than the +3 state, the presence of this layer is not unreasonable. Further

investigation has shown that when combined with polyethylene in a composite, the  $V_2O_5$  conducting filler maintains its original +5 surface valence state; however, when combined with Spurr B epoxy, indications are that the vanadium oxide surface is reduced to a +3 valence state, therefore eliminating the  $V_2O_4$  surface layer. This fact may be an important key to understanding the nature of the conduction mechanism.

We are also exploring the dispersive behavior of the dielectric constant, dielectric loss, and resistivity, in the composites. This behavior occurs at temperatures greater than the PTC transition temperature, as well as for volume fraction filler less than the percolation threshold. Past investigations into the behavior of composites have included a brief discussion of the dispersive characteristics of the resistivity and dielectric constant [12, 14, 17, 31, 32, 53]. It is generally believed that the resistivity of a material or composite will decrease with increasing frequency. This is similar to the frequency dependence observed in the  $V_2O_5$  composites. There is a relaxation in the resistivity and dielectric constant and preliminary experiments show that this relaxation behavior follows the predictions of Maxwell-Wagner theory, which describes the dispersive character through equivalent RC-circuit analysis and resultant interfacial polarization [17, 51, 52].

There is a continuing interest in the current-voltage characteristics and conduction mechanisms of composites for electrical applications [17, 48]. Temperature, electric field, dispersion of the filler in the polymer, microstructural features, and several other factors control whether the behavior is ohmic or nonohmic. It is generally accepted that at low electric fields and filler concentrations above the percolation threshold, the electrical conductivity is ohmic [11, 14, 30, 35]. At low filler volume fractions, there are substantial regions of insulating polymer between the conducting particles, making electron transport difficult. In this case, any conduction that occurs will be nonohmic or nonlinear in nature. In addition, there may be several mechanisms contributing to the nonlinear conduction. The conductivity will depend on the properties of the filler such as structure, concentration, and dispersion, as well as external factors like temperature and frequency. These studies have shown that electron hopping [32, 54], ion diffusion [32], electron tunneling [36, 54], and space charge buildup [55] are possible mechanisms controlling the resistance of the composite.

Preliminary studies in the  $V_2O_5$ -amorphous polymer systems show that there is ohmic conduction at low temperatures (low resistance state), but as the temperature of the sample is increased through current heating, the sample enters the high resistance state and the I-V characteristics become increasingly nonlinear. Because the composites act as thermistors, it is difficult to heat them externally past their PTC transition temperature. The present goal is to analyze the I-V curves at several temperatures in order to gain insight into the nature of the mechanism responsible for conductivity in these composites.

### 3.6. CONCLUSIONS

The resistive applications of composites has recently become more important. In this chapter the percolation behavior and temperature dependence of the resistivity in conductor-filled amorphous polymer composites has been reviewed. We focus on the PTC behavior, which, from general percolation concepts, is not expected except over a very narrow range of concentrations near the percolation threshold. However, as seen previously for a few conductor-polymer systems, some composites do exhibit a substantial PTC effect, although the origin of this behavior is not clear. Our research has focused on elucidating the mechanism of the PTC anomaly in metal oxide-amorphous polymer composites. Current research is focusing on the effect of particle surface chemistry and examination of I-V and frequency characteristics of the composites.

### ACKNOWLEDGMENTS

We would like to thank the National Science Foundation (Grant DMR-8512147) for its support of this research.

### REFERENCES

1. Heywang, W. "Resistivity Anomaly in Doped Barium Titanate." *J. Amer. Ceram. Soc.* 47 (1964): 484.
2. Doljack, F. A. "Polyswitch PTC Devices—A New Low-Resistance Conductive Polymer-Based PTC Device for Overcurrent Protection." *IEEE Trans. Compon. Hybrids Manuf. Technol.* CHMT-4, (1981): 372.
3. Narkis, M., and A. Vaxman. "Resistivity Behavior of Filled Electrically Conductive Crosslinked Polyethylene." *J. Appl. Polymer Sci.* 29 (1984): 1639.
4. Narkis, M., A. Ram, and Z. Stein. "Effect of Crosslinking on Carbon Black/Polyethylene Switching Materials." *J. Appl. Polymer Sci.* 25 (1980): 1515.
5. Rohlfing, L. "Carbon Black-Polyethylene Composites for Thermistors Applications." Masters thesis, The Pennsylvania State University, 1987.
6. Stauffer, D. *Introduction to Percolation Theory*. London: Taylor and Francis, 1985.
7. Deutscher, G., R. Zallen, and J. Adler, eds. *Percolation Structures and Processes*. Annals of the Israel Physical Society, vol. 5. London: Adam Hilger, 1983.
8. Kirkpatrick, S. "Percolation and Conduction." *Rev. Mod. Phys.* 45 (1973): 574.
9. Zallen, R. *The Physics of Amorphous Solids*. New York: Wiley, 1983.
10. Meyer, J. "Glass Transition Temperature as a Guide to Selection of Polymers Suitable for PTC Materials." *Polymer Eng. Sci.* 13 (1973): 462.
11. Kost, J., M. Narkis, and A. Foux. "Effects of Axial Stretching on the Resistivity of Carbon Black Filled Silicone Rubber." *Polymer Eng. Sci.* 23 (1983): 567.
12. Chung, K. T., A. Sahoo, and A. P. Pica. "Electrical Permittivity and Conductivity of Carbon Black-Polyvinylchloride Composites." *J. Appl. Phys.* 53 (1982): 6867.

13. Ezquerro, T. A., J. Martinaz-Salazan, and F. J. Balta Calleja. "Percolation Threshold of Conductive Polycarbonate/Carbon Composites as Revealed by Electron Microscopy." *J. Mat. Sci. Lett.* 5 (1986): 1065.
14. Klason, C., and J. Kubat. "Influence of Anisotropy on the PTC Effect in Injection Moulded Samples of CB-Filled Polyethylene and Polystyrene." *Internat. J. Polymer Mat.* 11 (1985): 47.
15. Verhelst, W. F., K. G. Wolthuis, A. Voet, P. Ehrburger, and J. B. Donnet. "The Role of Morphology and Structure of Carbon Blacks in the Electrical Conductance of Vulcanizates." *Rubber Chem. Tech.* 50 (1977): 735.
16. Hsu, W. Y., W. G. Holtje, and J. R. Barkley. "Percolation Phenomena in Polymer/Carbon Composites." *J. Mat. Sci. Lett.* 7 (1988): 459.
17. Carley Read, R. E., and C. D. Slow. "An Investigation of Charge Transport Through Rubber." *J. Phys. D* 2 (1969): 567.
18. Balberg, I., N. Binchenbaum, and S. Bozowski. "Anisotropic Percolation in Carbon Black-Polyvinylchloride Composites." *Solid State Comm.* 47 (1983): 989.
19. Mukhopadhyay, R., S. K. De, and S. Basu. "Effect of Metal Concentration on the Electrical Conductivity and Some Mechanical Properties of Poly(methyl Methacrylate)-Copper Composites." *J. Appl. Polymer Sci.* 20 (1976).
20. Bhattacharya, S. K., and A. C. D. Chakklader. "Review on Metal-Filled Plastics. I. Electrical Conductivity." *Polymer-Plast. Tech. Eng.* 19 (1982): 21.
21. Gul, V. F., and M. G. Golubeva. "Investigation of Electrically Conducting Anisotropic Structures in Polymer Materials. Influence of a Magnetic Field on the Conductivity of Polymer Materials Containing Conduction Fillers." *Coll. J. USSR* 30 (1968): 9.
22. Bhattacharya, S. K., S. Basu, and S. K. De. "Effect of Size, Shape, and Oxide Content of Metal Particles on the Formation of Segregated Networks in PVC Composites." *Composites* 177 (1978).
23. Klason, C., and J. Kubat. "Anomalous Behavior of Electrical Conductivity and Thermal Noise in Carbon Black-Containing Polymers at  $T_g$  and  $T_m$ ." *J. Appl. Polymer Sci.* 19 (1975): 831.
24. Miyakawa, K., K. Watanabe, E. Jojima, H. Aida, M. Sumita, and K. Ishikawa. "Electrical Conductivity of Carbon-Polymer Composites as a Function of Carbon Content." *J. Mat. Sci.* 17 (1982): 1610.
25. Kusy, R. P., and D. T. Turner. "Electrical Conductivity of a Polyurethane Elastomer Containing Segregated Particles of Nickel." *J. Appl. Polymer Sci.* 17 (1973): 1631.
26. Nishizawa, T., M. Senna, and H. Kuno. "Preparation, Electrical Resistivity and Its Temperature Dependence of RuO<sub>2</sub>-Polystyrene Composite Powder." *J. Mat. Sci.* 18 (1983): 1346.
27. Das, D., S. Basu, and A. Paul. "PVC-Cu Composites with Chemically Deposited Ultrafine Copper Particles." *J. Mat. Sci.* 15 (1980): 1719.
28. Reich, S. "Percolation and Eddy Currents in Random Close Packed Metal Polymer Composites." *J. Mat. Sci.* 22 (1987): 3391.
29. Voet, A. "Temperature Effect of Electrical Resistivity of Carbon Black Filled Polymers." *Rubber Chem. Tech.* 54 (1980): 42.
30. Siebel, F. K., J. I. Gittleman, and P. Sheng. "Transport Properties of the Composite Material Carbon-Polyvinyl Chloride." *Phys. Rev. B* 18 (1978): 5712.
31. Bhattacharya, S. K., S. Basu, and S. K. De. "Effect of Temperature on the Electrical Conductivity of Poly(vinyl Chloride)-Copper Composites." *J. Appl. Polymer Sci.* 25 (1980): 111.
32. Fawcett, E. O. "Electrical Conduction Mechanism in Carbon Filled Polymers." *IEEE Trans. Power Appar. Syst.* 90 (1971): 913.
33. Ghofraniha, M., and R. Sakhwey. "Electrical Conductivity of Polymers Containing Carbon Black." *Polymer Eng. Sci.* 28 (1988): 58.
34. Matsushita, R., M. Senna, and H. Kuno. "Electrical Resistivity of Hot-Pressed Silver-Polystyrene Powder Mixture." *J. Mat. Sci.* 12 (1977): 509.
35. Balta Calleja, F. J., T. A. Ezquerro, D. R. Rueda, and J. Alonso-Lopez. "Conductive Polycarbonate-Carbon Composites." *J. Mat. Sci. Lett.* 3 (1984): 165.
36. Ferralli, M. W., and A. F. Lewis. "Electrical Charge Transport Mechanisms in Carbon Black Filled Glassy Polymers." In *Phase Transitions—1973*, ed. L. E. Cross, 409. New York: Pergamon, 1974.
37. van Konynenburg, P., B. Lyons, R. Smith-Johannsen, and W. Moyer. U.S. Patent 4,534,889, August 13, 1985.
38. Abdel-Bany, E. M. "Factors Affecting Electrical Conductivity of Carbon Black Loaded Rubber. II. Effect of Concentration and Type of Carbon Black on Electrical Conductivity of SBR." *J. Polymer Sci.: Polymer Chem. Ed.* 17 (1979): 2163.
39. Jachym, B., H. Sodalowski, T. Slupkowski, and R. Zielinski. "Metallic Conductivity of Polyester Resin-Acetylene Carbon Black Compounds." *Phys. Stat. Sol. A* (1974): K159.
40. Nicodemus, L., L. Nicolais, G. Romeo, and E. Scafara. "Temperature Effect on the Electrical Resistivity of Metal/Polymer Composites." *Polymer Eng. Sci.* 18 (1978): 293.
41. Littlewood, S., and B. F. N. Briggs. "Investigation of Current-Interruption by Metal-Filled Epoxy Resin." *J. Phys. D* 11 (1978): 1457.
42. Hu, K. A., J. Runt, A. Safari, and R. E. Newnham. "Composite Thermistors." *Mar. Res. Ser. Sci.* 20 (1986): 475.
43. Hu, K. A., J. Runt, A. Safari, and R. E. Newnham. "TiO-Epoxy Composite Thermistors." *Phase Trans.* 7 (1986): 1.
44. Hu, K. A., J. Runt, A. Safari, and R. E. Newnham. "Electroceramic-Polymer Composite Thermistors." *Ferroelectrics* 68 (1986): 115.
45. Hu, K. A., D. Moffatt, J. Runt, A. Safari, and R. E. Newnham. "V<sub>2</sub>O<sub>5</sub>-Polymer Composite Thermistors." *J. Amer. Ceram. Soc.* 70 (1987): 583.
46. Moffatt, D. M., J. P. Runt, A. Halliyal, and R. E. Newnham. "Metal Oxide-Polymer Thermistors." *J. Mat. Sci.* 24 (1989): 609.
47. Shrout, T., W. Huebner, and D. Moffatt. "Novel Conducting Ceramic-Polymer Composites for High Current Switches." American Ceramic Society Pacific Coast Regional Meeting, San Francisco, October 1988.
48. Sherman, R. D., L. M. Middleman, and S. M. Jacobs. "Electron Transport Processes in Conductor-Filled Polymers." *Polymer Eng. Sci.* 23 (1983): 36.
49. Scarisbrick, R. M. "Electrically Conducting Mixtures." *J. Phys. D* 6 (1973): 2098.
50. Radhakrishnan, S. "Effect of Fillers on the Electrical Conduction in Polymers: Theory of Internal Conduction Mechanism." *Polymer Comm.* 26 (1985): 153.
51. Aharoni, S. M. "Electrical Resistivity of a Composite of Conducting Particles in an Insulating Matrix." *J. Appl. Phys.* 43 (1972): 2462.
52. Kusy, R. P. "Influence of Particle Size Ratio on the Continuity of Aggregates." *J. Appl. Phys.* 487 (1977): 5301.
53. Miyauchi, S., Y. Sorimachi, M. Mitsui, H. Akihida, and K. Ohkita. "Electrical Properties of Carbon-Black Grafted with Polymers Using an Anionic Catalyst." *J. Appl. Polymer Sci.* 29 (1984): 251.
54. Von Hippel, A. *Dielectrics and Waves*. New York: Wiley, 1954.
55. Reboul, J. "Ionic Polarization and Electronic Conduction in Carbon-Black-Filled Polyvinylchloride." *J. Appl. Phys.* 46 (1975): 2961.

**INTRINSIC SIZE EFFECTS  
IN FERROELECTRICS**

**APPENDIX 31**

## SIZE EFFECTS IN FERROELECTRIC THIN FILMS

ROBERT E. NEWNHAM, K. R. UDAYAKUMAR,  
AND SUSAN TROLIER-McKINSTRY

### INTRODUCTION

Beginning with work on the melting behavior of metals, it has been reported that many phase transitions are susceptible to size effects. The melting point of bulk gold, for example, is 1337.58 K, but this temperature drops rapidly for grain sizes below 100 Å (Fig. 36.1). This decrease in the phase transition temperature has been attributed to the change in the ratio of surface energy to volume energy as a function of particle size. Thus, for spherical particles of radius  $r$ , the melting temperature can be predicted from [Eq. (36.1)]

$$\Delta U dV - \Delta S T_r dV - \sigma dA = 0 \quad (36.1)$$

where  $\Delta U$  and  $\Delta S$  are the changes in internal energy and entropy on melting,  $\sigma$  is the interfacial energy between the liquid and the solid, and  $T_r$  is the melting temperature of the particle. If  $\Delta S$  and  $\Delta U$  are temperature independent, then the difference between the bulk and small-particle melting temperatures is inversely proportional to the particle radius according to

$$\frac{T_0 - T_r}{T_0} = \frac{2\sigma}{\rho L r} \quad (36.2)$$

*Chemical Processing of Advanced Materials.*  
Edited by Larry L. Hench and Jon K. West.  
ISBN 0-471-54201-6 © 1992 John Wiley and Sons, Inc.

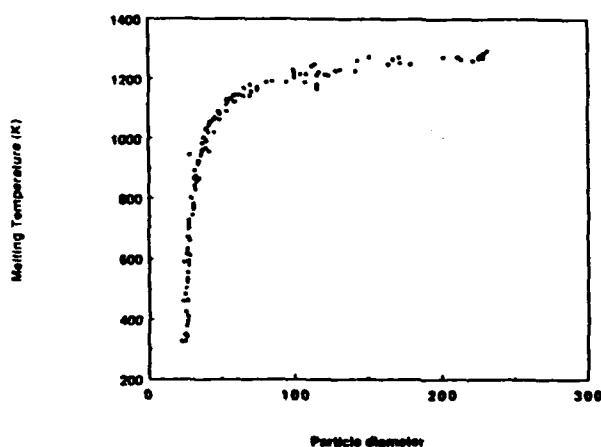


Figure 36.1. Melting temperature of gold particles as a function of size. Taken from Ref. [1].

where  $L$  is the heat of fusion,  $\rho$  the density, and  $T_0$  the bulk melting point.

It is interesting that many types of equilibrium phase transitions display comparable size effects. In addition to the data on gold particles, the melting temperatures of copper [3], tin [4], indium [5], lead, and bismuth [2] particles and thin films have all been shown to be size dependent. Similarly, the superconducting transition depends on size both intrinsically [6, 7] and extrinsically if the stress exerted on the superconducting phase is different at different sizes [8]. Superfluid transitions in He-impregnated powder compacts and thin films also depend on either the film thickness or the size of the pore diameter [9].

In ferroic materials, both the presence of domain walls and the ferroic transition itself are influenced by crystallite size. While this has not previously been critical to most applications, with the growing importance of thin-film- and small-particle-based devices, it is becoming important to understand the size effects expected in ferroic materials.

## REVIEW OF FERROIC SIZE EFFECTS

In brief, we expect four regions in the size dependence of ferroic properties (Fig. 36.2). In large crystallites, multidomain effects accompanied by hysteresis take place. Reductions in size lead to single-domain particles and, at yet smaller sizes, to destabilized ferroics with large property coefficients. Finally, at sufficiently small sizes a reversion to normal behavior is expected at the point where there are simply too few unit cells to sustain cooperative behavior. Similar transitions with size are expected in secondary ferroics. As an introduction to the intrinsic size effects in ferroelectric films, it is instructive to review what is known about the transitions between regions in ferroic particles.

Beginning with the larger end of the size spectrum, it is well known that large-

grained ferroic ceramics exhibit complex domain structures that are bordered by several types of domain walls. As the size of the system decreases, however, the volume free energy necessarily decreases as well, and it becomes increasingly difficult to support the free-energy term associated with domain walls [10]. Consequently, the number of domains is expected to diminish as first one and then the other types of domain walls are eliminated. The transition from polydomain to single-domain behavior is well documented in a number of ferromagnets. Pure iron suspended in mercury, for example, shows a critical size for conversion to single-domain behavior at  $\sim 23$  nm and  $\text{Fe}_{0.4}\text{Co}_{0.6}$  a critical size of  $\sim 28$  nm [11]. This is in good agreement with the calculations of Kittel, who suggested 20 nm as the minimum size for multidomain behavior in magnets [10]. Results for acicular agglomerates of  $\gamma\text{-Fe}_2\text{O}_3$  particles separated by nonmagnetic grain boundaries are also consistent with these estimates; Berkowitz et al. [12] report that the stable single-domain range at room temperature is centered at  $\sim 40$  nm.

Although the loss of multidomain behavior in ferroelectric ceramics is known to occur for much larger grain sizes (approximately several tenths of a micrometer), it is also clear that the stress state in a monolithic body containing domains is considerably more complex than that for isolated particles. Consequently, the changes in ferroic properties as a function of size in ferroelectric powders are expected to follow the ferromagnetic analog more closely. This is born out in experiments on 0-3  $\text{PbTiO}_3$ /polymer composites in which the filler

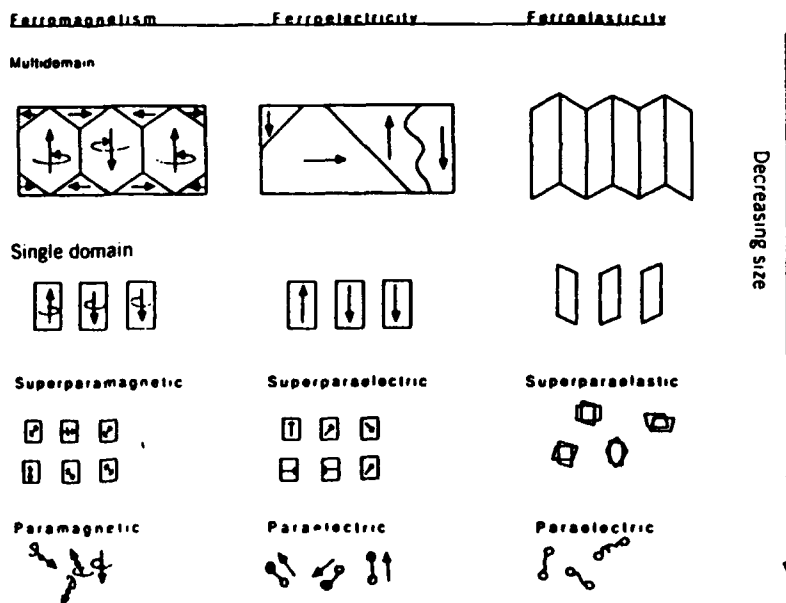


Figure 36.2. Transitions in ferroic behavior as a function of size.

particle size was varied. Lee et al. [13] report that there is a significant drop in the ability to pole such composites for filler particles smaller than  $\sim 200$  nm. Assuming both that the small particles were well crystallized and that the particle size distributions were narrow, this implies that transition from multidomain to single domain occurs in  $\text{PbTiO}_3$  particles near 200 nm.

At still smaller sizes, ferroic materials undergo a phase change to the high-temperature prototype group. In the case of ferromagnetic particles, this has been correlated with the size at which the decrease in volume free energy accompanying magnetization is on the order of the thermal energy [14]. As a result, the spin direction is randomized with time, leading to an unmagnetized but highly orientable single-domain crystal. Thus, a magnet in this size regime is characterized by a zero net magnetization, the disappearance of a magnetic hysteresis loop, extremely high magnetic susceptibilities, and a symmetry that, on average, is higher than that of the ferromagnetic phase. Iron exhibits superparamagnetic behavior at particle sizes near 7 nm [11],  $\gamma\text{-Fe}_2\text{O}_3$  at  $\sim 30$  nm [12] and  $\text{BaFe}_{1-2x}\text{Ti}_x\text{Co}_x\text{O}_{19}$  at 15–35 nm depending on the stoichiometry and the degree of particle shape anisotropy [15]. The loss of the ferroic hysteresis loop coupled with the ability to respond strongly to the presence of a magnetic field has been utilized in a variety of applications, including ferromagnetic fluids and high-frequency transformers where eddy current losses are a problem.

A similar mechanism has been proposed to explain the dielectric and elastic properties of relaxor ferroelectrics [16, 17]. Compositions including many of the  $\text{A}(\text{B}'_{1/2}, \text{B}''_{1/2})\text{O}_3$  and  $\text{A}(\text{B}'_{2/3}, \text{B}''_{1/3})\text{O}_3$  exhibit microdomains (typically 2–30 nm in size) of 1:1 ordering on the B sublattice dispersed in a disordered matrix. It has been suggested that as a result of this nanostructure, the spontaneous polarization in these materials is also subdivided into very small local regions. Thus, a lead magnesium niobate ceramic can be regarded as a collection of disordered but highly orientable dipoles. The result, much like the case of superparamagnetism, is a high dielectric permittivity over a broad temperature range even though the net spontaneous polarization is zero. Because of the long range of the electric fields induced by the local dipoles, however, there is more interaction between the local electric dipoles than was present in the ideal superparamagnet. Consequently, the superparaelectric behavior in relaxor ferroelectrics is modulated by coupling between local moments, so that a spin glass model is necessary to describe the phase transition behavior [17]. Evidence for the importance of the size of the microregions is given in experiments on materials that can be ordered by heat treatment. As the scale of the ordered regions grow beyond a certain size, the material reverts to ordinary ferroelectric (or antiferroelectric) behavior with a well-defined transition temperature and a nondispersive dielectric response.

As yet, direct observation of superparaelectric behavior in particulate ordinary ferroelectrics has not been documented. Recently, however, many investigators have attempted to determine the critical size for reversion to the high-temperature prototype symmetry [18–20]. As in the case of the melting of

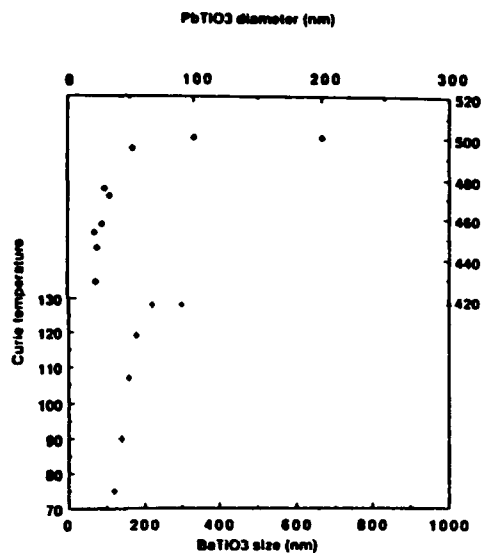


Figure 36.3. Transition temperature for ferroelectric powder. Data from Refs. [18, 19].

metal particles, as the particle size is decreased, the transition temperature drops markedly (Fig. 36.3). While at larger sizes the high-symmetry phase is the ordinary paraelectric phase, as the size of the ferroelectric particles becomes small enough that thermal energy can disorder the dipoles, there should be a transition from paraelectric to superparaelectric particles. The reported results indicate that unconstrained BaTiO<sub>3</sub> particles show the transition to a cubic phase near 80–120 nm [19], whereas PbTiO<sub>3</sub> is stable in the tetragonal form to ~10–20 nm [13, 18]. Because it is difficult to characterize the electrical properties of such small particles, it is not known if and when the high-symmetry particles actually become superparaelectric. On the other hand, NaNO<sub>2</sub> shows only some broadening in the differential thermal analysis (DTA) characteristic for the ferroelectric phase transition with no change in the transition temperature for particle sizes down to 5 nm. While it is an order–disorder ferroelectric, and so might have different size dependence for the properties than would a displacive ferroelectric, it is interesting that there is no evidence for superparaelectricity even at particle sizes of 5 nm.

It is also critical to note that it is possible to shift the critical size for reversion to high-temperature symmetry with changes in the processing. Residual strains, in particular, have been shown to drastically affect the properties of BaTiO<sub>3</sub> [21]. Thus, it is not surprising that heavily milled BaTiO<sub>3</sub> powders with an average radius of ~10 nm have been shown to possess permanent dipole moments [22].

Saegusa et al. [20] examined the solid solution between BaTiO<sub>3</sub> and PbTiO<sub>3</sub> to determine the critical size for stabilization of the cubic phase to room

temperature as a function of composition. Assuming that crystallinity and stoichiometry were maintained for the smallest sizes, their data suggest that the critical size is *not* a linear function of composition. It would be interesting to follow the magnitude of the polarization as a function of temperature in such powders to see how its magnitude is affected by particle size.

Although the general outline of size effects expected in films are similar to those demonstrated in ferromagnetic particles, it would not be surprising for the boundaries between different regions to shift along the size axis for different geometries. Kittel was one of the first to explore this possibility in ferromagnetic materials [10]. He calculated that in a film where the preferred magnetization is perpendicular to the major surface, the multidomain to single-domain transition should occur near 300 nm, an order of magnitude larger than the same transition in a particulate material. If, however, there was either no anisotropy or the easy magnetization direction fell in the film plane, new types of domain walls may appear and persist down to very small sizes.

The transition to superparamagnetic behavior is apparently suppressed in comparatively perfect thin films produced in high-vacuum systems, probably because the large two-dimensional area raises the volume energy above the available thermal energy, even for very thin films. Consequently, regular ferromagnetic behavior persists in much thinner films (down to  $\sim 0.5$  nm for Ni films sandwiched between nonmagnetic layers [23]). In such samples, the ferromagnetic transition temperature also drops rapidly for films  $< 15$  nm thick.

Films that grow as discrete islands of magnetic material rather than continuous layers or that consist of magnetic particles isolated from each other by nonmagnetic hydride or oxide layers, on the other hand, should behave like particulate systems (undergoing superparamagnetic transitions appropriate for the primary magnetic particle size). This type of behavior has been confirmed in ferromagnetic films that became superparamagnetic at apparent thicknesses of 2.7 nm (where the film actually consisted of 5–10-nm islands [24]). It is interesting that no change in the Curie temperature was noted before the onset of thermal randomization of the spins.

Given this information, what can be predicted about the behavior of ferroelectric thin films? First, for an unelectroded film it seems likely that ferroelectricity will remain stable at least down to thicknesses of  $\sim 100$  nm for  $\text{BaTiO}_3$  and possibly considerably lower for  $\text{PbTiO}_3$  films. This is in accord with several theoretical predictions for size effects in thin ferroelectric wafers. In that work, it was shown that when space charge effects (which will be considered in the following section) are discounted, the onset of intrinsic size effects is projected to fall in the range of 1–10 nm [25].

Multidomain configurations should also remain stable down to very small sizes. Corroborating evidence for this is suggested by transmission electron microscopy (TEM) studies of thinned ferroelectric ceramics and single crystals where, provided the grain size is large enough, domains can be detected in foils below 100 nm thick [26]. When, however, the grain size in the film falls below

some critical limit, the density of domains will probably decrease in a manner similar to that shown in ceramics [27].

Finally, as in the case of the magnetic films, unless there is some extrinsic mechanism for forming discrete polar microregions, the onset of superparaelectricity should be depressed by the relatively large volume of ferroelectric.

### THIN-FILM SIZE EFFECTS

The experimentally observed size effects reported in the ferroelectric thin-film literature fall into four major categories: an increase in the coercive field, a decrease in the remanent polarization, a depression in the dielectric constant, and a smearing of the paraelectric-ferroelectric transition over values expected from bulk materials of the same composition. Typical data on the first two observations are listed in Table 36.1, the third is depicted in Fig. 36.4, and the fourth point is discussed by Biryukov et al. [28]. One point that is immediately apparent from Table 36.1 and a perusal of literature data is that deviations from bulk properties are nearly universal, but the thickness at which the properties begin to diverge and the magnitude of the disparity are strongly dependent on

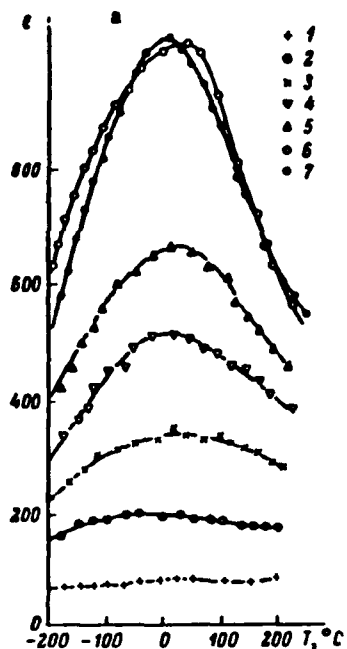


Figure 36.4. Temperature dependences of  $\epsilon$  (a) and  $\tan \delta$  (b) for  $(\text{Ba,Sr})\text{TiO}_3$  films. Film thickness  $d$  (micrometers): (1) 0.1; (2) 0.33; (3) 0.5; (4) 1.0; (5) 2.0; (6) 5.0; (7) 8.2. Data from Ref. [52].

TABLE 36.1. Remanent Polarization and Coercive Field in a Number of Perovskite Films

Material <sup>a</sup>	$P_r$ ( $\mu\text{C}/\text{cm}^2$ )	$E_c$ (kV/cm)	Reference
Single-crystal $\text{PbTiO}_3$	~55-75	6.75	35
Sol-gel $\text{PbTiO}_3$	3.37	54.8	36
Sputtered (001) $\text{PbTiO}_3$	55	75	37
Sputtered (001) $\text{PbTiO}_3$	35	160	38
Sputtered or CVD $\text{PbTiO}_3$	12	250	39
CVD (001) $\text{PbTiO}_3$	14.1	20.16	40
Bulk PZT 58/42	45	17	41
Sol-gel PZT	36		42
Sol-gel PZT 53/47	12	150	43
Sol-gel PZT 52/48	35		34
Sol-gel PZT	18-20	50-60	44
Sol-gel PZT 40/60	6.6	26.7	45
Sputtered PZT 90/10	13.9	60.0	46
Sputtered PZT 58/42	30.0	25	41
Sputtered PZT 65/35, weak (100)	12.5	90	47
Sputtered PZT 65/35	3.6	33	47
Sol-gel PLZT 2/54/46	28.5	190	48
Single-crystal $\text{BaTiO}_3$	26	1	49
Polycrystalline $\text{BaTiO}_3$	8	3	49
Sputtered $\text{BaTiO}_3$	0.8	3	50
Screen-printed $\text{BaTi}_{0.95}\text{Sn}_{0.05}\text{O}_3$	1.7-2.8	25	51
Sputtered (001) $\text{BaTiO}_3$	7	60	33
Sputtered $\text{BaTiO}_3$ , weak (101)	16	20	33

<sup>a</sup>Abbreviations: CVD, chemical vapor deposition; PZT, lead zirconate titanate; PLZT, lead lanthanum zirconate titanate.

the preparation conditions. Consequently, films produced at one laboratory may display marked size effects, while others of the same thickness and composition possess bulk properties.

The reasons for this type of discrepancy lie in the variety of mechanisms causing the apparent size effect. Included among these are microstructural heterogeneities, variations in crystalline quality, mechanical stresses imposed on the film by the substrate, space charge effects, and finally intrinsic size effects. It is critical to note that the first two of these, which in the opinion of the authors account for the majority of the "size effects" observed in thin-film properties, are, in fact, size independent. It is fortuitous, then, that many film preparation techniques produce films that are defective and would remain defective even if macroscopic samples could be fabricated.

Inhomogeneity in the film microstructure can take the form of incorporated porosity, surface and interface roughness, or variations in the grain size. In particular, many ferroelectrics grown by vapor deposition processes are columnar and should be expected to have low densities (Fig. 36.5). This, in turn,

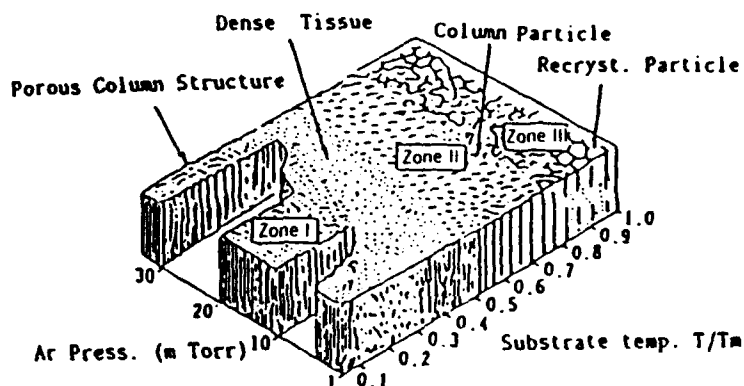


Figure 36.5. Structure of sputtered film as a function of gas pressure and normalized substrate temperature [37].

could appreciably lower the dielectric constant and, if there was poor coupling between the grains, would increase the coercive field as well [29]. Even in films that appear dense, Dudkevich et al. have shown that the microstructure may change continuously as a function of film thickness [30]. Thus, for sputtered  $\text{Ba}_{0.85}\text{Sr}_{0.15}\text{TiO}_3$  films, thinner films tend to be composed of small particles (15 nm for a 4-nm-thick film) where thicker films show a distribution of grain sizes ranging from the very fine particles deposited next to the substrate to larger grains at the film surface (200–300 nm for a film 2000 nm thick). Given this type of microstructural heterogeneity, it is no wonder that many properties appear to depend on film thickness. As the absolute grain size at any given thickness is expected to be a sensitive function of both the deposition conditions and any postannealing, samples prepared at different laboratories should behave differently.

A second significant influence on thin-film properties is the crystalline quality of the ferroelectric material. It is known that the loss of clear X-ray diffraction peaks is coupled to the disappearance of the paraelectric-ferroelectric phase transition. Unfortunately, many film deposition techniques also result in poor crystallinity. During sputtering, for example, the growing film is subjected to bombardment by high-energy ions. While this can be advantageous in terms of providing additional energy to the deposit and increasing the surface mobility, heavy bombardment, particularly at low substrate temperatures, can also introduce high defect concentrations. In chemically prepared thin films, on the other hand, low annealing temperatures can be insufficient to crystallize the ferroelectric phase fully.

Fast neutron irradiation of  $\text{BaTiO}_3$  single crystals (neutron energy  $\geq 50$  keV), for example, eventually introduces sufficient defects that the material transforms into a metastable cubic state with an expanded lattice parameter [31]. Having undergone this transition, no displacive transformation to the tetragonal, ferroelectric, state can be detected at temperatures above 78 K. Although the

bulk still displays some long-range order, the X-ray peaks are broadened by a factor of 5 over the unirradiated crystal, and it is not unlikely that the surface was completely amorphized. Annealing to 1000°C is required before the lattice parameter relaxes back to its initial value. Unfortunately, in many thin films, annealing temperatures are kept as low as possible to minimize changes in stoichiometry. While this may help maintain the perovskite structure, it is probable that 500–700°C is insufficient to crystallize amorphous or badly damaged films fully. Many authors working with either vacuum-deposited or chemically prepared thin films report modifications of the perovskite structure with a slightly expanded cubic unit cell [32].

In characterizing the crystallinity of ferroelectric films, Surowiak et al. [33] measured lattice strains in sputter-deposited BaTiO<sub>3</sub> films. They found that films that experienced heavy bombardment during growth tended to have more heavily deformed crystallites (i.e., the mean microdeformation  $\Delta d/d$  was as large as 0.01–0.005) and small coherent scattering sizes. Larger, less defective crystallites ( $\Delta d/d < 0.005$ ) could be formed when the growth conditions were not as rigorous [33]. Differences between the two types of films were readily apparent in the electrical properties: lower  $\Delta d/d$  values were associated with high remanent polarizations, piezoelectric constants close to single-crystal values, and relatively narrow phase transitions. This last point was examined by Biryukov et al. [28], who demonstrated that films with large lattice strains should be expected to show diffuse phase transitions. Poorly crystallized films from any preparation method will probably display low remanent polarization, lowered dielectric and electromechanical coupling constants, and diffuse phase transitions.

It is not surprising that mechanical stresses should also affect thin-film properties. As in most ferroic materials, the appearance of the order parameter at the transition temperature is accompanied in perovskite ferroelectrics by a spontaneous strain. Domain structure should be influenced by the types of strains present in the film. In a similar way, stresses in heteroepitaxial films have been shown to alter the equilibrium domain structure. Two-dimensional stresses can stabilize the ferroelectric phase to higher temperatures in bulk materials and this mechanism could operate in thin films when there is good cohesion between the substrate and the film.

The primary difference between size effects in ferromagnetic materials and ferroelectric materials is that, in the electrical analog, it is necessary to compensate the polarization at the surface of the material. In a ferroelectric that is slightly conducting or electroded with a material with a low carrier density, tremendous depolarization fields or space charge migration can be generated even in comparatively thick films ( $\sim 1 \mu\text{m}$ ). These can shift the phase transition temperature, lower the magnitude of the spontaneous polarization, and even destabilize the ferroelectric phase in the film.

Despite all of these opportunities for extrinsic size effects, there is evidence that films that are prepared carefully can display near bulk properties to very

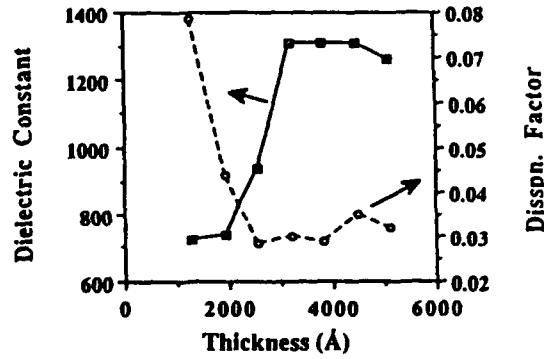


Figure 36.6. Dielectric constant and dispersion factor as a function of film thickness.

small thicknesses. In work on sol-gel PZT films, Udayakumar [34], for example, showed that room temperature dielectric constants of ~1300 could be maintained for films exceeding 300 nm thick (Fig. 36.6). The bulk remanent polarization was retained to 450 nm and remained finite, though reduced, in films 190 nm thick (Fig. 36.7). The high breakdown strength of these films (Fig. 37.8) will also be critical in device applications [34].

In work on RF-sputtered BaTiO<sub>3</sub> films, Dudkevich et al. [30] showed that the size of the coherent scattering region, *D*, within their films was more important than the thickness in determining the macroscopic electrical properties. As seen in Fig. 36.9, the dielectric constant increases markedly as the

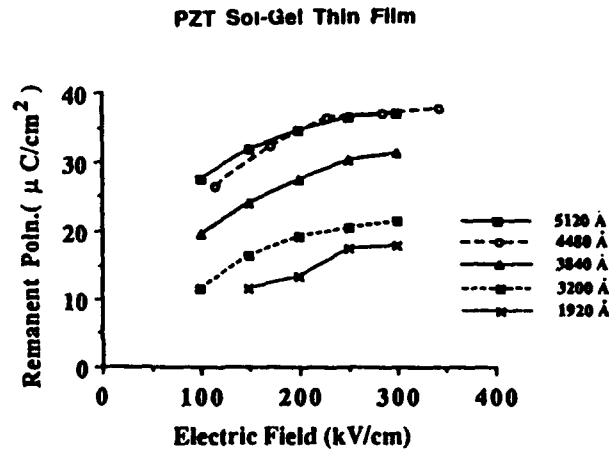


Figure 36.7. Remanent polarization in PZT sol-gel thin films as a function of electric field.

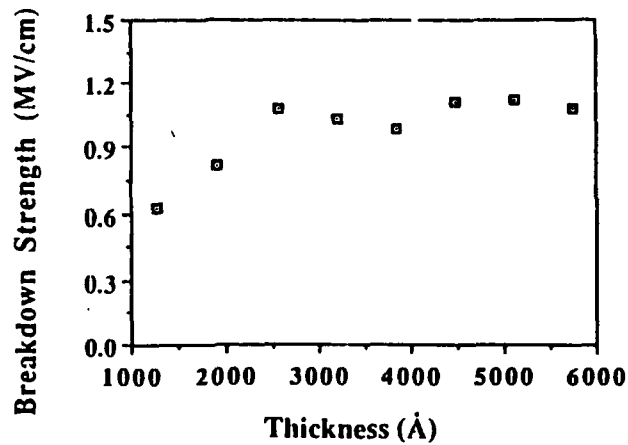


Figure 36.8. Breakdown strength as a function of film thickness.

coherent scattering size grows larger than  $\sim 30$  nm, and when  $D$  reached 50 nm, room temperature dielectric constants exceeding 1000 were achieved, and some indication of a dielectric constant peak could be detected at the Curie temperature [30].

As shown in Table 36.1, several other recent papers have demonstrated that it is possible to achieve bulk or near bulk properties for several members of the perovskite family.

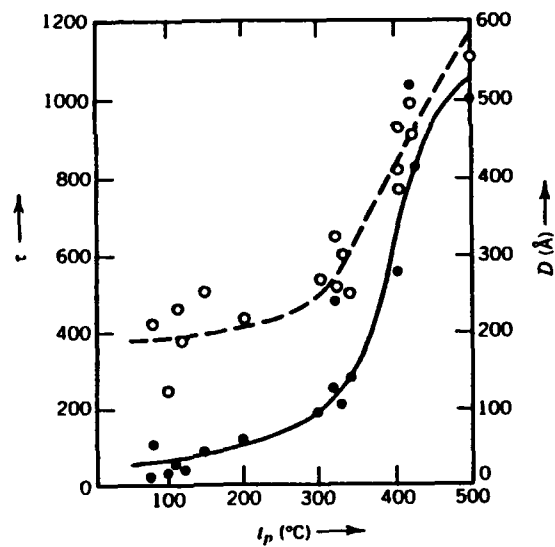


Figure 36.9. Size of the coherent scattering region (curve 1) and the dielectric permittivity (curve 2) of  $\text{BaTiO}_3$  films as a function of substrate temperature. Taken from Ref. [30].

## CONCLUSIONS

As the field of ferroelectric thin films grows, it becomes increasingly important to examine the role of size effects on the expected properties. While intrinsic size effects similar to those demonstrated in ferromagnetic analogs will act as lower limits to the size of ferroelectric devices, in many cases extrinsic, processing-induced contributions overshadow the fundamental size restrictions. Consequently, careful characterization of films to determine the role of extrinsic effects (i.e., internal microstructure, interface layers, and poor crystallinity) are necessary to understand relationships between processing and properties in ferroelectric films.

## REFERENCES

1. Ph. Buffat and J. P. Borel, Size Effect on the Melting Temperature of Gold Particles, *Phys. Rev. A* **13**(6), 2287-2298 (1976).
2. M. Takagi, Electron-Diffraction Study of Liquid-Solid Transition in Thin Metal Films, *J. Phys. Soc. Jpn.*, **9**(3), 359-363 (1954).
3. N. T. Gladkikh, R. Niedermayer, and K. Spiegel, Nachweis großer schmelzpunktserniedrigungen bei dünnen metallschichten, *Phys. Stat. Sol.*, **15**, 181-191 (1966).
4. M. Blackman and A. E. Curzon, On the Size Dependence of the Melting and Solidification Temperatures of Small Particles of Tin, *Structure and Properties of Thin Films*, Wiley, New York (1959).
5. B. T. Boiko, A. T. Pugachev, and Y. M. Bratsykhin, Melting of Subcritically Thin Condensed Films of Indium, *Sov. Phys. Sol. State*, **10**(12), 2832-2834 (1969).
6. M. Ido, Fluctuation Effect on the Knight Shift of Superconducting Al Fine Particles, *J. Phys. Soc. Jpn.*, **41**(2), 412-418 (1976).
7. I. Hlasnik et al., Properties of Superconducting NbTi Superfine Filament Composites with Diameters  $< \sim 0.1 \mu\text{m}$ , *Cryogenics*, **25**, 558-565 (1985).
8. J. H. P. Watson, Critical Magnetic Field and Transition Temperature of Synthetic High-Field Superconductors, *Phys. Rev.* **148**(1) 223-230 (1966).
9. T. Chainer, Y. Morii, and H. Kojima, Size Effects in Superfluid  $^3\text{He}$ , *Phys. Rev. B*, **21**(9), 3941-3944 (1980).
10. C. Kittel, Theory of the Structure of Ferromagnetic Domains in Films and Small Particles, *Phys. Rev.*, **70**(11, 12), 965-971 (1946).
11. E. F. Kneller and F. E. Luborsky, Particle Size Dependence of Coercivity and Remanence of Single-Domain Particles, *J. Appl. Phys.*, **34**(3), 656-658 (1964).
12. A. E. Berkowitz, W. J. Schuele, and P. J. Flanders, Influence of Crystallite Size on the Magnetic Properties of Acicular  $\gamma\text{-Fe}_2\text{O}_3$  Particles, *J. Appl. Phys.*, **39**(2), 1261-1263 (1968).
13. M. H. Lee, A. Halliyal, and R. E. Newnham, Poling Studies of Piezoelectric Composites Prepared by Coprecipitated  $\text{PbTiO}_3$  Powder, *Ferroelectrics*, **87**, 71-80 (1988).
14. C. P. Bean and I. S. Jacobs, *J. Appl. Phys.*, **27**(12), 1448 (1956).
15. O. Kubo, T. Ido, H. Yokoyama, and Y. Koike, Particle Size Effects on Magnetic Properties of  $\text{BaFe}_{12-2x}\text{Ti}_x\text{Co}_x\text{O}_{19}$  Fine Particles, *J. Appl. Phys.*, **57**(1), 4280-4282 (1985).
16. L. E. Cross, Relaxor Ferroelectrics, *Ferroelectrics*, **76**(3/4), 241-267 (1987).
17. D. Viehland, S. J. Jang, L. E. Cross, and M. Wuttig, Freezing of the Polarization Fluctuations in Lead Magnesium Niobate Relaxors, *J. Appl. Phys.*, **68**(6), 2918-2921 (1990).

18. K. Ishikawa, K. Yoshikawa, and N. Okada, Size Effects on the Ferroelectric Phase Transition in  $\text{PbTiO}_3$  Ultrafine Particles, *Phys. Rev. B*, **37**(10), 5852-5855 (1988).
19. K. Uchino, preprint, American Ceramic Society annual meeting (1989).
20. K. Saegusa, W. E. Whine, and H. K. Bowen, Preparation of  $\text{Pb}_x\text{Ba}_{1-x}\text{TiO}_3$  and the effect of Composition and the Size of the Crystallite on the Crystal Phase, preprint, American Ceramic Society annual meeting (1989).
21. S. Jyomura, I. Matsuyama, and G. Toda, Effects of the Lapped Surface Layers on the Dielectric Properties of Ferroelectric Ceramics, *J. Appl. Phys.*, **51**(11), 5838-5844 (1980).
22. R. Bachmann and K. Barner, Stable Suspensions of Ferroelectric  $\text{BaTiO}_3$  Particles, *Sol. State Commun.*, **68**(9), 865-869 (1988).
23. P. Beauvillain, C. Chapert, J. P. Renard, C. Marliere, and D. Renard, Magnetic Interaction Between Ultrathin Nickel Films Through a Gold Interlayer, in *Magnetic Thin Films*, 1986, R. Krishnan ed., les editons de physique, France (1986).
24. M. Prutton, *Thin Ferromagnetic Films*, Butterworth and Co. Ltd, Washington (1964).
25. K. Binder, Surface effects on Phase Transitions in Ferroelectrics and Antiferroelectrics, *Ferroelectrics* **35**, 99-104 (1981).
26. M. Tanaka and G. Honjo, Electron Optical Studies of Barium Titanate Single Crystal Films, *J. Phys. Soc. Jpn.*, **19**(6), 954-970 (1964).
27. G. Arlt, D. Hennings, and G. de With, Dielectric Properties of Fine-Grained Barium Titanate Ceramics, *J. Appl. Phys.*, **58**(4), 1619-1625 (1985).
28. S. V. Biryukov, V. M. Mukhortov, A. M. Margolin, Yu. I. Golovko, I. N. Zakharchenko, V. P. Dudkevich, and E. G. Fesenko, Phase Transitions in Polycrystalline and Heteroepitaxial Ferroelectric Films, *Ferroelectrics*, **56**, 115-118 (1984).
29. Q. Jiang, The Pennsylvania State University private communication (1990).
30. V. P. Dudkevich, V. A. Bukreev, V. M. Mukhortov, Yu. I. Golovko, Yu. G. Sineev, V. M. Mukhortov, and E. G. Fesenko, Internal Size Effect in Condensed  $\text{BaTiO}_3$  Ferroelectric Films, *Phys. Stat. Sol. (a)*, **65**, 463-467 (1981).
31. M. C. Wittels and F. A. Sherrill, Fast Neutron Effects in Tetragonal Barium Titanate, *J. Appl. Phys.*, **28**(5), 606-609 (1957).
32. S. Naka, F. Nakakita, Y. Suwa, and M. Inagaki, Change from Metastable Cubic to Stable Tetragonal Form of Submicron Barium Titanate, *Bull. Chem. Soc. Jpn.*, **47**(5), 1168-1171 (1974).
33. Z. Surowiak, A. M. Margolin, I. N. Zakharchenko, and S. V. Biryukov, The Influence of Structure on the Piezoelectric Properties of  $\text{BaTiO}_3$  and  $(\text{BaSr})\text{TiO}_3$  Thin Films with a Diffuse Phase Transition, *Thin Solid Films*, **176**, 227-246 (1989).
34. K. R. Udayakumar, J. Chen, S. B. Krupanidhi, and L. E. Cross, Sol-Gel Derived PZT Thin Films for Switching Applications, paper presented at the International Symposium on Applications of Ferroelectrics 1990 (1990).
35. V. G. Gavriyachenko, R. I. Spinko, M. A. Martynenko, and E. G. Desenki, Spontaneous Polarization and Coercive Fields of Lead Titanate, *Sov. Phys. Sol. State*, **12**(5), 1203-1204 (1970).
36. A. X. Kuang, L. S. Wu, and Q. F. Zhou,  $\text{PbTiO}_3$  Thin Film Prepared by Sol-Gel Process, *ISAF 1990 Abstr.*, X.34 (1990).
37. E. Yamaka, H. Watanabe, H. Kimura, H. Kanaya, and H. Okhuma, Structural, Ferroelectric, and Pyroelectric Properties of Highly c-Axis Oriented  $\text{Pb}_{1-x}\text{Ca}_x\text{TiO}_3$  Thin Film Grown by Radio-frequency Magnetron Sputtering, *J. Vac. Sci. Technol. A*, **6**(5), 2921-2928 (1988).
38. K. Iijima, Y. Tomita, R. Takayama, I. Ueda, Preparation of c-Axis Oriented  $\text{PbTiO}_3$  Thin Films and Their Crystallographic, Dielectric, and Pyroelectric Properties, *J. Appl. Phys.*, **60**(1), 361-367 (1986).
39. M. Okuyama and Y. Hamakawa, Preparation and Basic Properties of  $\text{PbTiO}_3$  Ferroelectric Thin Films and Their Device Applications, *Ferroelectrics*, **63**, 243-252 (1985).

40. S.-G. Yoon, H. Y. Lee, and H. G. Kim, Compositional Analysis of Lead Titanate Thin Films by Auger Electron Spectroscopy and Their Electrical Properties, *Thin Solid Films*, **171**, 251-262 (1989).
41. K. Sreenivas and M. Sayer, Characterization of Pb(Zr, Ti)O<sub>3</sub> Thin Films Deposited from Multi-element Metal Targets, *J. Appl. Phys.*, **64**(3), 1484-1493 (1988).
42. D. A. Payne, Integration of Ferroelectric Materials on Semiconductors by Sol-Gel Methods, *ISAF 1991 Abstr.*, 12.1 (1990).
43. H. Nagata, M. Watanabe, H. Sakai, and Y. Kubota, Thin Film Ferroelectrics of PZT System by Sol-Gel Processing, *ISAF 1990 Abstr.*, X.1 (1990).
44. S. K. Dey and R. Zuleeg, Sol-Gel Ferroelectric Thin Films Merged with GaAs JFET Memory Technology, *ISAF 1990 Abstr.*, 12.2 (1990).
45. G. Yi, Z. Wu, and M. Sayer, Preparation of Pb(Zr, Ti)O<sub>3</sub> Thin Films by Sol Gel Processing: Electrical, Optical, and Electro-optic Properties, *J. Appl. Phys.*, **64**(5), 2717-2724 (1988).
46. T. Okamura, M. Adachi, T. Shiosaki, and A. Kawabata, Epitaxial Growth of Ferroelectric Pb(Zr<sub>0.9</sub>Ti<sub>0.1</sub>)O<sub>3</sub> Films by Reactive Sputtering of Multi Metal Target, *ISAF 1990 Abstr.*, X.5 (1990).
47. A. Croteau, S. Matsubara, Y. Miyasaka, and N. Shohata, Ferroelectric Pb(Zr, Ti)O<sub>3</sub> Thin Films Prepared by Metal Target Sputtering, *Jpn. J. Appl. Phys.*, **26**(Suppl. 26-2), 18-21 (1987).
48. Z. Wu and M. Sayer, Properties of Sol-Gel Processed PLZT (2/54/46) Thin Films, *ISAF 1990 Abstr.*, X.6 (1990).
49. B. Jaffe, W. R. Cook, Jr., and H. Jaffe, *Piezoelectric Ceramics*, Academic, India (1971).
50. T. Nagatomo and O. Omoto, Preparation of BaTiO<sub>3</sub> Films by rf Sputtering and Their Crystallographic, Dielectric, and Optical Properties, *Jpn. J. Appl. Phys.*, **26**(Suppl. 26-2), 11-14 (1987).
51. M. Lopuszko, M. Pawelczyk, M. Urbanska, and Z. Surowiak, Diffuse Phase Transitions in Thick Ferroelectric Ba(Ti<sub>x</sub>Sn<sub>1-x</sub>)O<sub>3</sub> Films of Perovskite-Type Structure, *Thin Solid Films*, **69**, 339-345 (1980).
52. A. A. Gitel'son, A. M. Lerer, V. S. Mikhalevskii, V. M. Mukhortov, and S. V. Orlov, Physical Properties of (Ba, Sr)TiO<sub>3</sub> Ferroelectric Thin Films in Weak Electric Fields, *Sov. Phys. Solid State*, **19**(7), 1121-1124 (1977).

# **SPECTROSCOPIC ELLIPSOMETRY**

**APPENDIX 32**

**The Pennsylvania State University**  
**The Graduate School**

**SPECTROSCOPIC ELLIPSOMETRY OF INTERFACES**

**A Thesis in**  
**Physics**

**by**  
**Nhan Van Nguyen**

**Submitted in Partial Fulfillment**  
**of the Requirements**  
**for the Degree of**

**Doctor of Philosophy**

**November 1989**

## ABSTRACT

Spectroscopic ellipsometry is shown in this study to have the capability (i) to characterize damaged structure, (ii) to determine the composition and structure of nonstoichiometric compounds, (iii) to follow the evolution of interfaces and recrystallization process on heat treatment, and (iv) to detect extremely thin layer and/or transitional region between different layers.

In the case of c-Si implanted with carbon ions the regression analysis of SE data was shown to be able to distinguish the chemical mixture of silicon and implanted carbon against the physical mixture of silicon and silicon carbide. The recrystallization of Si and the formation of crystalline silicon carbide on annealing at high temperature were investigated.

Virgin and germanium implanted crystalline silicon samples oxidized at high temperatures were examined. The interposing layer between the oxide and the silicon substrate was found to be composed of a thin layer of crystalline germanium-silicon alloy  $\text{Ge}_x\text{Si}_{1-x}$  with the composition  $x$  accurately determined. A brief discussion on the strain and quantum confinement of the interface is also presented. The interface thickness is in excellent agreement with that obtained by compared to that obtained by high-resolution transmission electron microscopy. It is shown that the composition and not the thickness of the interface layer of  $\text{Ge}_x\text{Si}_{1-x}$  alloy is responsible for the enhancement of the oxidation rate of  $\text{Ge}^+$ -implanted c-Si

The single crystal silicon samples implanted with oxygen ions were analyzed. In the as-implanted state, the thickness and the understoichiometric oxide compound  $\text{SiO}_x$  formed in each layer were determined. The oxygen concentration oxygen is compared with the theoretically expected value. On high temperature annealing  $\text{SiO}_2$  is formed and

the damaged silicon gets annealed resulting in epitaxially grown c-Si from the substrate. SiO<sub>2</sub> was seen to redistribute on high temperature annealing, which was also confirmed by Rutherford Backscattering technique.

Depth profiling of silicon monoxide film on vitreous silica reveals the inhomogeneity of the oxygen concentration in the film. The composition x in the nonstoichiometric silicon oxide SiO<sub>x</sub> and the thickness of each layer of the film were determined. Such a nonstoichiometric compound was also observed at the interface between c-Si and its thick thermal oxide layer using the anti-S reflection technique. The result shows that this transitional region is  $10 \pm 0.9$  Å thick and composed of SiO<sub>0.9±0.1</sub>.

**APPENDIX 33**

The Pennsylvania State University  
The Graduate School

CHARACTERIZATION OF INHOMOGENEOUS  
TRANSPARENT THIN FILMS ON TRANSPARENT SUBSTRATES  
BY SPECTROSCOPIC ELLIPSOMETRY

A Thesis in  
Physics  
by  
Pongpan Chindaoum

Submitted in Partial Fulfillment  
of the Requirements  
for the Degree of

Doctor of Philosophy  
August 1991

## ABSTRACT

Inhomogeneities in dielectric thin films are known to be responsible for irreproducibilities in the film properties. Therefore any effective method for characterizing the films (i.e. determining the true optical properties) must account for the film inhomogeneity. The common technique used in the determination of the refractive index and thickness of transparent films is spectrophotometry (RT), where the absolute intensity of reflected and/or transmitted light is measured. However those measurements are not sensitive to heterogeneities, so workers have been forced to ignore them, or in the best case, to assume that the inhomogeneity varies linearly with the film thickness.

Spectroscopic ellipsometry (SE) has also been used as a nondestructive technique for determining the optical properties and structure of thin films. In contrast to RT, SE is capable of measuring simultaneously the amplitude and the phase of the reflected light. Since the phase parameter is extremely sensitive to very thin layers and to the film microstructure, SE is obviously more suitable for studying inhomogeneous films. Unfortunately, when a transparent sample is measured, SE suffers a serious drawback due to the lack of sensitivity inherent in the basic design of the instrument. Therefore, up till now, SE has been used primarily to study metallic or

semiconducting films where the optimum conditions are typically satisfied.

In this thesis, a novel method of incorporating an achromatic compensator into a rotating-analyzer ellipsometer to solve this problem is proposed and tested for its reliability. As a result, for the first time, the refractive index of vitreous silica measured by SE matches the reference data to within 0.001 over a wide spectral range (300-700 nm). More importantly, because of the improved accuracy of data taken with the achromatic compensator, the sensitivity of SE to the extinction coefficient can also be estimated to the third decimal place.

After gaining confidence in the accuracy of our experimental data on transparent samples, a number of fluoride and oxide optical coatings on vitreous silica substrates were studied. In every case, the best-fit models for these films reveal inhomogeneities (such as surface microroughness, incorporated voids and void distributions) which are consistent with the well-known columnar thin film growth morphology. In addition, these models provide quantitative results on the refractive index as a function of wavelength and the thickness as well as the void fraction of each optical sublayer. Since the film inhomogeneity has been accounted for, the evaluated optical properties should represent those of the true film materials. As a result, the index of refraction and its dispersion in the near UV and visible region are reported for several optical coating materials ( $\text{AlF}_3$ ,  $\text{CeF}_3$ ,  $\text{HfF}_4$ ,  $\text{LaF}_3$ ,  $\text{ScF}_3$ ,  $\text{Al}_2\text{O}_3$ ,  $\text{ThO}_2$ ,  $\text{HfO}_2$ ,  $\text{Sc}_2\text{O}_3$ ,  $\text{Y}_2\text{O}_3$  and  $\text{ZrO}_2$ ). The

multi-material approach in this study has also resulted in a moderate success in identifying correlations between the inhomogeneity and the coating material.

In addition to this work, the usefulness of SE for characterizing ferroelectric thin films is demonstrated. Using SE depth profiling analysis, thin films of  $\text{BaTiO}_3$  on single crystal  $\text{SrTiO}_3$  are shown to be very inhomogeneous. These inhomogeneities may explain the anomalous electrical properties observed in independent measurements.

**APPENDIX 34**

# Characterization of the interface between Ge<sup>+</sup>-implanted crystalline silicon and its thermally grown oxide by spectroscopic ellipsometry

N. V. Nguyen and K. Vedam

Materials Research Laboratory and Department of Physics, The Pennsylvania State University, University Park, Pennsylvania 16802

J. Narayan

Department of Materials Science and Engineering, North Carolina State University, Raleigh, North Carolina 27695-7916

(Received 22 August 1989; accepted for publication 10 October 1989)

Using spectroscopic ellipsometry we have studied a series of virgin and germanium-implanted crystalline silicon samples oxidized at 900 and 1000 °C. The thickness of the oxide in the virgin and implanted sample was accurately determined and found to be in agreement with the results previously obtained by single-wavelength ellipsometry. The interface structure between the silicon substrate and the oxide layer of all the samples was investigated in detail. We find that the interposing layer between the oxide and the silicon substrate is composed of a thin layer of crystalline germanium-silicon alloy. A brief discussion on the strain and quantum confinement of the interface that may affect the calculated composition is also presented. The interface thickness was found to be slightly larger to that obtained by high-resolution transmission electron microscopy measurement for samples implanted at higher doses. A plausible explanation for the discrepancy is provided.

## INTRODUCTION

Recently it has been shown that implantation of germanium ions into crystalline silicon (*c*-Si) enhances the oxidation of silicon.<sup>1</sup> During the oxidation process, a layer of germanium-silicon alloy is formed at the interface between the oxide and the silicon substrate as a result of the limited solid solubility of Ge in SiO<sub>2</sub> and the slow diffusivity of germanium in silicon compared with the oxidation rate. The enhancement of oxidation has been explained as a result of the reduction of binding energy of Si atoms at the interface between silicon and the oxide. Recently, Srivatsa *et al.*<sup>2</sup> have further investigated the nature of interfaces and oxidation processes of a series of germanium-implanted silicon with varying doses of germanium. In their studies, they employed Rutherford backscattering spectrometry (RBS), high-resolution transmission electron microscopy (HTEM), and a single-wavelength ellipsometer (SWE) to examine the thickness as well as the smoothness of the interfaces between the *c*-Si substrate and the oxide layer, and to correlate with oxidation conditions. Furthermore a model describing the enhancement of oxidation and the process of segregation of germanium at the interface was proposed in their report. With such characterization tools, however, they have been able to detect the thickness, but not the composition of germanium-silicon alloy at the interface. In order to further the understanding of the detailed mechanism of the oxidation process, the exact composition of the germanium-silicon alloy at the interface must be determined. Therefore, in this article, the same set of the samples mentioned above are reexamined using spectroscopic ellipsometry (SE) technique. SE is known as a nondestructive and nonperturbing technique to characterize thickness and structure, as well as composition of interfaces, with a sensitivity to the monolayer level.<sup>3</sup> In this article we show that this technique has enabled us to detect the finite interface between the silicon

substrate and the SiO<sub>2</sub> overlayer on it in the Ge<sup>+</sup>-implanted samples and also that it is a crystalline germanium-silicon alloy with the chemical composition accurately determined. In the process of analyzing SE data, we also exclude a number of other possible compositions of the interface such as a thin layer of pure germanium or a physical mixture of clustered crystalline Ge(*c*-Ge) and crystalline (*c*-Si). Furthermore, the oxide thickness on the virgin and implanted samples are determined to a higher degree of confidence and found to be consistent with the results of Srivatsa *et al.*

## EXPERIMENT

The single-crystal silicon (1–15 Ω cm) substrates with (100) orientation were implanted with singly charged Ge ions at 35 keV at several doses as summarized in Table I. These samples were oxidized in a tube furnace in a steam ambient with one set at 900 °C for 30 min and the other at 1000 °C for 20 min. The thickness of oxide on the virgin and implanted samples was measured by a single-wavelength ellipsometer (SWE). The thicknesses of the interface layer between the *c*-Si substrate and the oxide for the implanted samples were determined by high-resolution TEM. The implant dose of Ge ions was obtained by RBS. All of these measurements were previously reported by Srivatsa *et al.* In this article, we reproduce some of their results for comparison with our results.

The SE data for each sample were obtained in the photon energy range from 1.5 to 5.0 eV with 0.02-eV increments with an automatic rotating polarizer ellipsometer described in detail elsewhere.<sup>4</sup> The actual measured parameters are  $\alpha$  and  $\beta$ , which are the second order Fourier coefficients of the intensity of light arriving at the detector of the ellipsometer. From these coefficients, one can easily calculate the ellipsometric parameters  $\tan \Psi$  and  $\cos \Delta$ , which are the amplitude and phase of the complex reflectance ratio

TABLE I. Summary of results from spectroscopic ellipsometry (SE), HTEM, RBS, and single-wavelength ellipsometry (SWE) for the virgin and implanted samples.

Sample		Measure of implanted dose (RBS) $\times 10^{16}/\text{cm}^2$	Oxide thickness ( $\text{\AA}$ )				Interface			$\sigma$	
			Virgin		Implanted		Thickness ( $\text{\AA}$ )		Composition	Virgin	Implanted
Label No.	Oxidation		SE	SWE	SE	SWE	SE	HTEM	Ge, Si, ...		
2	910 °C 30 min	0.5	1363 $\pm$ 1	1300	2254 $\pm$ 1	2130	14 $\pm$ 1	12	$x = 0.48 \pm 0.02$	0.012	0.016
3		0.86	1160 $\pm$ 1	1130	1857 $\pm$ 1	1850	29 $\pm$ 2	29	$x = 0.50 \pm 0.02$	0.014	0.028
5		3.15	1037 $\pm$ 1	1040	1740 $\pm$ 2	1760	106 $\pm$ 9	95	$x = 0.51 \pm 0.02$	0.016	0.043
7	1000 °C 20 min	0.485	1976 $\pm$ 1	1980	2396 $\pm$ 1	2440	18 $\pm$ 2	14	$x = 0.37 \pm 0.03$	0.016	0.017
8		0.91	2003 $\pm$ 1	2000	2476 $\pm$ 1	2470	29 $\pm$ 4	32	$x = 0.43 \pm 0.03$	0.017	0.024
9		3.35	1976 $\pm$ 1	1950	2514 $\pm$ 2	2490	142 $\pm$ 10	95	$x = 0.44 \pm 0.02$	0.017	0.033

$\bar{\rho} = \bar{r}_p/\bar{r}_s \equiv \tan \psi e^{i\Delta}$ , where  $\bar{r}_p$  and  $\bar{r}_s$  are the complex reflectances of *p*- and *s*-polarized lights, respectively. In the following data analysis, a realistic model characterizing each sample has to be objectively constructed so as to reproduce measured data. The wavelength-independent quantities, such as the thickness and composition of the various layers in the model, are determined by minimizing the unbiased estimator ( $\sigma$ ), which is the difference between the measured data and the modeled data, using least-squares method and linear regression analysis (LRA). The uncertainties of these quantities are also obtained with a 90% confidence limit. Throughout this article, for want of space only the spectrum of  $\cos \Delta$  as a function of photon energy is presented.

## RESULTS AND DISCUSSION

To analyze the measured data, we used a three-phase (ambient/oxide layer/*c*-Si substrate) model for the virgin samples, and a four-phase (ambient/oxide layer/interface/*c*-Si substrate) model for the implanted ones. In the virgin samples, the determination of the oxide thicknesses is simple and straightforward, therefore, need not be discussed further. On the other hand, since the interface between the *c*-Si substrate and the oxide in the implanted samples is expected to be nonstoichiometric, a thorough examination must be taken to accurately determine the characteristics of this interface. In the following presentation, to avoid repetition in our description, we concentrate only on sample No. 8 in discussing the analysis though the results of similar analyses on all the samples are included.

If the three-phase model without a finite interface between the oxide layer and the *c*-Si substrate is considered for the implanted specimen, the calculated data using such a model shows a large discrepancy in the photon energy region of about 2.0–3.4 eV, as clearly displayed in Fig. 1. Such a deviation implies that the optical behavior of the interface is different from those of *c*-Si substrate and SiO<sub>2</sub> mainly in this particular spectral range. Therefore, in the modeling process we considered *c*-Ge, amorphous Ge (*a*-Ge), amorphous Si (*a*-Si), a physical mixture of clustered *c*-Ge and *c*-Si, and crystalline germanium-silicon alloy for the interposing interface layer. The reasons for using these materials for a model fit can be seen in the subsequent data analysis because the resulting modeled spectra show the main effect in the spec-

tral range of 2.0–3.4 eV, as mentioned above, and an unnoticeable change in the remaining spectral region. For instance, in sample No. 8, if the interface is considered as a pure crystalline germanium layer, the best fit from the LRA analysis for this particular model gives an oxide of 2474  $\pm$  2  $\text{\AA}$  thick and a pure crystalline germanium of 6  $\pm$  1  $\text{\AA}$  thick that is inconsistent with the HTEM result (32  $\text{\AA}$ ) reported by Srivatsa *et al.* (see Table I). Furthermore the fitting between the modeled spectra and the experimentally measured data does not agree well in the spectral region 2–3.4 eV as can be seen from Fig. 1, and in addition the unbiased estimator of 0.040 is also fairly large. Consequently we can rule out this model that treats the interface as made up of pure crystalline germanium. Next we considered the case in which the interface is a thin layer of clustered *c*-Ge physically mixed<sup>3</sup> with *c*-Si. Again, similar to the previous case, this model resulted in an unacceptable value for the unbiased estimator  $\sigma = 0.040$ . The fitting of the corresponding modeled data is also poor and visibly similar to Fig. 1. In addition it yields an unreasonable 90% confidence limits in both thickness (23  $\pm$  38  $\text{\AA}$ ) and fraction of the composition (*c*-Si mixed

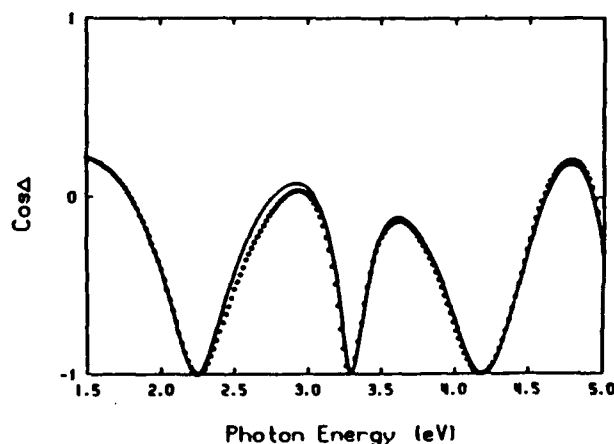


FIG. 1. Comparison of the measured (dots) and the calculated (solid line) spectra for sample No. 8 for the following models: (a) SiO<sub>2</sub>/*c*-Si without interface layer, (b) SiO<sub>2</sub>/interface of *c*-Ge/*c*-Si, and (c) SiO<sub>2</sub>/interface (which is a physical mixture of *c*-Ge and *c*-Si)/*c*-Si. Since all these three models yield almost identical graphs, only one is presented here.

with  $0.06 \pm 0.47\%$  of  $c$ -Ge) of the interface. It should be mentioned that we attempted to interpret this interface as either  $a$ -Ge or  $a$ -Si or as a physical mixture of  $a$ -Si and  $a$ -Ge (not shown) and all of these models failed to reproduce the measured spectrum. Finally, as clearly seen in Fig. 2 for the implanted sample No. 8, the modeled data fits the measured data extremely well when the interface is modeled with a thin  $29 \pm 2$ -Å-thick layer of crystalline germanium-silicon alloy of composition  $\text{Ge}_{0.43}\text{Si}_{0.57 \pm 0.03}$ . In all the models described above, the input data are the dielectric spectrum of  $c$ -Si and  $c$ -Ge published by Aspnes,<sup>5</sup> and that of  $\text{SiO}_2$  obtained from Malitson's analytic dispersion relation<sup>6</sup> for vitreous silica. The dielectric function of  $\text{Ge}_x\text{Si}_{1-x}$ , whose imaginary part is shown in Fig. 3, has been recently measured by Humlicek *et al.*<sup>7</sup> for various compositions  $x$  from 1 to 0, using the SE technique. To determine the exact alloy composition of the interface, however, we must know the dielectric function for that composition. By using the harmonic oscillator approximation (HOA)<sup>8,9</sup> to represent the dielectric function of  $\text{Ge}_x\text{Si}_{1-x}$  as a sum of the contributions from seven oscillators, we were able to fit all of the measured spectrum of Humlicek *et al.* and the fitted parameters of the seven oscillators are then generalized for any  $x$  to obtain the dielectric function of  $\text{Ge}_x\text{Si}_{1-x}$ . This generalized dielectric function is then incorporated into our modeling and LRA program to allow for the variation of value of  $x$  to fit the measured data. The results of similar studies on other samples both virgin and implanted are summarized in Table I.

It is seen that the thickness of oxide on the virgin and implanted samples obtained by our SE technique is in good agreement with the results reported by Srivatsa *et al.* as shown in Table I. Since the correlations between implanted doses of Ge, oxidation conditions, oxide thickness of virgin and implanted samples, and enhanced oxidation phenomenon have been already described in detail by Srivatsa *et al.*, we focus our discussion only on the thickness and composition of the interposing interface layer. Referring to Table I and Fig. 4, we find that the thickness of the interface obtained by our SE measurement agrees well with that obtained by HTEM for most samples except for those with

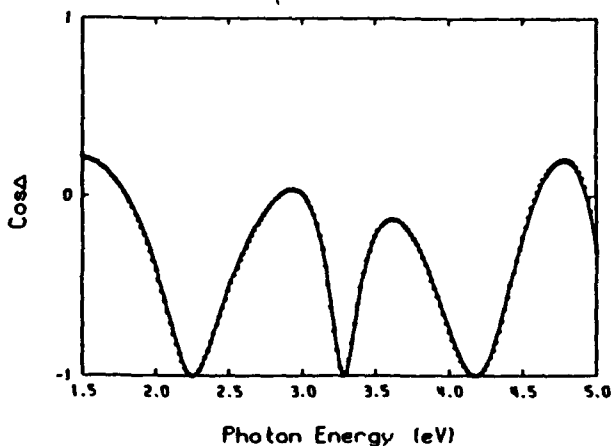


FIG. 2. Comparison of the measured spectrum (dots) with that for the model  $\text{SiO}_2/\text{interface}/c\text{-Si}$  (solid line) for sample No. 8. The interface is crystalline germanium-silicon alloy  $\text{Ge}_x\text{Si}_{1-x}$ ,  $x = 0.43 \pm 0.03$ .

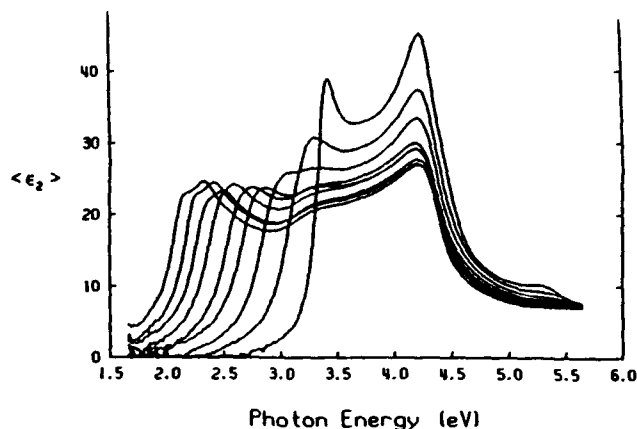


FIG. 3. The imaginary part of the pseudodielectric function ( $\epsilon$ ) of crystalline  $\text{Ge}_x\text{Si}_{1-x}$  alloys for  $x = 0.00, 0.218, 0.389, 0.513, 0.635, 0.750, 0.831, 0.914,$  and  $1.000$ . The value of  $x$  decreases from left to right (after Ref. 7).

higher implant doses, namely, samples No. 5 and 9, which were implanted to a dose of  $3.15 \times 10^{16}$  and  $3.35 \times 10^{16}/\text{cm}^2$ , respectively. The interface thicknesses of these two particular samples obtained by SE are larger than those of the HTEM measurement. This discrepancy can be easily explained if we reexamine the cross-section electron micrograph (Fig. 4 in the report of Srivatsa *et al.*) for sample No. 5, which shows a large degree of roughness at the  $\text{Si}/\text{Ge}_x\text{Si}_{1-x}$  interface. It should be pointed out that the SE measurement was done on an area of about  $1 \times 3 \text{ mm}^2$  of the sample surface, therefore, the SE measured thickness is an average on that area whereas HTEM thickness was estimated from a region much less than a  $\mu\text{m}$  in length. Moreover, the large uncertainty of SE interface thickness (see Table I) for the samples compared with the other ones of lower doses (samples No. 2,3,7,8) seems to correlate with the roughness mentioned above since, in the modeling formalism, an interface between layers is assumed to be extremely sharp.

Srivatsa *et al.* used Rutherford backscattering spec-

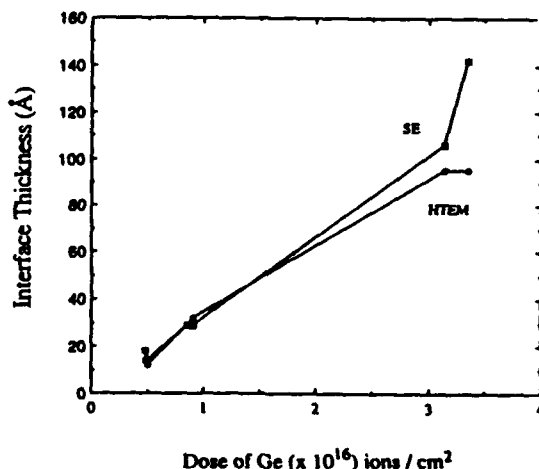


FIG. 4. Plot of the interface thickness obtained by SE and HTEM. The Ge ion dose was measured by RBS (Ref. 2).

trometry to determine the implanted doses or the total number of germanium per unit area and thicknesses of SiO<sub>2</sub> oxide layers (see Table I). If one assumes that all this germanium is concentrated at the interface, one can calculate the "estimated" thickness of this pure germanium layer, as was done by Srivatsa *et al.* A comparison of this "estimated" thickness with that obtained by HTEM (see Table I) may suggest that the interface is germanium rich. However, from our SE measurements (composition column in Table I), we find that the interface of all the samples is a crystalline germanium silicon alloy Ge<sub>x</sub>Si<sub>1-x</sub> with composition  $x$  in the range from 0.34 to 0.51. Thus our result indicates the interface is instead slightly silicon rich. This statement can be supported by the accuracy (confidence level) in determining the composition. It has been known that linear regression analysis used in SE not only systematically provides the best-fit parameters such as thickness and composition, but also establishes correlations and 90% confidence levels as to show which parameters are well determined by the data.<sup>10</sup> As evident in Table I, the composition of the germanium silicon alloy at the interface for all the samples has a very high confidence level, i.e., a small uncertainty, and thus a high degree of accuracy. Furthermore, since the composition of the crystalline germanium-silicon alloys is extremely sensitive to the energy position of optical transition  $E_1$ , the generalized dielectric function of the alloy discussed above allows our modeling program to adjust the energy position of  $E_1$  to fit the measured spectra and thus accurately deduce the composition of the interface for each sample.

At this juncture, it is necessary to consider the effect of strain in a strained layer epitaxial interface. According to Bean *et al.*,<sup>11</sup> the lattice mismatch of  $c$ -Ge<sub>x</sub>Si<sub>1-x</sub> with respect to that of (100)  $c$ -Si can be accounted for by lattice strain if the thickness of the Si-Ge alloy layer is less than a critical value, which depends on the alloy composition. In such cases, the lattice parameters parallel to the interface are equal and the growth of the epitaxial layers are commensurate (i.e., there are no misfit dislocations at the interface). Bean *et al.* found that for the case of Ge<sub>0.5</sub>Si<sub>0.5</sub> the critical thickness is 100 Å and the strain amounts to about 2%. In our experiment, since the thickness of the Si-Ge alloy layers are less than 100 Å and the alloy composition range is from 0.4 to 0.5, one would expect such strained layer epitaxial growth in our samples with the strain of the order of 2%. In our SE studies thus far we have used the dielectric function data of Humlicek *et al.* obtained on strain-free bulk alloys. In other words, we have not taken the effect of this strain due to lattice mismatch in our calculations. As a first approximation, such a neglect of the strain is not expected to cause serious problems for the following reasons. From Fig. 3 it is seen that even a slight variation of  $x$  in the alloy composition causes a significant shift of the  $E_1$  energy position. The effect of introducing tetragonality (commensurate) in the  $c$ -SiGe alloy will be to split each of the  $E_1$  and  $E_2$  peaks into two components corresponding to light polarized parallel and perpendicular to the interface. Since such splitting is usually an order of magnitude less than the large shift of the peak position observed by varying  $x$  by 0.1, the results obtained by neglecting the strain effect should be minimal. In fact, using

electroreflectance spectroscopy Pearsall *et al.*<sup>12</sup> have experimentally and theoretically investigated the strain effects on Si-Ge<sub>x</sub>Si<sub>1-x</sub> multiple quantum-well structures and found that for the case of a 75-Å-thick layer of Ge<sub>0.45</sub>Si<sub>0.55</sub> sandwiched between 274-Å-thick layers of  $c$ -Si, a shift of 0.02 eV in the  $E_1$  position was observed due to the strain. With this 0.02-eV shift in  $E_1$ , using the  $E_1$  vs  $x$  relationship obtained by Humlicek *et al.*, we find that it corresponds to a shift in our modeled composition of about 0.02, which is still within the uncertainty of the evaluated composition ( $\pm 0.02$ , see Table I). Hence we believe the neglect of tetragonality of the Ge<sub>x</sub>Si<sub>1-x</sub> alloy interface should not cause significant error in the evaluation of the value of "x" and in the thickness of the interface determined by the SE technique. Despite this, it may still be possible to detect the effect of tetragonality by the variable angle-of-incidence SE technique, and such experiments are in progress to detect and characterize it. In closing, it is also worth mentioning the influence of quantum-well confinement. Since a low band-gap crystalline Ge<sub>x</sub>Si<sub>1-x</sub> thin layer is sandwiched between the oxide and crystalline silicon substrate that have higher band gaps, the optical transitions of the interface may shift upward due to the effect of spatial confinement of both electrons and holes. Again as shown by Pearsall *et al.*, this effect is negligible for the  $E_1$  position, thereby, the alloy composition values evaluated for our samples are probably not affected by the quantum-well confinement.

## CONCLUSION

The technique of spectroscopic ellipsometry (SE) technique has been employed to characterize a series of virgin and germanium-implanted  $c$ -Si samples oxidized at 900 and 1000 °C. The oxide thickness on both the virgin and implanted set was found to be consistent with that previously obtained by a single-wavelength ellipsometer. In this study we have demonstrated the ability of SE to measure the thickness as well as determine the exact chemical composition of a monolayer thick interface buried under the thick oxide overlayer. Specifically, the interface between the  $c$ -Si substrate and the oxide overlayer in the implanted sample was found to be a crystalline germanium-silicon alloy Ge<sub>x</sub>Si<sub>1-x</sub> with the composition  $x$  in the range from 0.37 to 0.51, i.e., slightly silicon rich. The interface thickness by SE is in good agreement with the results obtained by HTEM except for two samples implanted with higher doses. For these specimens, the thicknesses determined by SE are larger than those measured by HTEM. The disagreement can be accounted for by the degree of roughness at the interface between the Ge<sub>x</sub>Si<sub>1-x</sub> layer and the  $c$ -Si substrate, which was observed to increase with a higher implantation dose. The effect of strain and quantum confinement on the optical transition  $E_1$  and, thus, on the interface composition obtained from SE analysis was shown to be negligible.

## ACKNOWLEDGMENTS

The authors wish to thank Professor R. W. Collins for many valuable discussions. This research work was supported by DARPA/ONR, project No. N00014-86-K-0767. The

authors would also like to thank Dr. Humlicek of the University of Purkyne for sending us his results prior to publication. One of us (J.N.) was partially supported by the National Science Foundation-Engineering Center Programs through the NCSU Center for Advanced Electronic Materials Processing (Grant No. CDR-8721505).

<sup>1</sup>O. W. Holland, C. W. White, and D. Fathy, *Appl. Phys. Lett.* **51**, 520 (1987); D. Fathy, O. W. Holland, and C. W. White, *Appl. Phys. Lett.* **51**, 1337 (1987).

<sup>2</sup>A. R. Srivatsa, S. Sharan, O. W. Holland, and J. Narayan, *J. Appl. Phys.* **65**, 4028 (1989).

<sup>3</sup>D. E. Aspnes and J. B. Theeten, *Phys. Rev. Lett.* **43**, 1046 (1979).

<sup>4</sup>K. Vedam, S. Y. Kim, L. D'Aries, and A. H. Guenther, *Opt. Lett.* **12**, 456 (1987); N. V. Nguyen, 1989 Ph.D. thesis, Pennsylvania State University (unpublished).

<sup>5</sup>D. E. Aspnes and A. A. Studna, *Phys. Rev. B* **27**, 985 (1983).

<sup>6</sup>L. H. Malitson, *J. Opt. Soc. Am.* **55**, 1205 (1965).

<sup>7</sup>J. Humlicek, M. Garriga, M. I. Alonsos, and M. Cardona, *J. Appl. Phys.* **65**, 2827 (1989).

<sup>8</sup>G. F. Feng and R. Zallen, *Phys. Rev. B* **40**, 1064 (1989).

<sup>9</sup>M. Erman, J. B. Theeten, P. Frijlink, S. Gaillard, F. J. Iffia and C. Alibert, *J. Appl. Phys.* **56**, 3741 (1984).

<sup>10</sup>D. E. Aspnes, J. B. Theeten, and R. P. H. Chang, *J. Vac. Sci. Technol.* **16**, 1374 (1979).

<sup>11</sup>J. C. Bean, L. C. Feldman, A. T. Kiory, S. Nakahara, and I. K. Robinson, *J. Vac. Sci. Technol.* **2**, 436 (1984).

<sup>12</sup>T. P. Pearsall, F. H. Pollak, J. C. Ean, and R. Hull, *Phys. Rev. B* **33**, 6821 (1986).

**APPENDIX 35**

SPECTROSCOPIC ELLIPSOMETRY STUDIES ON ION BEAM SPUTTER DEPOSITED  
Pb(Zr,Ti)O<sub>3</sub> FILMS ON SAPPHIRE AND PT-COATED SILICON SUBSTRATES

S. Trolier-McKinstry, H. Hu, S. B. Krupanidhi,  
P. Chindaudom\*, K. Vedam, and R. E. Newnham

Materials Research Laboratory  
The Pennsylvania State University  
University Park, PA 16802

\*P Chindaudom is now with NECTECH, Ministry of Science, Bangkok, Thailand

**Abstract**

Spectroscopic ellipsometry has been utilized to non-destructively depth profile multi-ion-beam reactively sputtered lead zirconate titanate films. Some degree of inhomogeneity (in the form of low density layers or surface roughness) was found in all of the films examined. The evolution in the structure and microstructure of such films during post-deposition annealing was investigated with *in-situ* spectroscopic ellipsometry. It was found that the onset of microstructural inhomogeneities was associated with the crystallization of the perovskite phase, and that the final film microstructure was dependent on the details of the annealing process.

A model was developed to approximate the effect that local density variations play in determining the net electrical properties of ferroelectric films. Depending on the configuration of the embedded porosity, it was demonstrated that microstructural inhomogeneities can significantly change the net dielectric constant, coercive field, and remanent polarization of ferroelectric films. It has also been shown that low density regions near the film/substrate interface can result in apparent size effects in ferroelectric films.

## Introduction

Ferroelectric thin films are potentially useful as pyroelectric sensors, ferroelectric memory elements, electrooptic switches, and miniature electromechanical transducers. For these applications, high quality films with reproducible electrical, optical, and electromechanical properties are required. Several growth techniques have emerged in the recent past for the deposition of multi-cation oxide films. In all cases, the final properties seem to be closely connected to the nature of the deposition process [1]. For this study, multi-ion-beam reactive sputtering (MIBERS) was chosen for the growth of optical quality perovskite films. Films for optical applications should have a uniform smooth surface, should be free from defects or inclusions, and should possess minimal absorption and low scattering over the wavelengths of interest. With the MIBERS technique the composition, microstructure, and physical morphology of the films can be controlled by careful choice of the growth conditions [2,3].

Unfortunately, as is the case for transparent films used in optical coatings, non-destructive characterization of the film (including any variations in the microstructure with depth in the sample) has in the past been difficult to perform. To alleviate this problem, this paper describes spectroscopic ellipsometry (SE) as a non-destructive, non-invasive tool for depth profiling ferroelectric thin films on both transparent and absorbing substrates.

The success of SE for depth-profiling samples was demonstrated in the 1970's (e. g. [4]). Following the initial demonstration, careful studies were undertaken to demonstrate that the SE results are consistent with other characterization tools [5-8]. SE has since become widely used for characterizing thin film systems where at least one component is strongly absorbing. Transfer of the process to either monolithic transparent samples or transparent films on transparent substrates, however, has been hindered by inherent difficulties in obtaining accurate SE data for such samples. This difficulty has recently been overcome via the development of a series of systematic

calibrations for a rotating analyzer spectroscopic ellipsometer [9,10]. The information derived from this technique is particularly useful in correlating the role of the processing procedure in controlling the physical structure and net electrical properties of ferroelectric thin films.

### Film Preparation

Pb(Zr,Ti)O<sub>3</sub> (PZT) films with a Zr/Ti ratio of about 50/50 were deposited by multi-ion-beam reactive sputtering [2]. This technique, as established earlier, offers a highly controllable, reproducible deposition process with excellent uniformity in composition and thickness for large surface area samples. As substrates for the deposition of oriented films, both (1 $\bar{1}$ 02) and (0001) sapphire were used (One side polished, Union Carbide). The interest in (1 $\bar{1}$ 02) sapphire stems from the fact that this orientation can be grown epitaxially on silicon, leading to the possibility of integrating a PZT electrooptic component on to a silicon substrate prepared with a sapphire intermediate layer [11]. In addition, platinum-coated silicon wafers were also utilized as substrates for some films. These latter substrates had a thick SiO<sub>2</sub> barrier layer to prevent reaction between platinum and silicon at elevated temperatures, and a thin Ti film between the SiO<sub>2</sub> and Pt to improve adhesion.

The depositions were carried out on unheated substrates without low energy ion assistance. It was observed that the substrate temperature rose to about 100°C during deposition due to intrinsic bombardment by the sputtered species. While the films on sapphire were deposited with a Pb content very close to the stoichiometric composition of the perovskite phase, the films on Pt-coated silicon were deposited with 3 - 6% excess Pb to promote crystallization of the correct phase on annealing [2]. Some films were reserved for *in-situ* ellipsometric studies. The remaining films were heated *ex-situ* at 10°C/min to 650°C and soaked at this temperature for 2 hrs. This procedure yields well-crystallized perovskite films. All films deposited on sapphire showed highly

oriented X-ray diffraction patterns after annealing. Films on  $(\bar{1}\bar{1}02)$  substrates, as seen in Fig. 1, were almost exclusively (101) oriented. Similarly, with (0001) substrates, the films were also (101) orientated, although to a lesser degree. Films on Pt-coated silicon had a random polycrystalline orientation. Ferroelectricity was established by measuring hysteresis loops for the films on Pt-coated silicon substrates.

### Ellipsometer configuration and calibration

A schematic of the rotating-analyzer spectroscopic ellipsometer used in these experiments is shown in Figure 2. In addition to standard calibrations to eliminate first order errors in the optics [12], two additional steps were required to achieve accurate data for transparent samples. First, the problem of detector non-linearity was minimized by calibrating the polarization detection system both for the presence of ambient light and for variations in the gain of ac and dc components of the signal with changes in the overall signal level [13]. Secondly, inherent difficulties in accurately measuring the near  $0^\circ$  (or  $180^\circ$ ) phase change on reflection from a transparent sample [14] were overcome through the use of an achromatic compensator.

In contrast to the standard Babinet-Soleil compensator, the three-reflection achromatic compensator [15] used in these experiments produces approximately a  $90^\circ$  phase retardation for all wavelengths between 300 and 800 nm. To correct for the remaining wavelength dependent errors introduced by the compensator, a two-measurement, "effective source" calibration was utilized. With this technique, the polarization state of the light emerging from the compensator is first measured at each wavelength with the ellipsometer detection arm in the straight-through position. Then, the sample is aligned at the desired angle of incidence and measured over the same wavelength range to obtain a spectrum containing lumped information on the sample properties and the source polarization. The change in the light polarization due to reflection from the sample itself, the quantity of interest, can then be calculated.

With these calibrations in place, the ellipsometric parameters  $\Delta$  and  $\Psi$  can be measured for transparent samples to within  $0.03^\circ$  and  $0.01^\circ$ , respectively, over the spectral range 300 - 800 nm. This corresponds to an accuracy in the real and imaginary parts of the refractive index of 0.001 [9,13] for a bulk specimen of vitreous silica [16]. As shown in Figure 3, this is an order of magnitude improvement over the accuracy which can be obtained without these data correction procedures. It should be noted that the additional procedures utilized constitute a calibration of the polarization detection system, and as such are sample independent.

Measurements made as a function of temperature were performed in a windowless electrical resistance furnace. As shown in Figure 4, a kanthal-wire wrapped alumina tube was used as the heat source. The temperature was monitored by a thermocouple placed within half an inch of the sample, and controlled by computer. The outer shell of the chamber consisted of a capped, monolithic brass cylinder machined with two  $1/2"$  x  $1/4"$  holes for the entrance and exit beams. Both the cylinder and the baseplate were subsequently electroplated with nickel to minimize oxidation of the copper and vaporization of the zinc at elevated temperatures. Because the chamber is windowless, no additional corrections for the ellipsometer optics were required.

### Experimental Procedure

Measurements were made on films on sapphire substrates at an incidence angle of  $80^\circ$  using the compensator and the effective source calibration described above. For films on Pt-coated Si, measurements were performed at an angle of incidence of  $70^\circ$  without the compensator. SE data were collected both on films which had been annealed at  $650^\circ\text{C}$  for 2 hours and on as-deposited films which were heat-treated *in-situ* in the ellipsometer. For the *in-situ* experiments, data were taken at different annealing temperatures in  $50^\circ\text{C}$  intervals between 25 and  $600^\circ\text{C}$ . Between room temperature and  $350^\circ\text{C}$ , data were collected at the annealing temperature. Above  $400^\circ\text{C}$ , however, the

film was heated to the desired temperature, soaked for half an hour, and cooled below 300°C for measurement to eliminate errors associated with glow from the furnace. In all cases, the film was heated to the previous annealing temperature at 5°C/min, and then raised from there to the new annealing temperature at 2°C/min. Cooling was done at 5°C/min until the furnace could no longer follow. After this treatment, the same film was annealed in a conventional furnace at 650°C for 2 hr in order to match the maximum annealing temperature experienced by the *ex-situ* annealed samples. Following data collection, the SE data were modelled in order to analyze the film thickness, optical properties and the degree of inhomogeneity present within the film.

Modelling of the experimental data was done under the assumption of planar interfaces between layers with all layers parallel to the surface of the film. Inhomogeneities in the film density were described by subdividing the film into a series of layers with different volume fractions of air present in each. Bruggeman effective medium theory was used to calculate the effective dielectric functions of two phase mixtures. Variables in the fitting procedure included all of the layer thicknesses, the volume fraction of air present at any depth in the film, and the dispersion relation describing the optical properties of the film itself. The equation used to describe the film refractive index was:

$$(n + ik)^2 = 1 + \frac{A(1)\lambda^2}{\lambda^2 - \lambda_0^2 - i2\lambda A(2)} \quad (\text{eq. 1})$$

where  $(n + ik)$  is the complex refractive index,  $\lambda$  is the wavelength in nm,  $\lambda_0$  is the oscillator position, and  $A(1)$  and  $A(2)$  are constants. Both  $\lambda_0$  and the  $A(j)$  were determined during the fitting. To reduce the number of variables, the optical properties of the film were assumed to be isotropic.

Reference optical property data were used to describe the substrate dielectric functions. For sapphire, reference data were taken from Malitson [17] and Jeppesen

[18] for the ordinary and extraordinary indices, respectively. Because the literature values for  $dn/dT$  are so small (on the order of  $10^{-5}/^{\circ}\text{C}$ ), room temperature data for the refractive indices of sapphire were used at all temperatures. For the Pt-coated silicon substrates, ellipsometric spectra were collected for the bare substrate, and were directly inverted to provide an effective dielectric function for the exposed metal. Modelling of the data for these substrates showed that the surfaces consisted of roughened platinum. Unfortunately, the degree of roughness was found to change as the substrates were heated, so there is considerable residual uncertainty in the effective dielectric functions for the Pt-coated silicon substrates.

For the modelling, the data sets were truncated to between 400 and 800 nm in order to eliminate the onset of the absorption edge in PZT. Output from the fitting program included values for the "best-fit" parameters, 90% confidence limits for each variable, a correlation coefficient matrix describing the interrelatedness between variables, the unbiased estimator,  $\sigma$  [4], of the goodness of fit, and calculated  $\Delta$  and  $\Psi$  spectra for the final model. All of these factors were examined to determine the appropriateness of a given model.

With the exception of the films on (0001) sapphire, all of the fitting was done assuming that both film and substrate could be treated as isotropic materials. The routine which handled the propagation of light through anisotropic materials was written by Parikh and Allara [19] following the  $4 \times 4$  matrix formalism of Yeh [20,21]. An anisotropic substrate model was not used for the film on ( $\bar{1}\bar{1}02$ ) sapphire as the angle between the inclined optic axis of the alumina and the plane of incidence of the light could not be determined accurately.

#### Analysis of Crystallized MIBERS Films on Sapphire and Pt-coated Silicon

Results from the ellipsometric modelling of the SE data for the films annealed at  $650^{\circ}\text{C}$  for 2 hr are shown in Table 1. All of the films were determined to be between

400 and 600 nm thick, which is consistent with profilometry measurements on the same films. In most cases, a low density interfacial layer between the substrate and the film was essential to properly match the peak heights in both the  $\Delta$  and  $\Psi$  spectra. In addition, a layer of surface roughness improved the fit for some films. As seen in Figure 5, the final fits resulted in very good matches to the experimental data.

The high refractive indices obtained for the middle layer of the films suggest that this region is reasonably dense. Figure 6 shows the modelled refractive indices for several films on sapphire (determined with  $A(2)$  from eq. 1 assigned to zero) in comparison with reference data for 2/65/35 and 16/40/60 PLZT ceramics [22]. As the refractive index of PLZT ceramics is largely controlled by the Zr/Ti ratio [22], the film on (0001) sapphire in particular shows excellent agreement with the values which would be expected for a dense PZT 50/50 material. The lower  $n$  values for the films on ( $\bar{1}\bar{1}02$ ) sapphire could be due either to the presence of residual porosity distributed throughout the densest portion of the film or the assumption of isotropic behavior for both the film and the substrate. When these films were modelled with reference data from the film on (0001) sapphire, 5.7% additional residual porosity was required in each layer of the film to fit the experimental data.

Unless the restriction  $A(2) = 0$  was imposed during the fitting, however, finite values for the imaginary part of the refractive index in the films were obtained in the SE modelling. In part, the larger  $k$  values may reflect the fact that transparency in lead-based perovskites decreases as the lanthanum content is reduced. The opacity of dense, bulk PZT ceramics has been attributed to light scattering at refractive index discontinuities such as domain walls and grain boundaries consisting of a second phase [23]. It is likely that the same mechanisms are present in the films. In addition, there are probably "microstructural" contributions to the effective  $k$  which arise from inhomogeneities in the film not accounted for in the modelling (i.e. scattering from distributed porosity in the bulk of the film, the presence of a lossy layer associated with

either space charge formation or lead loss during firing, or the presence of additional porosity in the film not properly accounted for in the modelling). It was also found that a non-zero value of  $A(2)$  resulted in an increase in the dispersion found for the film refractive indices and a somewhat improved fit for the SE data on the films. The reason for this additional dispersion is unknown. The values reported in Table 1 are for fits with a non-zero  $A(2)$ . Because of the uncertainties in the optical properties of the Pt-coated silicon substrates, it was not possible to determine the exact refractive indices for PZT films on such substrates.

Figure 7 shows a comparison of the *ex-situ* annealed PZT films on Pt-coated Si and (0001) sapphire substrates. Both are densest throughout the bulk of the films, with low density layers near the substrate and some surface roughness. This type of depth profile is common in films with a columnar or cluster morphology [24]. It is also consistent with SEM observations on the same films [2].

For the same annealing conditions, films on Pt-coated silicon possess a much thicker surface roughness layer than those on sapphire. That could be a result either of the higher degree of roughness of the sputtered Pt substrate or the higher initial PbO content in the film on platinum. As discussed by Yang et al. [25], the roughness of a film with a columnar microstructure is dependent on the smoothness of the substrate: with rougher substrates leading to rougher films. Fox et al. [3] also suggest that crystallization of the perovskite phase and PbO vaporization are important in determining the microstructural features of annealed lead lanthanum titanate films.

#### Evolution of Structure During *In-Situ* Annealing

Films deposited at room temperature on  $(\bar{1}\bar{1}02)$  sapphire and Pt-coated Si substrates were annealed *in-situ* in the ellipsometer to determine whether the inhomogeneities seen in films crystallized conventionally were created during the deposition, or whether they were generated during the annealing. For these studies,

sapphire substrates were preferable as all changes in the spectra with temperature could be attributed unambiguously to the film. For the films on Pt-coated silicon, temperature-dependent changes in the effective substrate optical properties obscured interpretation of the SE data. Nevertheless, the results for the film on Pt-coated silicon seem consistent with those reported for the sapphire substrates.

Figure 8 shows the ellipsometric spectra collected during the annealing of the film on sapphire. The data can visually be divided into three regimes. At low temperatures the interference oscillations are damped strongly at short wavelengths. As shown in Figure 9, however, this additional damping disappears between 450° and 500°C. Little change occurs from this temperature until 600°C, which appears to mark a transition between the second and third regions. The latter, as illustrated with the data after the 650°C anneal, is characterized by higher  $\Psi$  values (See Fig. 8).

It was not possible to model the full spectra at low temperatures with a single oscillator, as that did not mimic the abrupt decrease in damping below 500nm. A much better fit could be achieved by mixing the contribution of the oscillator with reference data for rf sputtered lead oxide [26]. For all low temperature data, reference data for rf sputtered PbO provided a better fit than did data for evaporated PbO, largely because the band gap was shifted 0.6 eV lower in energy. No explanation for the disparity in the dielectric functions of the two was given by Harris et al. [26], though one possibility would be the presence of mixed valence states in the sputtered Pb [27]. Fits to as-deposited films on sapphire substrates were not improved significantly by the addition of surface roughness or a gradient in the PbO content to the model. Due to the strong correlation between the void volume fraction and the PbO content, it was not possible to achieve reproducible fits with low density regions near the film-substrate interface. No evidence for low density regions near the substrate were found in Fox's work on as-deposited MIBERS lead lanthanum titanate films [3].

The volume fraction of PbO remained approximately constant at lower temperatures, but beginning at 450°C, successively less PbO was required to match the ellipsometric spectra. Figure 10 shows the best-fit models for 450 and 500°C; the modelling is improved by allowing the lead "loss" to begin at the film surface and move progressively through the film thickness. Over the same temperature range, the film changed from an orange color to pale yellow.

Two possibilities would account for these changes. First, following composition analysis of as-deposited and annealed films, Fox et al. [3] concluded that as-deposited MIBERS lead lanthanum titanate thin films contain excess PbO which is removed during high temperature annealing. Comparable results were obtained on PZT films [2]. The onset temperature at which this was projected to occur was  $490 \pm 50^\circ\text{C}$  [3]. While this temperature is lower than that reported for PbO loss from bulk  $\text{PbTiO}_3$  samples [28], it is in good agreement with the SE experiments. Secondly, the lead oxide could at  $\sim 450^\circ\text{C}$  revert to a less lossy species. Thus, the increase in transparency at low wavelengths could be associated either with a homogenization of the lead oxidation state or with the incorporation of the lead species in to a more transparent phase (like that of evaporated PbO, the perovskite, or a pyrochlore phase). It is not possible to distinguish between these two mechanisms on the basis of the SE data and both may be operative. Similarly, although it is likely that a pyrochlore phase was formed during these lower temperature anneals (at least for the film on Pt-coated Si), this could not be unambiguously identified on the basis of the SE modelling.

At 550°C the experimental data were fit well with a two layer model consisting of a "dense" underlayer with a thin layer of surface roughness. As shown in Figure 11, the extent of the inhomogeneities becomes more pronounced for anneals above 550°C. In contrast to the samples annealed only at 650°C for 2 hrs (i.e. those not exposed to extended periods at intermediate temperatures), no low-density layer near the film/substrate interface was required to model the ellipsometric spectra.

Between the 500 and 550°C anneals, the film refractive index also increased markedly (see Figure 12). This is most likely associated with the crystallization of the perovskite phase. X-ray diffraction patterns following the 600 and 650°C anneals confirmed that the films on sapphire had converted to the perovskite structure with a very high degree of <110> orientation. Figure 12 also shows that the refractive index remains reasonably constant for all fits above 550°C; there is a slight drop at 650°C (not shown) that is probably associated with the fact that the "dense" bottom layer of the PZT contains some residual porosity. In summary, Figure 13 shows the proposed reaction scheme for changes occurring during the annealing of a MIBERS film deposited at room temperature.

#### Role of Annealing Profile in Controlling Inhomogeneities in MIBERS Films

In comparing the microstructures of films annealed in different ways, it is clear that while the inhomogeneity profiles are consistent for samples given identical annealing schedules, they are strongly dependent on variations in the heating cycle. This is apparent in Figure 14, which shows the SE-determined depth profiles for films annealed at 650°C for 2 hrs with and without extended lower temperature soaks. It is interesting that for samples annealed *in-situ* in the ellipsometer the major changes in the film inhomogeneities were coincident with the crystallization of the perovskite phase. This suggests that while the initial microstructure of a vapor-deposited film is controlled by factors such as substrate temperature, gas pressure, and adatom mobility [29], the final appearance is also a function of any post-deposition processes involving diffusion. Thus, in ferroelectric films elimination of excess PbO, reaction with the substrate, crystallization of either the pyrochlore or perovskite phases, and grain growth could successively alter the film microstructure. Additional support for this hypothesis is given by Fox et al. [3], who used scanning electron microscopy to follow the microstructural evolution of MIBERS lead lanthanum titanate films.

It is demonstrated in the following section that inhomogeneities in the microstructure, especially those associated with low density regions, alter the net coercive field, dielectric constant and remanent polarization of ferroelectric films. Given the dependence of the microstructure on the details of the post-deposition annealing profile observed here, it is clear that two films of the same composition, crystal structure, and thickness, which were annealed at the same peak temperature, could nevertheless still possess considerably different electrical properties. Consequently, post-deposition annealing should be considered an important variable in both the microstructure and property development of ferroelectric films.

It is also clear that the reasons for the discrepancies between the properties of the two films in Figure 14 would not be detected by X-ray diffraction. This clearly establishes the need for microstructure-sensitive characterization techniques in the study of ferroelectric films for device applications. Both spectroscopic ellipsometry and electron microscopy should be useful in this regard.

#### Influence of Inhomogeneities on the Electrical Properties of Films

Some ferroelectric films grown with the MIBERS technique possess low density regions near the film/substrate interface which are consistent with the appearance of either clustering or columns in the annealed film. Such a low density layer should be expected to alter the net electrical properties of the film. Indications of this can be seen experimentally in the hysteresis loop of a film which was shown to have an inhomogeneous depth profile by spectroscopic ellipsometry. The coercive field and net dielectric constant of the film was 75 kV/cm and ~850, respectively. By contrast, a homogeneous film of the same composition and the same grain size (chemically prepared) had a lower coercive field (~40 kV/cm) and a higher net dielectric constant. Both films have higher  $E_c$  values than would be expected for bulk ceramics of the same composition, probably as a result, in part, of the fine grain size of the films and stress

exerted on the film by the substrate [30]. Nevertheless, the inhomogeneous vapor-deposited films possess a higher coercive field and a more severe tilt to the "vertical" sides of the loop than do the homogeneous films. An attempt was made to model the hysteresis loop of the films to determine whether these differences could be attributed to the ellipsometrically characterized inhomogeneities.

To model the effect that embedded porosity of this type would have on the apparent electrical properties of the film, the following approximation was considered. If a representation of a columnar microstructure is subdivided into elements vertically, then most segments contain dense PZT in series with a low dielectric constant layer (see Fig. 15). It is assumed here that the upper electrode is conformal, so that the surface roughness does not strongly influence the net electrical properties of the film. Given these conditions, the net capacitance of one element can be expressed as

$$\frac{1}{C} \propto \frac{\epsilon_2 (d - x) + \epsilon_1 x}{\epsilon_1 \epsilon_2}$$

where  $\epsilon_1$  and  $\epsilon_2$  denote the dielectric constants of the dense and the defective regions respectively,  $d$  is the total film thickness, and  $x$  is the thickness of the low density material. For this geometry, the ratio of the actual coercive field of the dense PZT to the apparent coercive field of the element is

$$\frac{E_{\alpha(1)}}{E_c} = \frac{\frac{V_1}{d-x}}{\frac{V}{d}} = \frac{\epsilon_2 d}{\epsilon_2 (d - x) + \epsilon_1 x}$$

It is also assumed that there are no forces (such as stress) acting to depole the film. While some depolarization will occur in actual samples, tilting the lines bounding the top and bottom of the hysteresis loops, that will not alter the basic conclusions of this argument.

In vapor-deposited materials, the dielectric constant and the thickness of the defective material would be expected to vary locally as nucleation and growth

commenced, leading to a distribution in the capacitances and coercive fields of the different subelements. The absence of a well-defined coercive field, in turn, leads to a loss in the squareness of the hysteresis loop, which is one of the desired attributes for the model. As a first approximation, the dielectric constant and coercive field for the dense fine-grained PZT were assigned the values from the sol-gel film, i.e.  $\epsilon_1 = 1300$ , and  $E_{c(1)} = 40\text{kV/cm}$  [31]. To mimic the slope of the sides of the hysteresis loop for a 600 nm thick MIBERS film, the coercive fields for the elements were divided into equal steps between 40 and 110kV/cm. This gives the right slope and correctly predicts the average value for  $E_C$  (~75kV/cm). The shape of the derived hysteresis loop is also in reasonable agreement with the experimental data.

To further check the validity of this model, the net dielectric constant for a film 600 nm thick with a 60 nm thick low density layer near the substrate was also calculated using a parallel model to average the capacitance of the individual vertical elements. The coercive field distribution described above requires dielectric constant values for the bottom layer to vary between 70 and 1300. This leads to a net dielectric constant for the film of 770, reasonably close to the experimentally observed value of ~850 [2]. The volume fraction of air in the bottom layer of each element needed to cause the assumed coercive field distribution was also calculated using the logarithmic and series approximations for the dielectric constant of a composite. These values bracket the average volume fraction of air derived from the SE determination. This is also reasonable. Consequently, this model provides a good approximation for the observed electrical properties of some types of inhomogeneous ferroelectric films. In all cases heterogeneities within the film should be expected to increase the coercive field value. When a distribution of coercive fields is present, the hysteresis loop should be both significantly broadened and tilted to the right, as is generally observed in reported data on ferroelectric thin films.

Moreover, depending on the distribution of porosity in the film, the coercive field of some regions could be so high as to make them practically unswitchable, lowering the apparent polarization for the film. Thus it is possible that a film of well-crystallized ferroelectric could display apparent remanent polarizations significantly below that expected for the bulk ceramic material. This would occur despite the fact that if the film could be fully switched, the remanent polarization would be 99.2% of the bulk value for the case where the bottom 60 nm (of a film 600 nm thick) was, on average, 92% dense.

Finally, defective regions in the film could serve as pinning sites for domain wall motion. This, in turn, could influence both aging and fatigue in ferroelectric films. Consequently, deposition techniques which facilitate production of films which are highly homogeneous, in addition to being highly crystalline, may be essential in the preparation of optimized films for device applications.

It is clear from the above discussion that inhomogeneities in the microstructure can significantly affect the observed low and high field electrical properties of ferroelectric films. This explains much of the variability reported in the literature for these properties. As the degree and types of inhomogeneities present in the film are controlled by the preparation conditions, it is not surprising that films prepared under different conditions display widely disparate dielectric constants and hysteresis loops. However, the role of inhomogeneities has often been ignored. For vapor deposited films, low-energy ion bombardment during growth and rapid thermal annealing have been shown to be useful in improving the film microstructure [32,33].

#### Role of Inhomogeneities on Apparent Size Effects in Ferroelectric Films

Any film which contains low density regions near the substrate should also be expected to display marked extrinsic size effects. Thus, for the films discussed above, and for other vapor-deposited films grown under low adatom mobility conditions, as the

total film thickness is decreased, the defective layer contributes a larger fraction to the overall properties, and the observed properties demonstrate an extrinsic dependence on film thickness.

Consider, for example, the simplified model for the MIBERS film discussed in the previous section, where the first 60 nm of perovskite has a lower density than the remainder of the film. As before, the dielectric constant of the defective region will be distributed between 70 and 1300, so that the hysteresis loop of the film has the proper shape. If this initial layer is kept constant while the total film thickness of the film is varied, then the hysteresis loops become progressively broader and more tilted as  $d$  is decreased (see Fig. 16). At the same time, the net dielectric constant drops off markedly, even though  $\epsilon$  for the solid phase is assumed to remain unchanged. Thus, an infinitely thick film would be essentially undisturbed by the anomalous layer, and would have a well-defined coercive field and dielectric constant equivalent to the values for a bulk, fine-grained ceramic. For thinner films, however, both  $\epsilon$  and  $E_c$  diverge from the bulk values. The decrease in dielectric constant for thinner films shown in Figure 16 is also in agreement with a variety of experimental studies [31,34].

Figure 16a is drawn with even the thinnest films showing the maximum value for the remanent polarization. If the low density layer is, on average, 92% dense (i.e. the ellipsometrically determined value), this is a good approximation, even for the 100 nm thick film, since the effective remanent polarization is calculated to be 95.2% of the bulk value. As the film thickness increases, the maximum  $P_r$  value rapidly approaches 100% of the bulk value. However, this marks the limiting value for  $P_r$  assuming that full switching of the film could be achieved. In practice, it is more likely that given the presence of high local coercive fields in the thinner films, some areas of the film would become unswitchable, and the measured remanent polarization would be lowered.

The sensitive dependence of the apparent size effects on the initial stages of the film microstructure would also explain why films prepared under different conditions

demonstrate different properties as a function of thickness. Spectroscopic ellipsometry offers one means through which depth profiles of inhomogeneities in thin film samples can be characterized non-destructively, and so should be useful in resolving many of the residual questions about structure-microstructure-property relationships in ferroelectric films.

### **Conclusions**

It has been shown that spectroscopic ellipsometry can be utilized to characterize the microstructural inhomogeneities in ferroelectric thin films. Some degree of inhomogeneity (in the form of low density layers or surface roughness) was found in each of the films examined; in all cases these were more important in modelling the ellipsometric spectra than were intrinsic changes in the properties of the ferroelectric phase as a function of film thickness. The presence of microstructural inhomogeneities is not necessarily linked to the existence of a poorly crystallized film. As a result, well-crystallized, and even well-oriented films can display poor microstructures.

A model was developed to approximate the effect that such local density variations should have on the net electrical properties of an otherwise perfect film. Depending on the configuration of the embedded porosity, it was demonstrated that microstructural inhomogeneities can profoundly alter the dielectric constant, coercive field, and remanent polarization of ferroelectric films. Effects of this type are expected to be especially pronounced in vapor-deposited films with columnar or cluster microstructures and low density sol-gel films. Therefore, optimization of processing conditions to produce dense, homogeneous microstructures will be critical in the development of high quality devices.

Due to the relationship between the film microstructure and the net electrical properties, any systematic variations in the density with film thickness, like those associated with columnar growth, will cause changes in the net film properties as a

function of thickness. This mechanism is expected to be responsible for the majority of apparent size effects reported in the literature. Consequently, in examining the properties of ferroelectric films, and especially in considering the variation in properties with film thickness, it is imperative that some microstructure-sensitive technique, such as microscopy or spectroscopic ellipsometry, be utilized.

It has also been demonstrated that spectroscopic ellipsometry can track the evolution of crystallinity and structural inhomogeneity during annealing of as-deposited MIBERS films. One of the advantages of performing these studies on transparent materials is that the entire depth of the film can be sampled (and characterized) at once. In this work, crystallization of the perovskite phase was shown to be largely complete after half an hour at 550°C for MIBERS films on sapphire substrates. For the prolonged heating cycles utilized during *in-situ* annealing of the ferroelectric films, roughening of the film surface was coincident with this crystallization, and can probably be attributed to the growth of crystal nuclei. In addition, lower temperature phenomena like changes in the lead species present could be identified.

It was found that the final microstructures of MIBERS PZT films is dependent on the details of the annealing process. Thus, while the depth profile of film inhomogeneities was consistent for films given the same annealing schedule, changes in the annealing resulted in considerable modification of the final density distribution. Even films annealed at the same peak temperature, but which were exposed to intermediate temperatures for different lengths of time displayed this type of behavior. Consequently, while the final film microstructure will be influenced by the as-deposited state, it will not necessarily be controlled only by the deposition parameters.

This has several important consequences in terms of processing ferroelectric films for device applications. First, the post-deposition annealing schedule can be as important as the deposition conditions in controlling the film microstructure, and thus the film properties. Second, evaluation of annealing schedules should be conducted in

light of structural information for the film (i.e. from microscopy or spectroscopic ellipsometry) in addition to X-ray diffraction information. Third, as the net electrical properties depend on the inhomogeneities present in the film, some limited property tuning may be possible given proper control of the annealing process. In particular, porosity profiles could be tailored to permit control or grading of the film properties (i.e. structural or optical) through the thickness. One area in ceramic materials in which this type of control might be interesting is in the preparation of functionally gradient materials or in ceramic membranes.

### References

- 1 S. B. Krupanidhi, *J. Vac. Sci. & Technol. A*, 10 (1992) 1569 .
- 2 S. B. Krupanidhi, H. Hu, and V. Kumar, *J. Appl. Phys.*, 71 (1992) 376.
- 3 G. R. Fox, S. B. Krupanidhi, K. L. More, and L. F. Allard, *J. Mat. Res.*, 7 (1992).
- 4 D. E. Aspnes and J. B. Theeten, *Phys. Rev. Lett.*, 43 (1979) 1046.
- 5 K. Vedam, P. J. McMarr, and J. Narayan, *Appl. Phys. Lett.*, 47 (1985) 339.
- 6 P. J. McMarr, K. Vedam, and J. Narayan, *J. Appl. Phys.*, 59 (1986) 694.
- 7 J. Narayan, S. Y. Kim, K. Vedam, and R. Manukonda, *Appl. Phys. Lett.*, 51 (1987) 343.
- 8 N. V. Nguyen, K. Vedam, and J. Narayan, *J. Appl. Phys.*, 67 (1990) 599.
- 9 P. Chindaudom, *Characterization of Inhomogeneous Transparent Thin Films on Transparent Substrates by Spectroscopic Ellipsometry*, Ph.D. Thesis, The Pennsylvania State University (1991).
- 10 P. Chindaudom and K. Vedam, *Opt. Lett.*, 17 (1992) 538.
- 11 S. Krishnakumar, S. C. Esener, C. Fan, V. H. Ozguz, M. A. Tittle, C. Cozzolino, and S. H. Lee, *MRS Symposium Proceedings Vol. 200: Ferroelectric Thin Films* E. R. Myers and A. I. Kingon, eds. MRS: Pittsburgh, PA 1990 91.
- 12 D. E. Aspnes, *J. Opt. Soc. Am.*, 64 (1974) 812.

- 13 P. Chindaudom and K. Vedam, *Appl. Opt.* 1993 (submitted).
- 14 J. M. M. de Nijs and A. van Silfhout, *J. Opt. Soc. Am.*, 5 (1988) 773.
- 15 R. J. King and M. J. Downs, *Surf. Sci.*, 16 (1969) 288.
- 16 I. H. Malitson, *J. Opt. Soc. Am.*, 52 (1962) 1377.
- 17 I. H. Malitson, *Opt. Soc. Am.*, 55 (1965) 1205.
- 18 M. A. Jeppesen, *J. Opt. Soc. Am.*, 48 (1958) 629.
- 19 A. N. Parikh and D. L. Allara, *J. Chem. Phys.*, 96 (1992). 927.
- 20 P. Yeh, *J. Opt. Soc. Am.*, 69 (1979) 742.
- 21 P. Yeh, *Surface Science*, 96 (1980) 41.
- 22 P. D. Thacher, *Appl. Opt.*, 16 (1977) 3210.
- 23 C. E. Land, P. D. Thacher, and G. H. Haertling, in *Applied Solid State Science: Advances in Materials and Device Research Vol. 4*, Ed. by R. Wolfe. Academic Press Inc., New York, 1974.
- 24 B. Yang, *Spectroscopic Ellipsometry and Computer Simulation Studies of Thin Film Morphology Evolution*, Ph.D. Thesis, The Pennsylvania State University, 1988.
- 25 B. Yang, B. L. Walden, R. Messier, and W. B. White, *SPIE Proc. 821: Modelling of Optical Thin Films* (1987) 68.
- 26 E. P. Harris, P. S. Hauge, and C. J. Kircher, *Appl. Phys. Lett.*, 34 (1979) 680.
- 27 A. E. Ennos, *J. Opt. Soc. Am.*, 52 (1962) 261.
- 28 R. L. Holman and R. M. Fulrath, *J. Appl. Phys.*, 44 (1973) 5227.
- 29 R. Messier, A. P. Giri, and R. A. Roy, *J. Vac. Sci. Technol. A2* (1984) 500.
- 30 G. H. Haertling, *J. Vac. Sci. Technol. A*, 9 (1991) 414.
- 31 K. R. Udayakumar, J. Chen, S. B. Krupanidhi, and L. E. Cross, *Proc. 1990 IEEE 7th Int. Symp. Appl. Ferroelec.* (1990) 741.
- 32 H. Hu and S. B. Krupanidhi *Appl. Phys. Lett.* 61 (1992) 1246.
- 33 H. Hu, L. Shi, V. Kumar, and S.B. Krupanidhi, *Ceram. Trans.* 25 ed. by A. S. Bhalla and K. M. Nair, The American Ceramic Society, Westerville, Ohio (1992) 113.

- 34 A. A. Gitel'son, A. M. Lerer, V. S. Mikhalevskii, V. M. Mukhortov, and S. V. Orlov,  
*Sov. Phys. Sol. State*, 19 (1977) 1121.

### List of Figures

- Fig. 1: X-ray diffraction patterns of the PZT films on (a)  $(1\bar{1}02)$  sapphire and (b) Pt-coated Si. Films were annealed at 650°C for 2 hours.
- Fig. 2: Schematic of the rotating analyzer ellipsometer utilized in this work.
- Fig. 3: Comparison of uncorrected and corrected SE data for vitreous silica.
- Fig. 4: Electrical resistance furnace and sample mount (a) Side view. (b) Top view of the baseplate and sample holder. The entire baseplate can be translated along y and rotated about z to permit alignment of the sample at any temperature. Rotation of the sample about the x axis was performed with the worm gear and screw shown in the figure. This could also be adjusted at any temperature.
- Fig. 5: Fit to the film on (0001) sapphire.
- Fig. 6: Comparison between the refractive index of PZT films and PLZT ceramics. (Note: Thacher has demonstrated that the refractive index of PLZT ceramics is largely controlled by the Zr/Ti ratio [22]. Consequently, the film refractive indices should fall between those for the 2/65/35 and 16/40/60 PLZT ceramics).
- Fig. 7: Depth profile of the inhomogeneities in films deposited on (a) Pt-coated silicon and (b) (0001) sapphire.
- Fig. 8: SE data for the *in-situ* annealing of a film on sapphire.
- Fig. 9: Annealing of a film showing a decrease in the high energy damping at 500°C. The lower temperature data was very close to that shown for 450°C.
- Fig. 10: Best fit models for intermediate temperature anneals of an as-deposited film on sapphire. Note that the refractive index of the "a-PZT" changed with annealing temperature as shown in Fig. 12.
- Fig. 11: Evolution of microstructure with temperature during high temperature *in-situ* annealing of an as-deposited film on sapphire. Note that the refractive index of the "PZT" material in the film changed continuously during these anneals as

shown in Fig. 12. These changes are probably associated with the crystallization of the perovskite phase.

Fig. 12: Refractive index of an as-deposited film on sapphire as a function of annealing temperature.

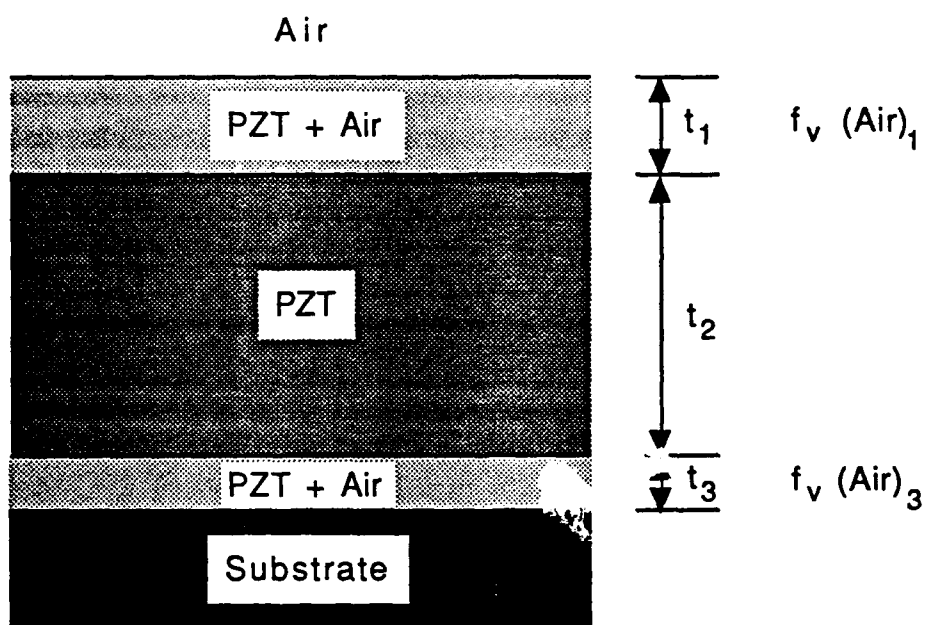
Fig. 13: Reaction scheme for the *in-situ* annealing of a PZT film on sapphire (Note that as a pyrochlore phase could not be identified from the SE data alone, it is not shown on the reaction scheme. It is possible, however, that pyrochlore phase formation is concurrent with the removal of the lossy lead oxide phase).

Fig. 14: Final microstructures of films on sapphire annealed at 650°C (a) with and (b) without extended annealing at lower temperatures. The annealing profile shown for (b) is simplified.

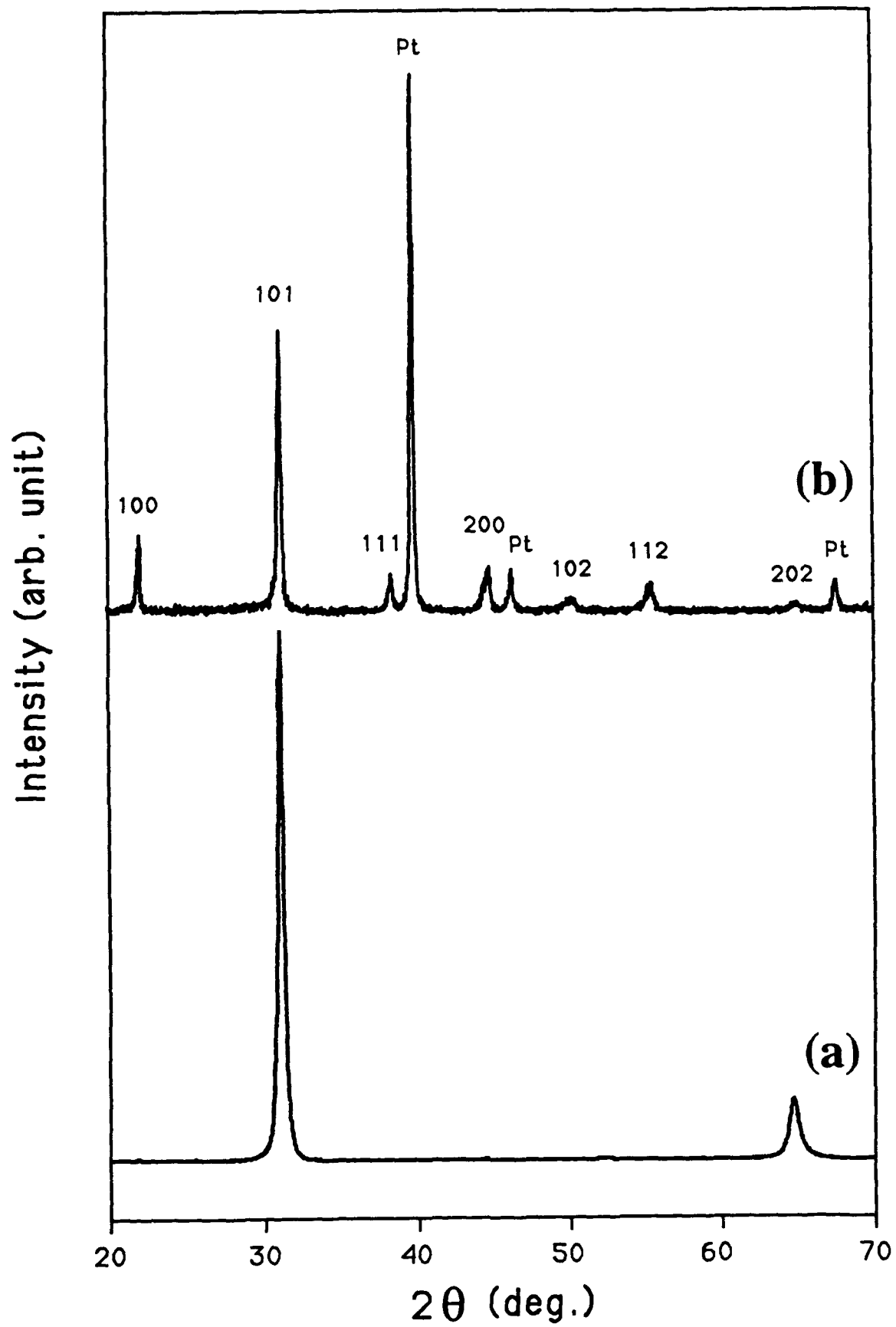
Fig. 15: Geometry used for modelling the effect of inhomogeneities on the electrical properties of an inhomogeneous ferroelectric film. (a) A two-dimensional representation of columnar growth subdivided vertically. (b) One element of the above structure.

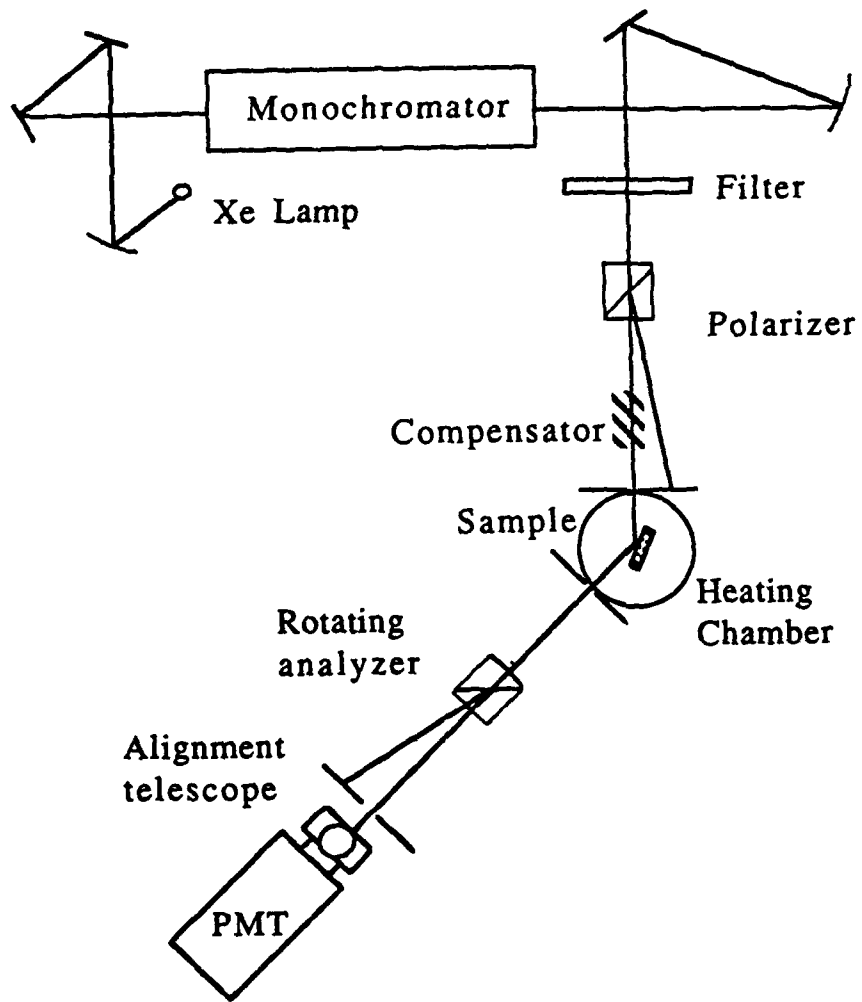
Fig. 16: The effects of a 60 nm thick low density layer near the substrate on the electrical properties of PZT thin films. (a) Variation in the hysteresis loop with the total film thickness. (b) Variation of the dielectric constant and the coercive field with film thickness. Limiting values are  $\epsilon = 1300$  and  $E_c = 40$  kV/cm for a homogeneous fine-grained film on a Pt-coated Si substrate.

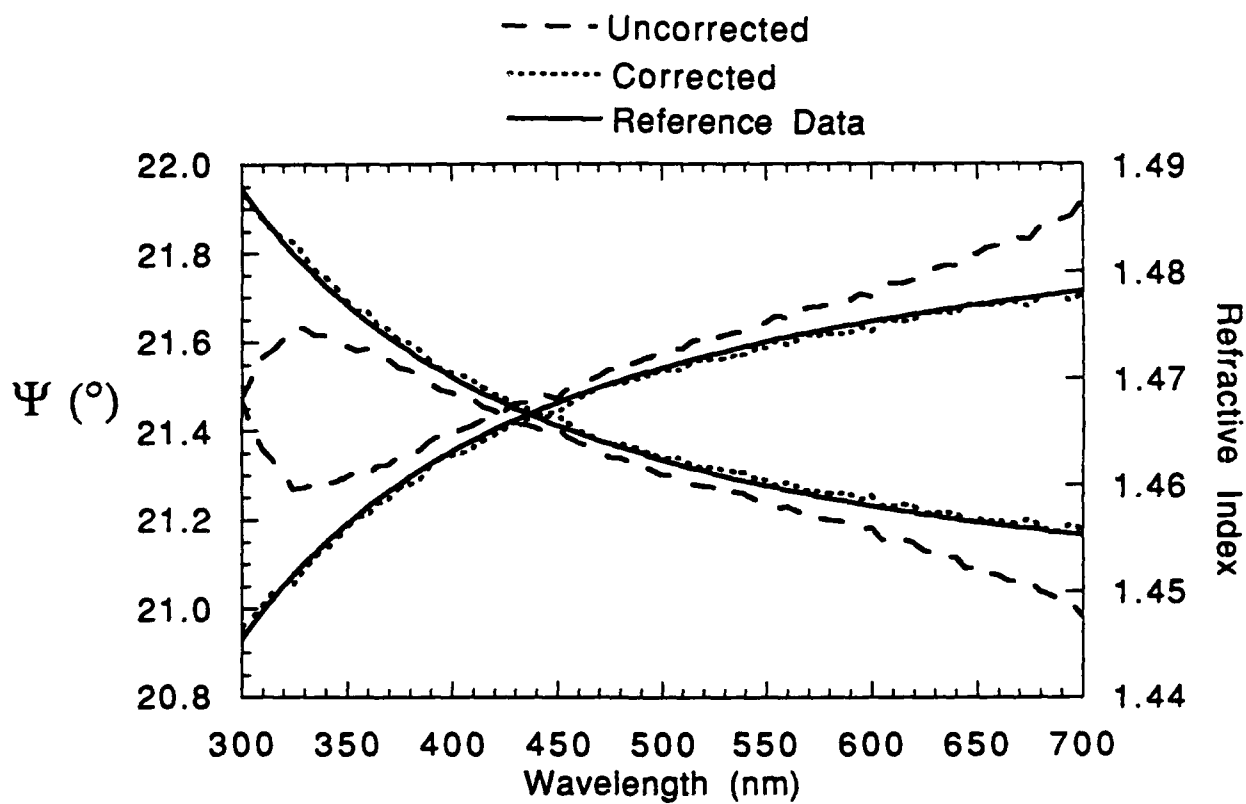
Table 1: Best-fit parameters for the modelling of films annealed at 650°C for 2 hours.



	$f_v(\text{Air})_1$	$t_1$ (nm)	$t_2$ (nm)	$f_v(\text{Air})_3$	$t_3$ (nm)
PZT on (0001) Sapphire	$0.07 \pm 0.02$	$18.3 \pm 5.2$	$478.5 \pm 9.8$	$0.08 \pm 0.01$	$83.9 \pm 3.8$
PZT on ( $\bar{1}102$ ) Sapphire	-----	-----	$548.1 \pm 6.6$	$0.08 \pm 0.01$	$62.4 \pm 4.7$
PZT on ( $\bar{1}\bar{1}02$ ) Sapphire	-----	-----	$580.3 \pm 2.7$	$0.12 \pm 0.01$	$53.8 \pm 1.3$
PZT on Pt- coated Silicon	$0.21 \pm 0.03$	$109.2 \pm 2.6$	$557.5 \pm 18.8$	-----	-----
PZT on Pt- coated Silicon	$0.15 \pm 0.02$	$107.7 \pm 3.9$	$522.0 \pm 25.9$	$0.14 \pm 0.06$	$56.3 \pm 18.5$







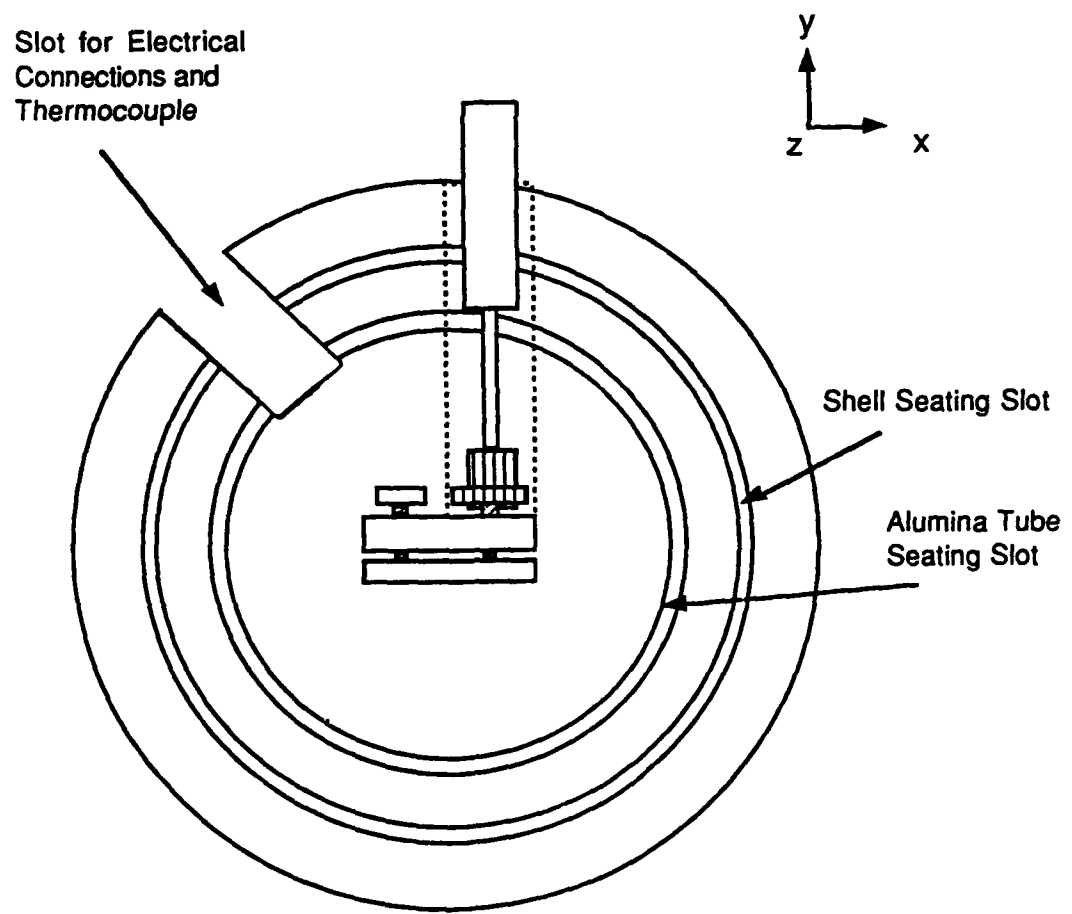
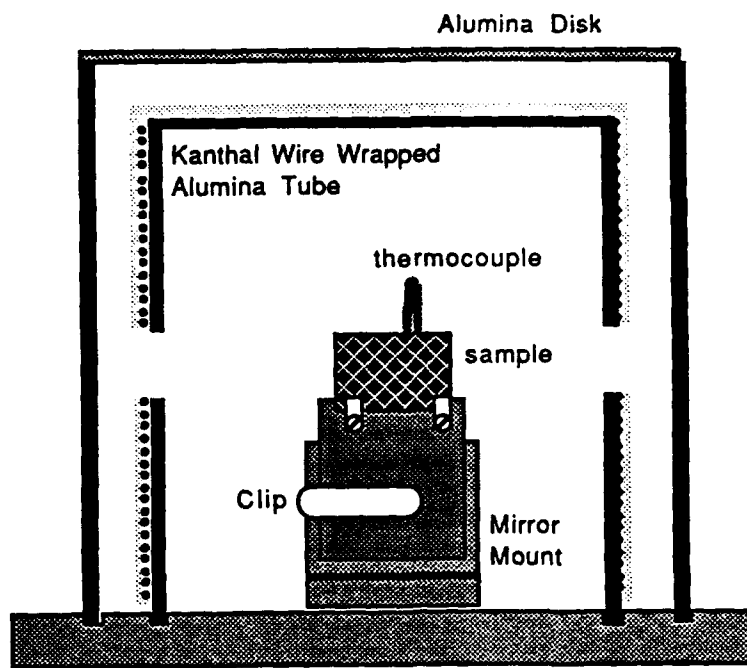
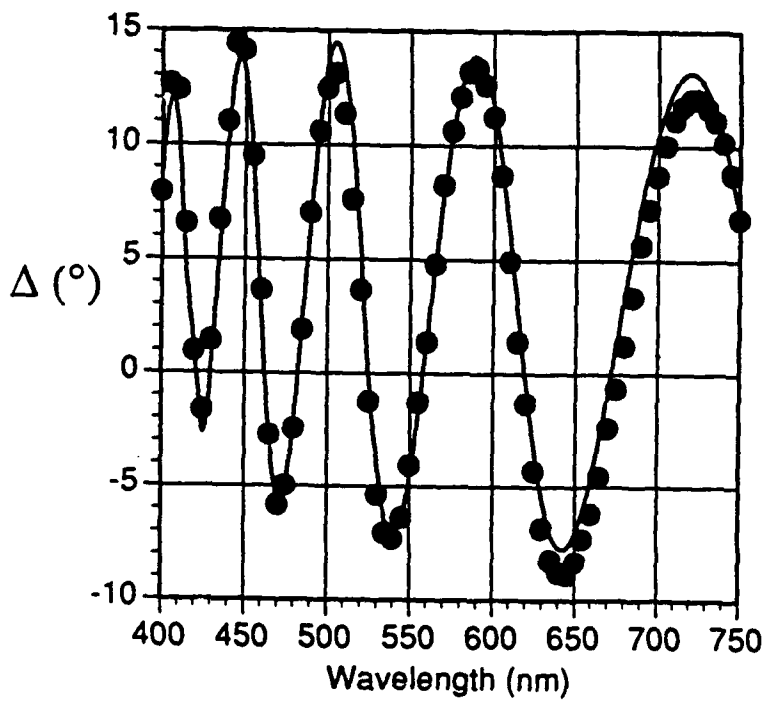
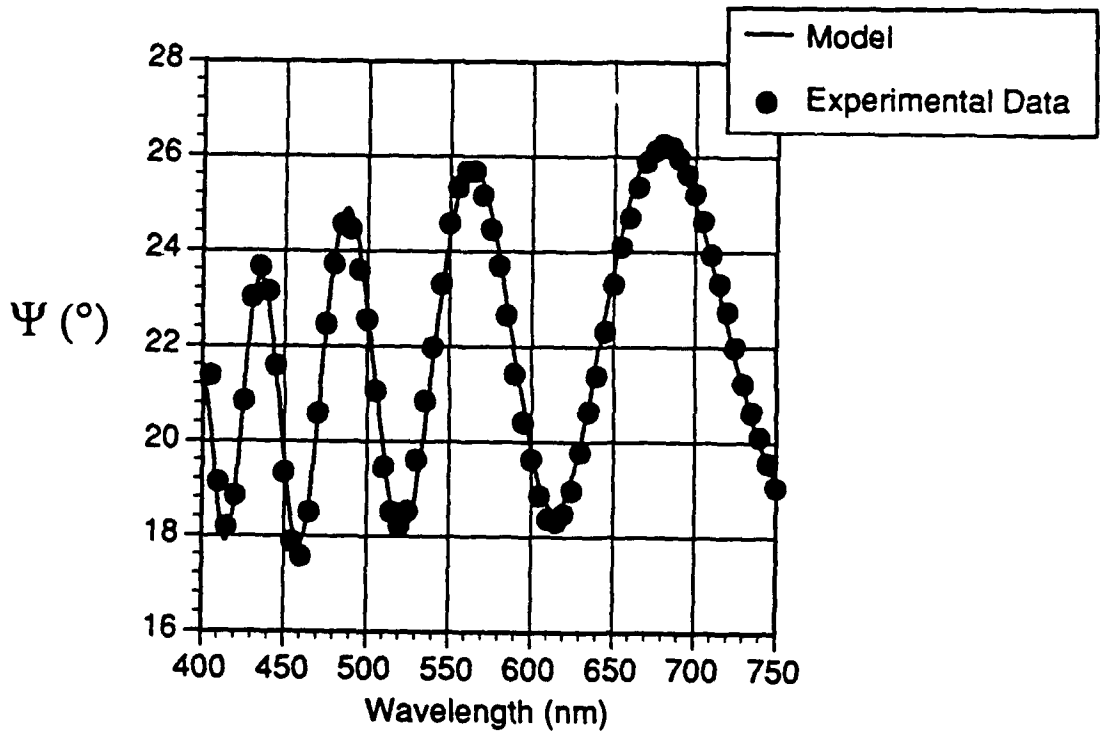
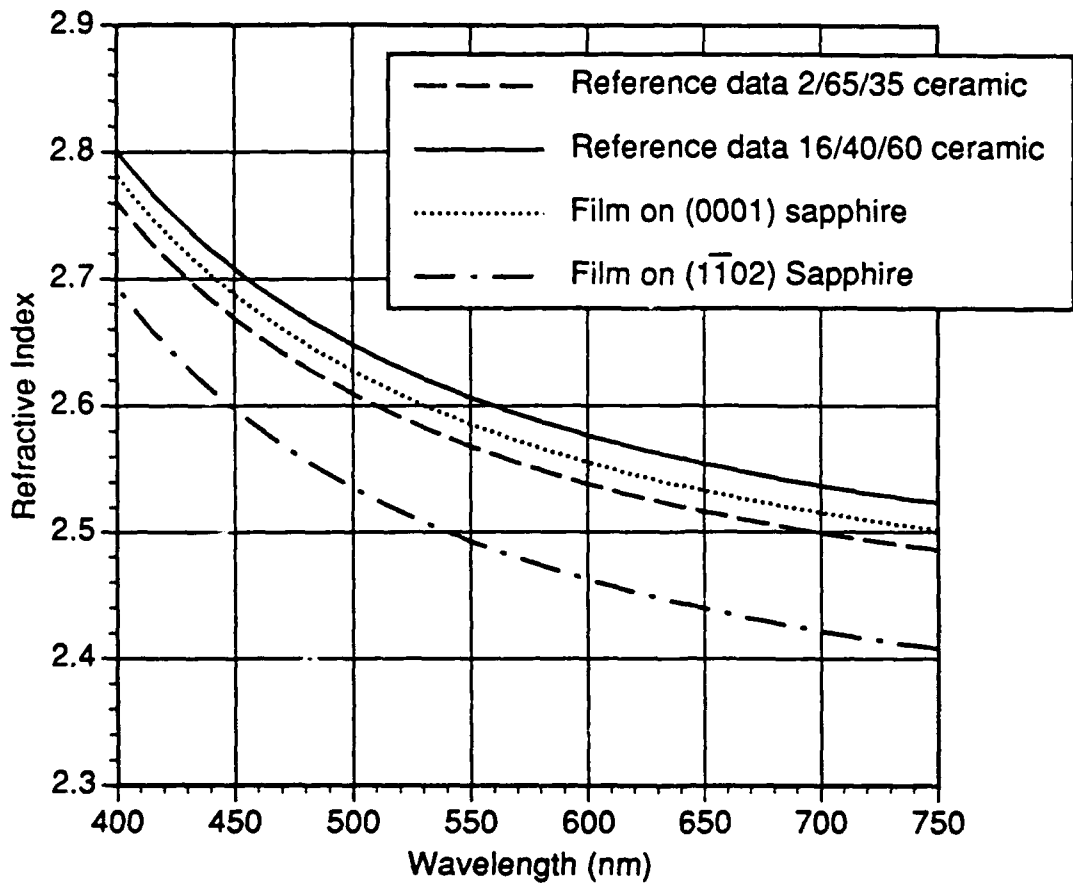
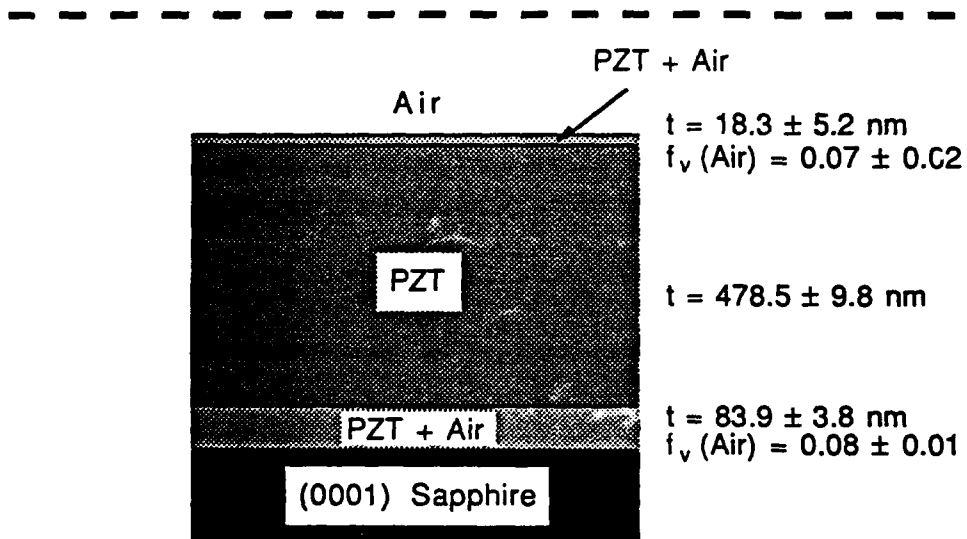
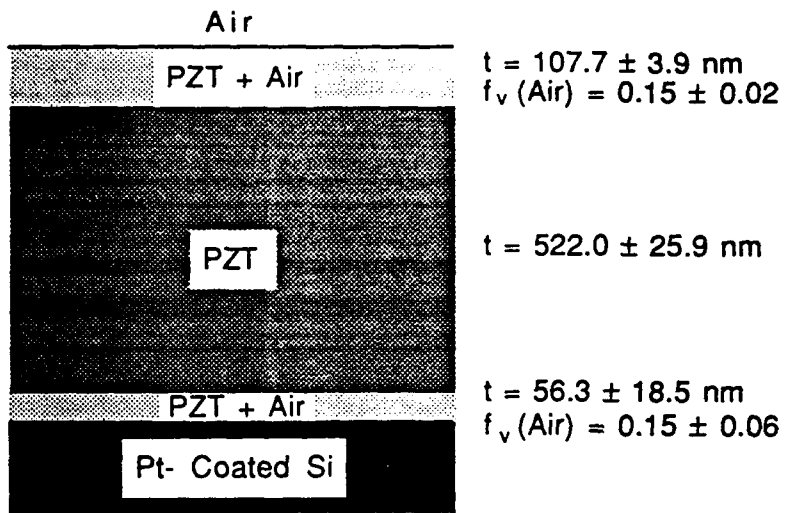
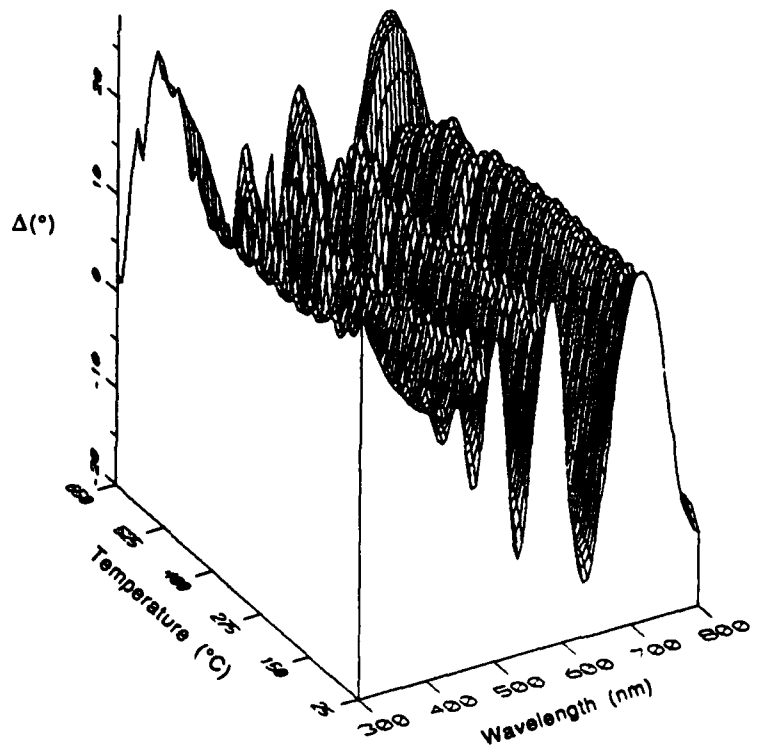
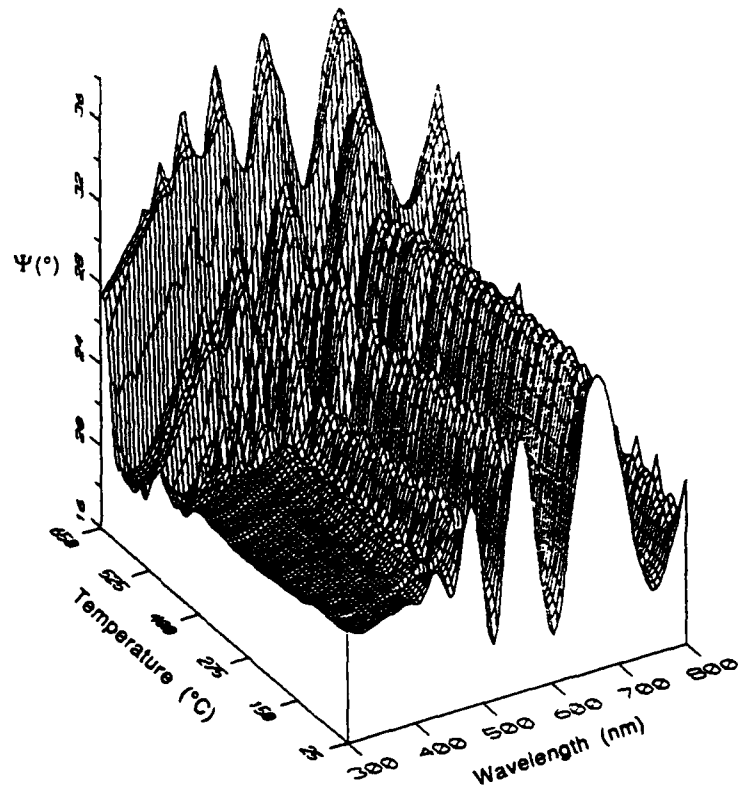


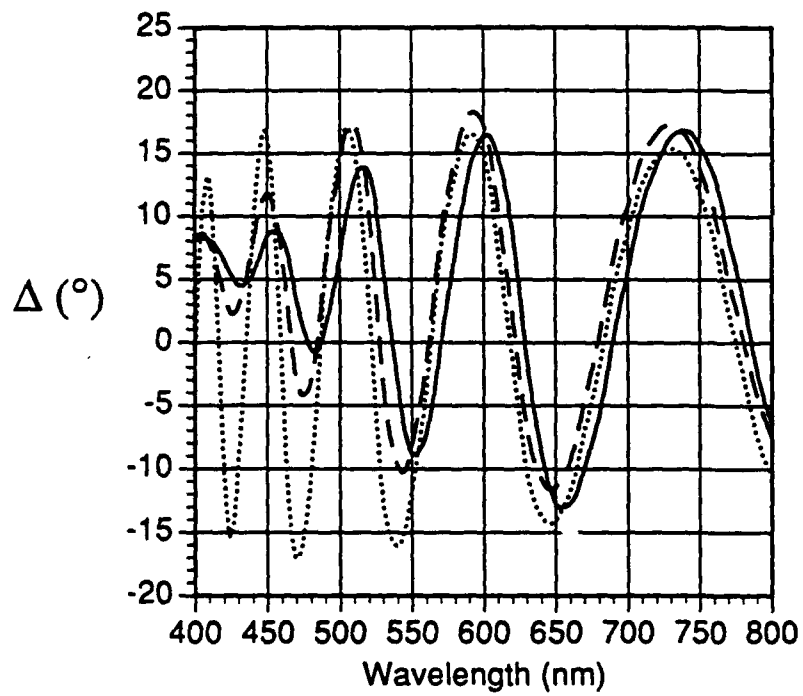
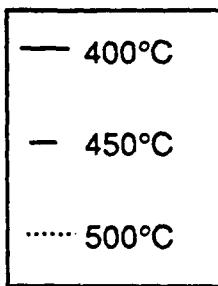
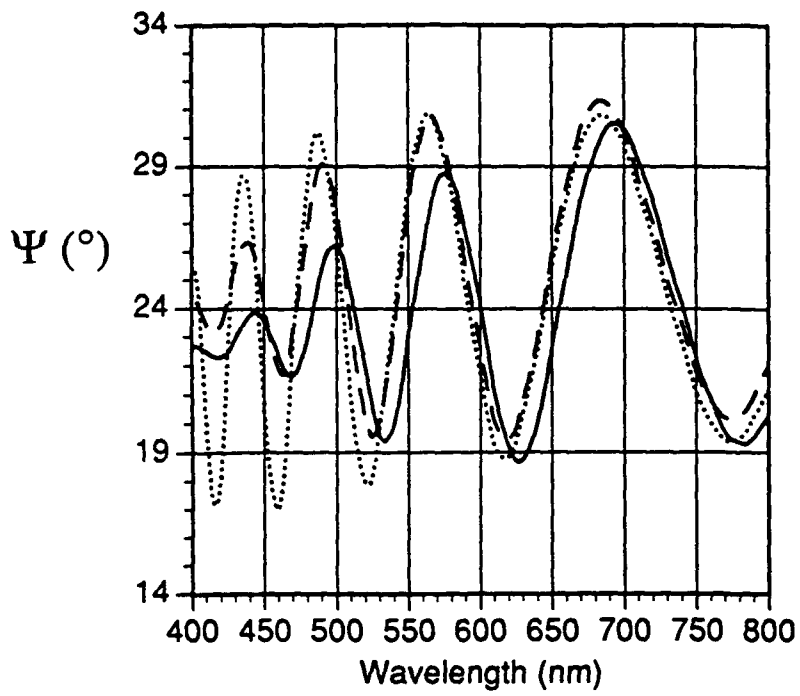
Fig. 1



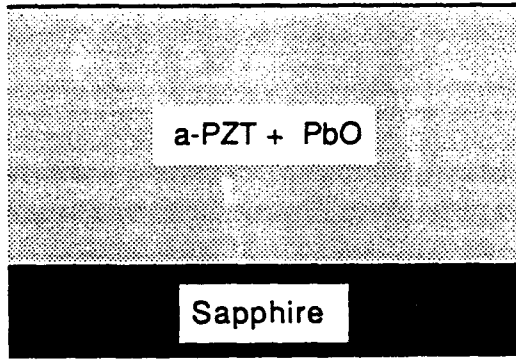






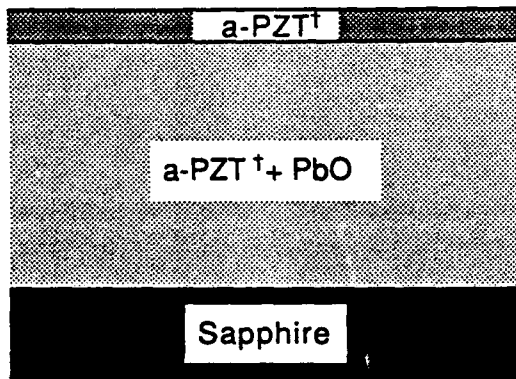


Air



$f_v(\text{PbO}) = 0.26 \pm 0.03$   
 $t = 662.7 \pm 3.8 \text{ nm}$      **400° C**

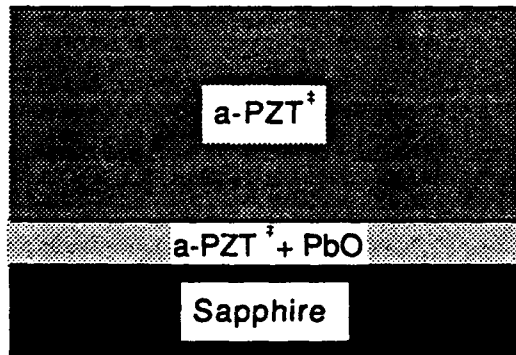
Air



$t = 33.7 \pm 2.6 \text{ nm}$

$t = 619.1 \pm 5.8 \text{ nm}$      **450° C**  
 $f_v(\text{PbO}) = 0.14 \pm 0.01$

Air

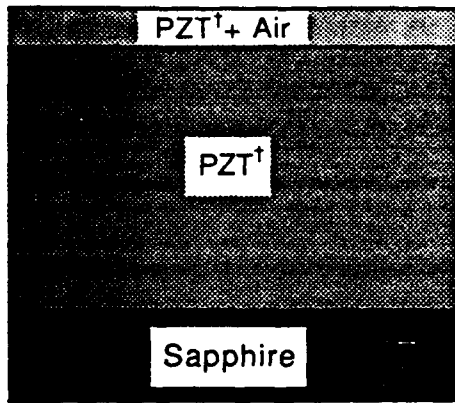


$t = 602.6 \pm 19.4 \text{ nm}$      **500° C**

$t = 63.0 \pm 22.9 \text{ nm}$   
 $f_v(\text{PbO}) = 0.12 \pm 0.06$

550° C

Air

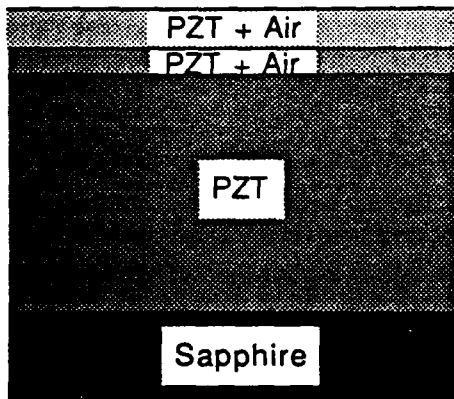


$t = 82.3 \pm 3.4 \text{ nm}$   $f_v (\text{Air}) = 0.06 \pm 0.01$

$t = 492.1 \pm 3.6 \text{ nm}$

600° C

Air



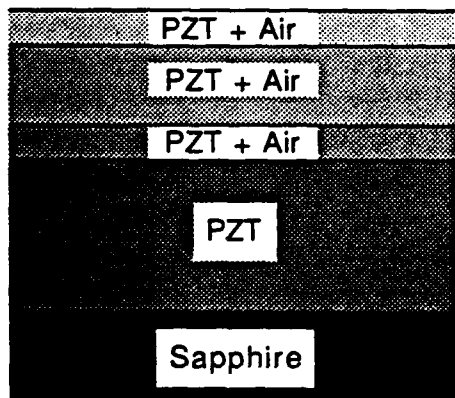
$t = 80.8 \pm 2.3 \text{ nm}$   $f_v (\text{Air}) = 0.26 \pm 0.01$

$t = 47.7 \pm 2.8 \text{ nm}$   $f_v (\text{Air}) = 0.08 \pm 0.01$

$t = 458.9 \pm 8.8 \text{ nm}$

650° C

Air

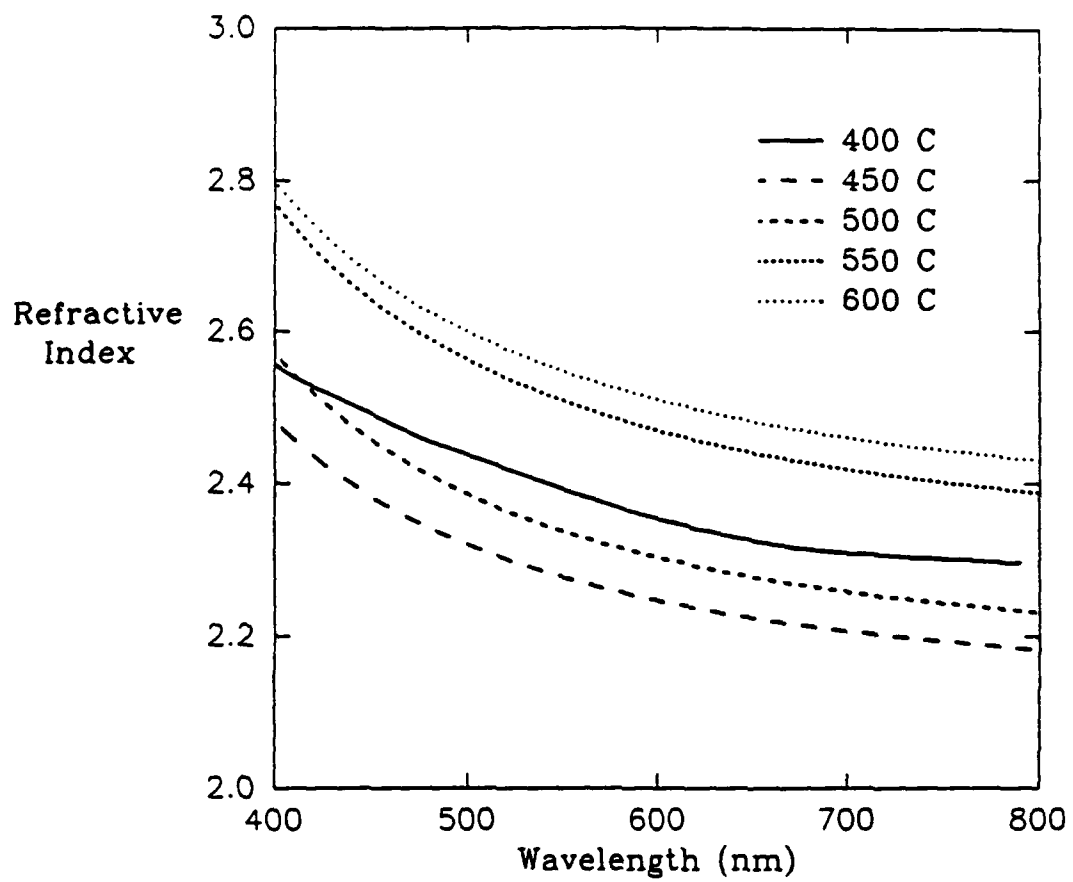


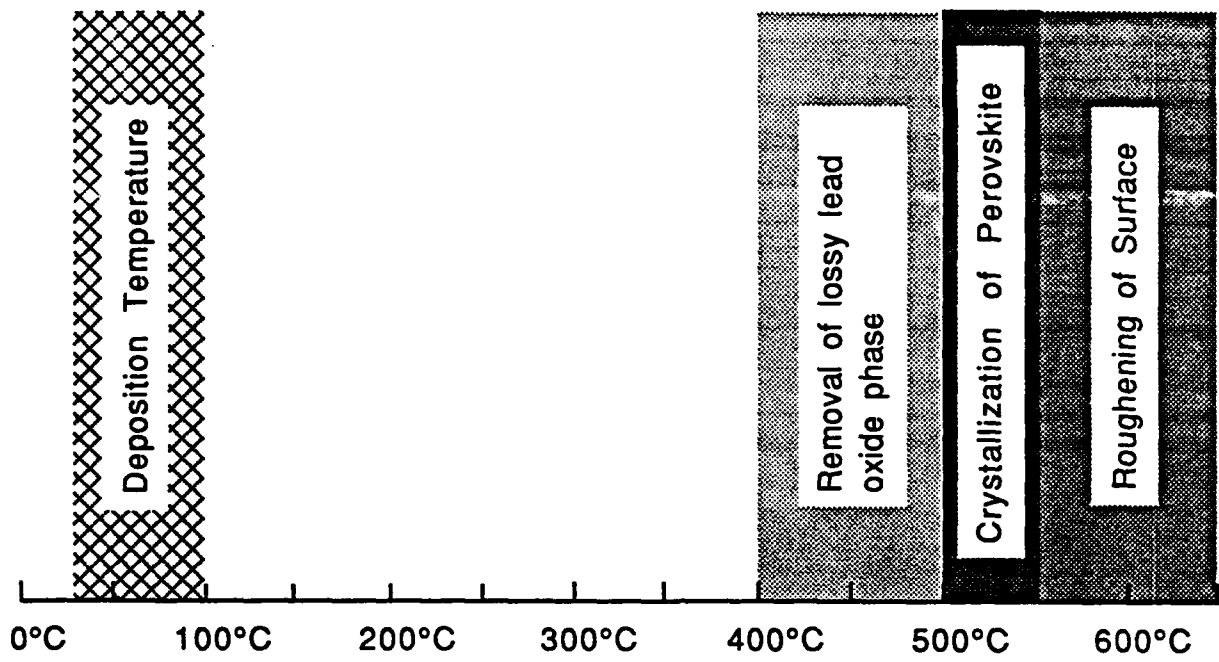
$t = 72.3 \pm 0.4 \text{ nm}$   $f_v (\text{Air}) = 0.56 \pm 0.01$

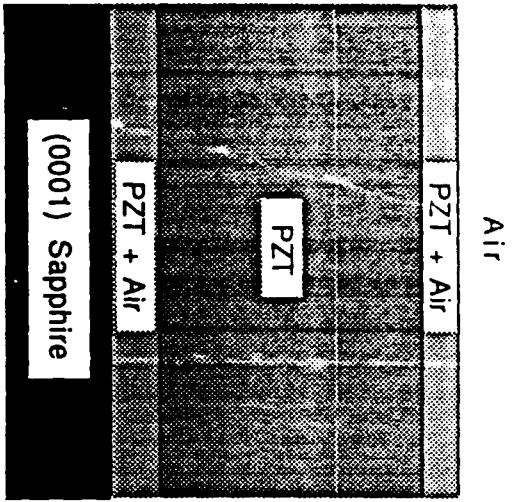
$t = 178.6 \pm 1.9 \text{ nm}$   $f_v (\text{Air}) = 0.15 \pm 0.01$

$t = 57.6 \pm 1.5 \text{ nm}$   $f_v (\text{Air}) = 0.07 \pm 0.01$

$t = 323.7 \pm 5.4 \text{ nm}$

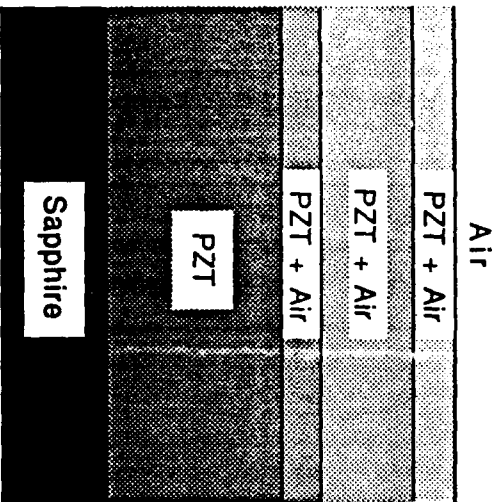
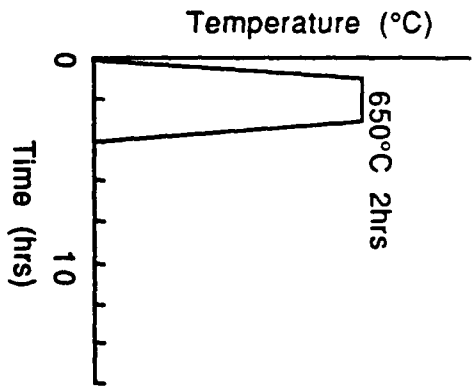






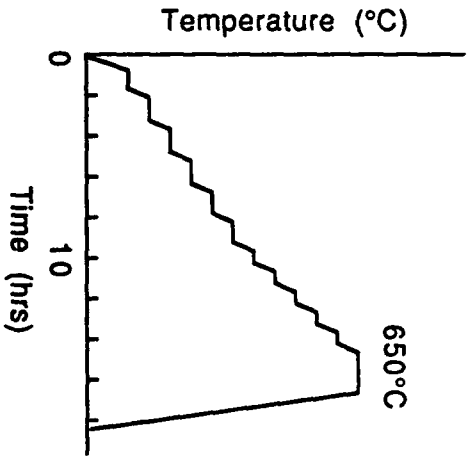
$t = 18.3 \pm 5.2 \text{ nm}$   
 $f_v \text{ (Air)} = 0.07 \pm 0.02$   
 $t = 478.5 \pm 9.8 \text{ nm}$   
 $t = 83.9 \pm 3.8 \text{ nm}$   
 $f_v \text{ (Air)} = 0.08 \pm 0.01$

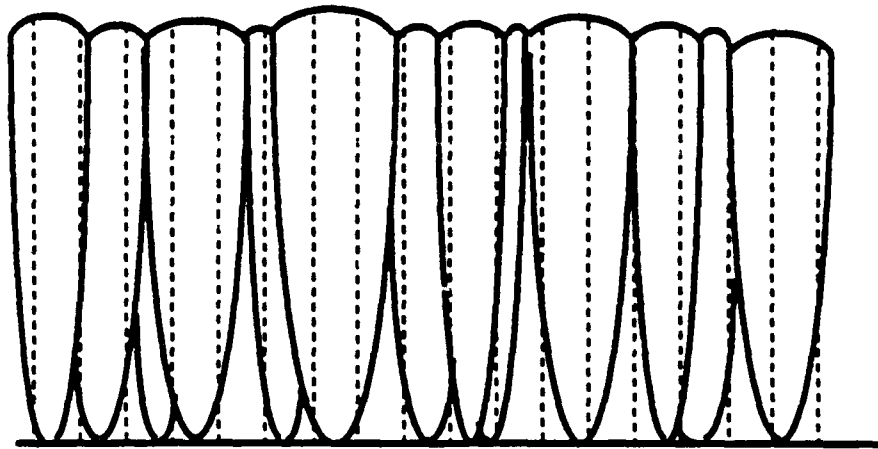
(a)



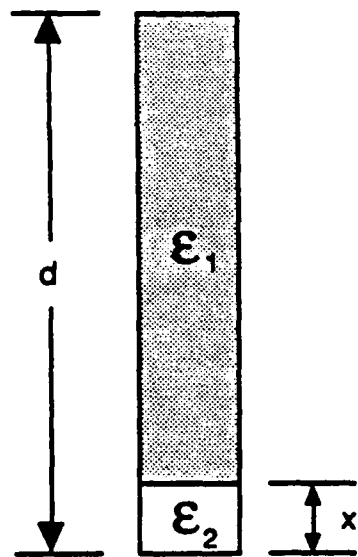
$t = 72.3 \pm 0.4 \text{ nm}$   
 $f_v \text{ (Air)} = 0.44 \pm 0.01$   
 $t = 178.6 \pm 1.9 \text{ nm}$   
 $f_v \text{ (Air)} = 0.15 \pm 0.01$   
 $t = 57.6 \pm 1.5 \text{ nm}$   
 $f_v \text{ (Air)} = 0.07 \pm 0.01$   
 $t = 323.7 \pm 5.4 \text{ nm}$

(b)

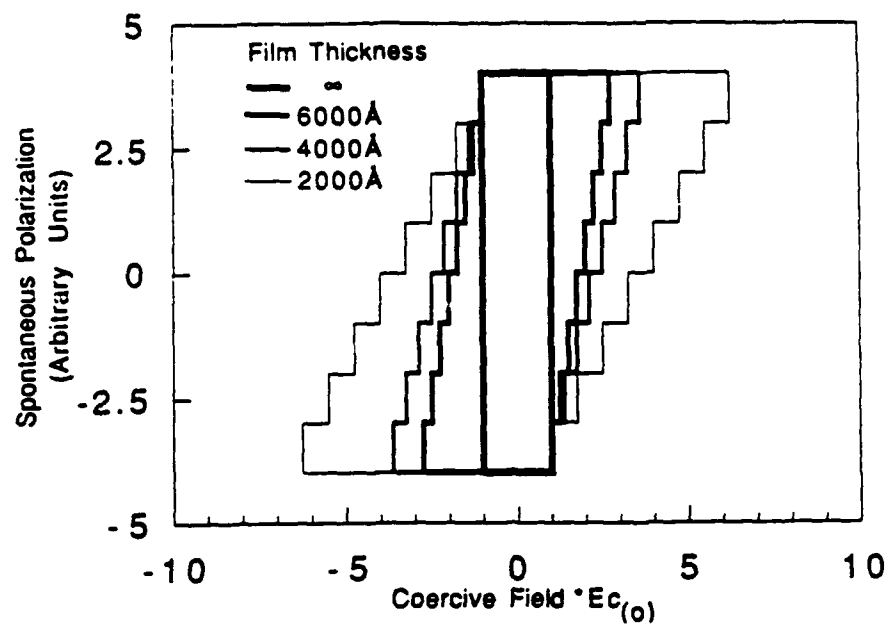




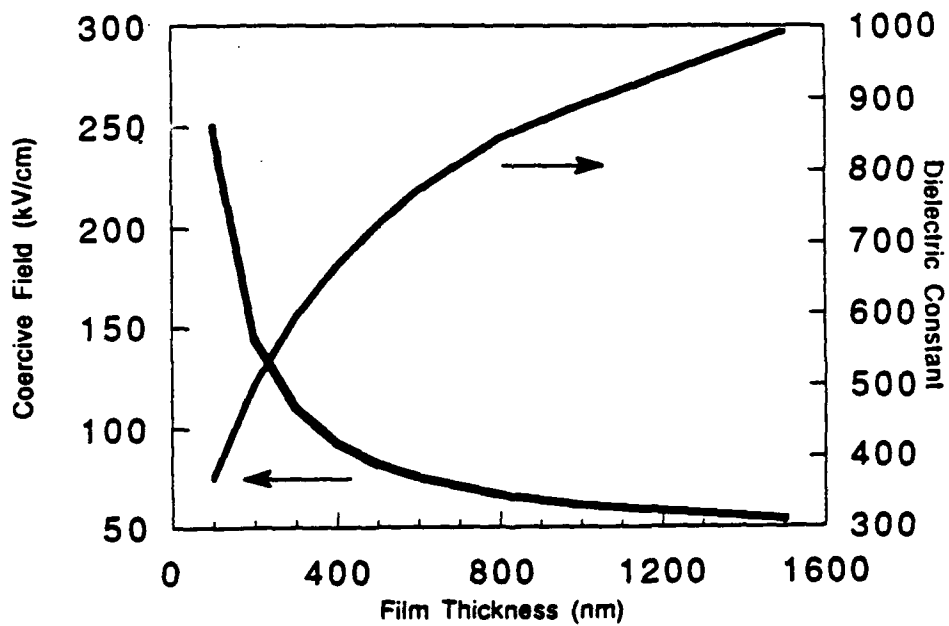
(a)



(b)



(a)



(b)

**APPENDIX 36**

# DIELECTRIC BEHAVIOR OF FERROELECTRIC THIN FILMS AT HIGH FREQUENCIES

J. Chen, K. R. Udayakumar, K. G. Brooks, and L. E. Cross  
Materials Research Laboratory  
Pennsylvania State University  
University Park, PA 16802

## Abstract

The high frequency dielectric response of sol-gel derived lead zirconate titanate (PZT) thin films has been investigated. Conceptualizing the presence of interface layers was critical in explaining the dielectric measurements. By a careful control of the processing parameters, aided by rapid thermal annealing, the low frequency dielectric characteristics could be sustained upto a GHz range.  $\text{Ba}_{0.5}\text{Sr}_{0.5}\text{TiO}_3$  which is paraelectric at room temperature appears to be a potential candidate material for high frequency applications.

## Introduction

In these modern times, many and varied are the applications of high frequency dielectrics; in high resolution/ digital communication devices encompassing cellular phone and satellite communications, in microelectronics and packaging for high speed switching mode power supply, in frequency sensors for microwave detection, to plainly list but a few. Dielectrics qualifying for such applications must possess high dielectric permittivity, low dissipation loss, and low temperature coefficient of electrophysical properties. Ferroelectric materials, which constitute a unique subclass of dielectrics, while very promising in satisfying these general attributes, suffer from a drop in the dielectric constant at a characteristic frequency, ascribed to the piezoelectric resonance of the crystallites as well as the inertia of the domain boundaries; other plausible explanations advanced for the phenomenon include the existence of interface layers at the film-electrode boundary, impurities in the film, and grain imperfections as also grain boundaries. At still higher frequencies, an additional drop in the relative permittivity may occur, assigned generally to dielectric relaxation. In paraelectric materials, no piezoelectric resonance can occur if the phase is centrosymmetric; the clamped and free dielectric constant, which refer to the dielectric constant at frequencies above and below piezoelectric resonance respectively, are equal to one another. At a given high frequency, dielectric relaxation can still cause a fall in the dielectric permittivity in this non-polar phase.

Shifting the focus from the confines of the bulk materials to the dielectric behavior of ferroelectric thin films at low-amplitude a.c. field of high frequencies, as in the present study, the dominant factors that influence relaxation appear to be connected to the presence of interface layers, and grain imperfections. For, first, these films have been characterized by very small grain sizes, in the 0.1-0.2  $\mu\text{m}$  range [1,2], that has the effect of displacing the threshold frequency due to the piezoelectric clamping of grains or domains to higher levels; and second, fabrication of the films through the sol-gel process ensures maximal chemical purity. This study will, consequently, argue that the dielectric dispersion in the 1 MHz to several GHz range stems from the presence of barrier layers and grain imperfections, both of which can be squarely linked to the film processing.

## Results and Discussion

The PZT films used in the study were of the morphotropic phase boundary composition (with a Zr/Ti mole ratio of 52/48), fabricated by the sol-gel spin-on technique. The details of the film fabrication as well as the structural and electrophysical characterization of these films have been outlined in Refs. 1 and 2; the dielectric and ferroelectric property measurements were limited to the radio frequency range in these earlier studies. For dielectric measurements in this study, a high frequency impedance analyser (HP 4191A) was used. All the films were rapid thermally annealed at temperatures and times as specified.

Fig. 1 is a plot of the dielectric permittivity as a function of frequency for a 0.385  $\mu\text{m}$  thick PZT film, rapid thermally annealed in the temperature range of 600-800°C for 60 seconds. It is patent from the figure that with increasing annealing temperature, the relaxation frequency decreases systematically; of greater import is the precipitous tumble in permittivity to almost a cipher at this frequency. While this latter point is seemingly baffling at first glance, the frequency response of the measured dielectric constant and the corresponding impedance spectrum from the equivalent circuit model, based on properties of the

film core, the electrode, and a series resistance [3], lends a modicum of understanding to the anomalous dielectric behavior. Sayer et al. [3] postulated the formation of an interface layer at the top electrode-film boundary and the film-substrate boundary; by varying the internal barrier layer thickness from 0.01  $\mu\text{m}$  to 0.5  $\mu\text{m}$  (the disturbed layer at both the interfaces are lumped) on a film of 1  $\mu\text{m}$  total thickness, the dielectric constant was computed, which has been reproduced here as Figure 2. Scrutiny of this figure, and its juxtaposition with Fig. 1, reveals a striking similarity, tempting the speculation of the presence of interface layers of increasing thickness with increasing severity of annealing of the films. As observed by the authors [3], the calculated higher dielectric constant for films with thicker barrier layers might be related to the assumption of the full thickness of the film in the computations, when in

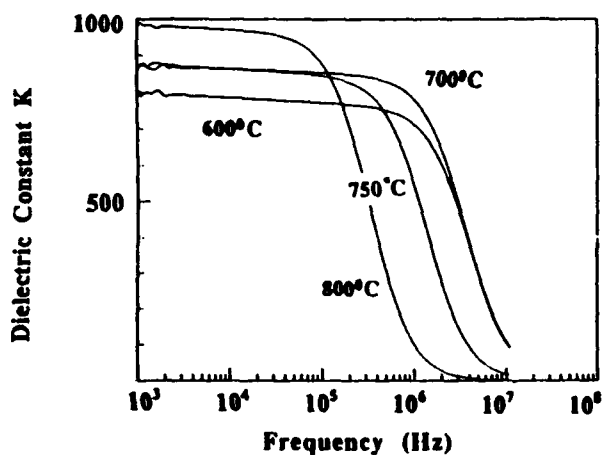


Fig. 1 High frequency dielectric response of PZT thin films, annealed 600-800°C at a constant dwell time of 60 seconds. Note the systematic change in the relaxation frequency with annealing temperature.

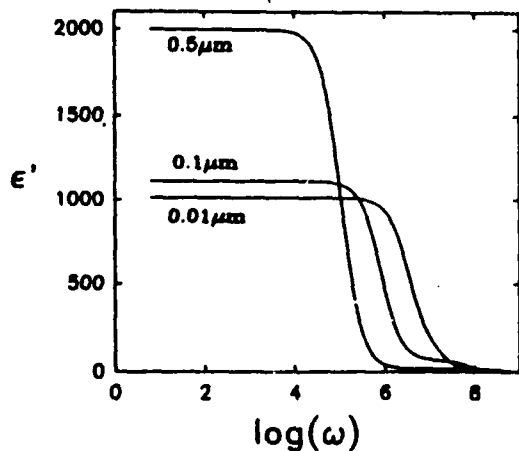


Fig. 2 Computed dielectric constant of a 1  $\mu\text{m}$  film with varying internal barrier thickness; the true value of  $\epsilon' = 1000$  (reproduced from Sayer et al. [3])

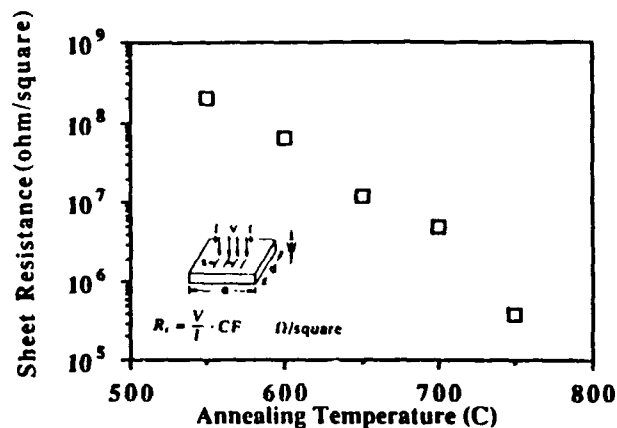


Fig. 3 Resistivity plotted as a function of annealing temperature.

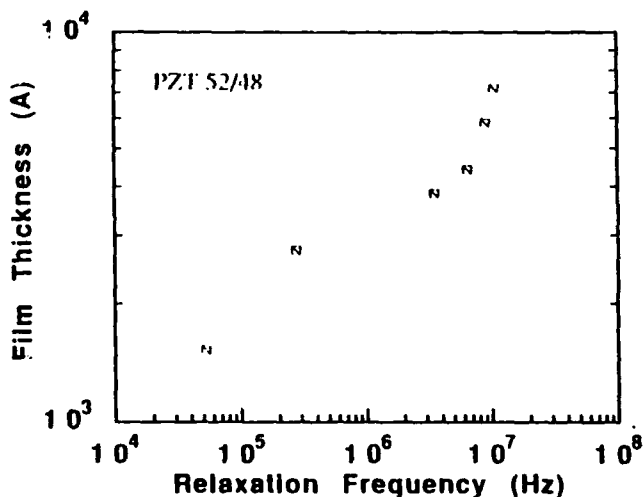


Fig. 4 Relaxation frequencies determined for films of varying thickness shows a drop for thinner films.

reality, it should be smaller by a thickness equal to that of the disturbed layers. In our earlier study [1], the high frequency dielectric relaxation was alluded to the formation of low resistivity surface layers whose resistivity changes with the annealing conditions; from Fig. 3, it is apparent that higher annealing temperature results in lower resistivity of this anomalous layer. Maintaining the same processing parameters, dielectric relaxation frequencies of films varying in thickness from 0.15  $\mu\text{m}$  to 0.75  $\mu\text{m}$  were determined (Fig. 4); thinner films are privy to lower relaxation frequencies, indicating heightened sensitivity to the interface layer formation. When the thermal budget was reduced during annealing by lowering the dwell time from 60 seconds to 10 seconds, there was no

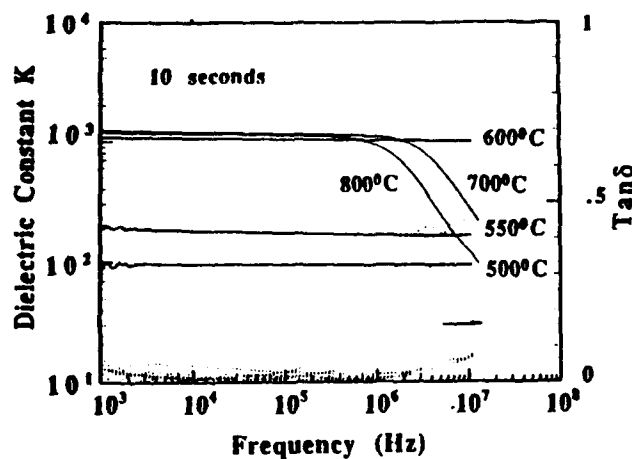


Fig. 5 Dielectric permittivity plotted as a function of frequency for various annealing temperatures but with a reduced dwell time of 10 seconds.

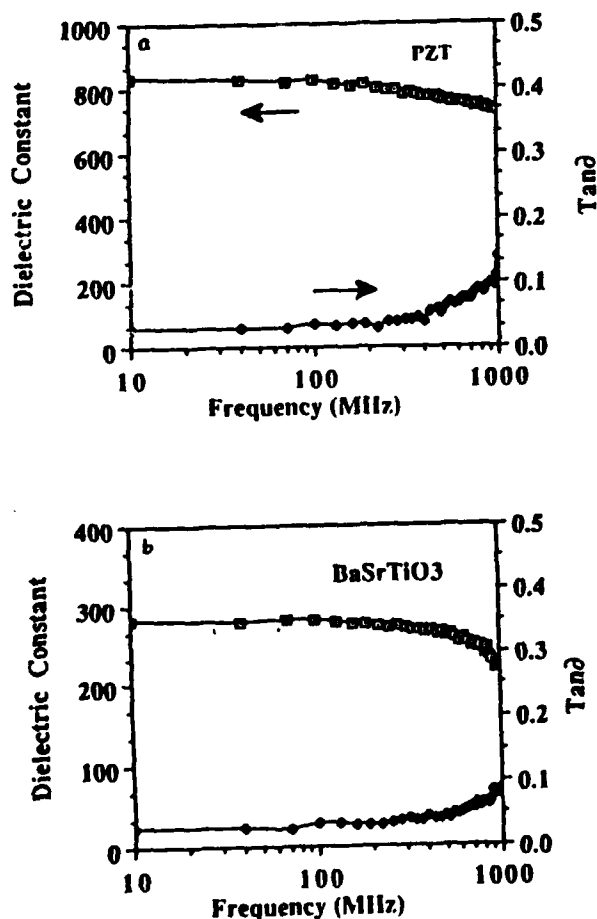


Fig. 6 The frequency characteristics of ferroelectric PZT films (a), and paraelectric BST films (b); note the non-dispersive behavior upto the measured frequency of 1 GHz by a careful control of the growth of the interface layer.

evidence of relaxation in films annealed at 500 to 600°C (Fig. 5); interface layer growth may thus be controlled to eliminate low frequency dielectric dispersion. Extending this theme, by manipulating the processing parameters, the low frequency dielectric permittivity and loss of the PZT films could be sustained upto a GHz, as shown in Fig. 6a. A solid solution system embracing compositions that is paraelectric at room temperature is the (Ba, Sr)TiO<sub>3</sub> (BST) system; specifically, thin films in the BST system, of composition corresponding to a Ba/Sr mole ratio of 50/50, fabricated by the sol-gel chemical technique, revealed dispersion-free dielectric characteristics (Fig. 6b) for measurements upto a GHz.

### Summary

Earlier studies of both bulk ceramics and thin films has shown that the utility of ferroelectrics for high frequency applications is limited on account of the dielectric dispersion at 1 MHz to a few hundred MHz depending on the specific material. The present endeavor has shown that by a delicate interplay of the processing parameters, dielectric relaxation in the PZT films can be prevented upto a GHz. Films that are ferroelectric at room temperature are *intrinsically* subjected to relaxation due to the piezoelectric clamping of grains or domains, and the inertial response of domain wall movement. It would therefore appear prudent to examine the feasibility of films that are paraelectric at room temperature for high frequency applications; Ba<sub>0.5</sub>Sr<sub>0.5</sub>TiO<sub>3</sub> falls in this category, and the first results are indeed promising.

### References:

- [1] J. Chen, K. R. Udayakumar, K. G. Brooks, and L. E. Cross, "Rapid thermal annealing of sol-gel derived PZT thin films", *J. Appl. Phys.*, pp. 4465-69, May 1992
- [2] K. R. Udayakumar, J. Chen, S. B. Krupanidhi, and L. E. Cross, "Sol-gel derived PZT thin films for switching applications", *Proc. Seventh Intl. Symp. Appl. Ferroelectrics*, 1990, pp. 741-43
- [3] M. Sayer, A. Mansingh, A. K. Arora, and A. Lo, "Dielectric response of ferroelectric thin films on non-metallic electrodes", *Integrated Ferroelectrics*, vol. 1, pp. 129-146, 1992.

**APPENDIX 37**

## PIEZOELECTRIC THIN FILM ULTRASONIC MICROMOTORS

K. R. UDAYAKUMAR, J. CHEN, K. G. BROOKS, L. E. CROSS,  
 A. M. FLYNN \*, AND D. J. EHRlich \*\*  
 Materials Research Laboratory, Pennsylvania State University, University Park, PA 16802  
 \* MIT Artificial Intelligence Laboratory, Cambridge, MA 02139  
 \*\* MIT Lincoln Laboratory, Lexington, MA 02173

### ABSTRACT

Thin films of lead zirconate titanate have been fabricated for application to a new family of flexure-wave piezoelectric micromotors that are characterized by low speed and high torque. The high relative dielectric constant and breakdown strength of the films lead to high stored energy densities. Evaluation of the film as a bimorph yielded a value of  $-88$  pC/N for the transverse piezoelectric strain coefficient,  $d_{31}$ ; the relevant electromechanical coupling factor,  $k_{31}$ , calculated thereupon was 0.22. The development of the piezoelectric ultrasonic micromotors from the PZT thin films, and the architecture of the stator structure are described. Nonoptimized prototype micromotors show rotational velocities of 100-300 rpm at drives of 3-5 V.

### INTRODUCTION

Recent investigations of ferroelectric thin film structures, largely devoted towards application in non-volatile random access memories (NVRAMs) and dynamic random access memories (DRAMs), have demonstrated that films of the lead-based perovskite-structured ferroelectric oxides can be deposited on both Si and GaAs substrates, and annealed to the proper ferroelectric crystalline form at temperatures generally compatible with their integration into IC fabrication. Specifically, thin films of lead zirconate titanate (PZT) of the morphotropic phase boundary composition have been shown to have dielectric permittivity and remanent polarization comparable to the bulk, but clearly superior dielectric breakdown strengths. In fact, the films exhibit more than an order of magnitude higher breakdown strengths than the bulk. With a relative dielectric constant of 1200-1300 and dielectric breakdown strengths of 1-2 MV/cm [1], depending on the film quality and microstructure, the maximum stored energy density at an applied voltage of 5 V across the film is about  $9 \times 10^5$  J/m<sup>3</sup>. This is calculated from the relation  $0.5\epsilon_r E_{bd}^2$ , where  $\epsilon_r$  represents the relative permittivity, and  $E_{bd}$  the breakdown strength. In comparison, a typical 100  $\mu$ m radial-gap variable-capacitance micromotor has a stored energy density of  $5 \times 10^4$  J/m<sup>3</sup>; this assumes a typical maximum voltage of 100 V applied across a rotor-stator gap of 1  $\mu$ m. This suggests the potential applicability of the PZT films in electromechanical devices, following the argument of Bart et al. [2] that the stored electric energy is a useful measure of an electromechanical transducer's ability to provide torque.

For a ferroelectric thin film with potentially high turning-power to be useful in applications involving vibration or motion, the films should be capable of being driven to large shape changes at quite low drive voltages. Mechanical strain can be induced by three mechanisms in a polycrystalline material: piezoelectricity, electrostriction, and antiferroelectric to ferroelectric phase switching. The first two mechanisms can be described phenomenologically in a homogeneous, polarizable, deformable, anisotropic solid, with polarization as the order parameter [3], by

$$\epsilon_{ij} = \epsilon_{ijkl} X_{kl} - b_{mij} P_m - Q_{mnij} P_m P_n$$

where  $x_{ij}$  are the components of the induced strain;  $X_{kl}$  the components of the applied stress;  $s_{ijk}$  the elastic compliance tensor;  $P_i$  the components of electric polarization;  $b_{mij}$  the piezoelectric tensor in polarization notation; and  $Q_{mnij}$  the electrostriction tensor in polarization form. In the equation above, if the stress is held constant,  $X_{kl}=0$ ; piezoelectric and electrostrictive effects evidently contribute to the polarization related strain. For ferroelectric materials, particularly the perovskite-structured oxides, the dielectric constants are high, enabling the inducement of very high levels of polarization and strain (in addition to the spontaneous polarization and strain) under realizable electric fields. It is this large strain that makes ferroelectrics an attractive option for actuator applications.

For a poled ferroelectric, the *piezoelectric* effect is the dominant electromechanical mechanism for field-induced strain; in bulk ceramics, compositions in the lead zirconate titanate system have been the most widely exploited. For any ferroelectric derived from a centrosymmetric point group in the paraelectric temperature range, field induced strain is contributed by the *electrostrictive* effect. Compositions close to the PMN end of the lead magnesium niobate (PMN)-lead titanate (PT) solid solution system, the best electrostrictors, are characterized by low magnitude of the polarization related electrostrictive coefficient,  $Q$ , but their high permittivity ensures the strain levels to be on par with those of the piezoelectrics. The strains achievable with the piezoelectric and electrostrictive materials are on the order of 0.01% to 0.1%. Certain compositions in the  $\text{PbZrO}_3$ - $\text{PbTiO}_3$ - $\text{PbSnO}_3$  ternary undergo an *antiferroelectric to ferroelectric phase switching*, and this constitutes the third mechanism of electromechanical transduction. This phase transition phenomenon is accompanied by large spontaneous polarization, giving rise to high volume expansion strain. Associated strains as large as 0.85% have been reported in this system [4].

In this study, we examine the strain resulting from the piezoelectric effect in PZT thin films, and explore its viability for the development of piezoelectric ultrasonic micromotors. Micromotors based on electrostrictive strains and switchable antiferroelectrics might warrant future study. Initial studies on electrostriction of anhysteretic La doped PZT (9/65/35) thin films [5], and films with phase change compositions of lead lanthanum zirconate stannate titanate [6] are reported in these proceedings.

For a poled PZT ceramic, that has a cylindrical polar symmetry  $\infty\text{mm}$ , there are three nonvanishing, independent piezoelectric coefficients,  $d_{33}$ ,  $d_{31}$  and  $d_{15}$  [7]. The transverse piezoelectric coefficient,  $d_{31}$ , relates the field along the polar axis to the strain perpendicular to it. The subscript 3 here refers to the poling axis, and 1 and 2 to the arbitrarily chosen orthogonal axes in the plane normal to the 3-axis. In the ultrasonic micromotor to be described, bending oscillations generate the elastic traveling wave, and it is  $d_{31}$  that is of relevance. We confine ourselves in the next section to the determination of this coefficient. A fuller evaluation of the piezoelectric constants has been undertaken in [8].

## PIEZOELECTRIC STRAIN COEFFICIENT

The PZT thin films chosen for this study were of the morphotropic phase boundary composition (with a Zr/Ti molar ratio of 52/48) that has demonstrated excellent piezoelectric properties in the bulk [9]. Films were deposited on [100] Si wafers with 0.15- $\mu\text{m}$ -thick Pt sputtered on a thermally grown  $\text{SiO}_2$  buffer layer. The films were fabricated by the sol-gel spin-on technique. The details of the procedure, along with the dielectric and ferroelectric properties, has been described previously [1].

The transverse piezoelectric coefficient,  $d_{31}$ , was measured with the aid of a modified Mach-Zehnder laser interferometer that has the capability to resolve an ac field induced displacement of the order of  $10^{-13}$  m [10]. The film was used as a piezoelectric flexure element, or bimorph, in which the film is considered to be bonded to the Si substrate. This bimorph was 5 mm long and 0.5 mm wide. The PZT film used was 0.38  $\mu\text{m}$  thick, and sputtered gold formed the top electrode. An ac field applied across its

conducting surfaces bends the film. The resulting displacement of the bimorph is plotted as a function of the amplitude of the ac field in Figure 1. For the metal-ceramic bimorph of the form considered here, the deflection  $D_e$  at the free end of a cantilever of length  $L$  and thickness  $h$ , on application of an electric field  $E$ , has been derived, using stress analysis [11], to be

$$D_e = \frac{3 d_{31} E L^2 (1+2\alpha) (1+\alpha)}{2 h (1+\alpha)^3 - \alpha^3 (1-\gamma)}$$

where  $\alpha = (t_f/2t_s)$ ,  $t_s$  being the thickness of the substrate,  $t_f$  that of the PZT film; and  $\gamma = s_{11f}/s_{11s}$ , with  $1/s_{11f}$  and  $1/s_{11s}$  representing the Young's moduli of the film and the substrate respectively ( $\gamma$  is approximately 6 here). For a very large ratio of the thickness of the substrate to that of the film ( $>10^3$  here), the above expression may be approximated by the following :

$$D_e = \frac{3 d_{31} E L^2}{2 h t_f \lambda_f}$$

From Figure 1, for a deflection of  $0.1 \mu\text{m}$ , the transverse piezoelectric coefficient,  $d_{31} = -88 \text{ pC/N}$ , a magnitude close to the reported value of  $-93 \text{ pC/N}$  of the bulk ceramic [9]. The Figure highlights the nonlinear nature of the transverse piezoelectric coefficient.

For ferroelectric PZT derived from centric prototypic symmetry,  $m3m$ , the piezoelectric constants of the ferroelectric domain are morphic, and specifically for the coefficient relating the strain measured in an orthogonal direction to that of the poled film (in the 3-direction) [3],

$$d_{31} = d_{32} = 2 Q_{12} P_3 \epsilon_{33} \epsilon_0$$

where  $Q_{12}$  represents the electrostrictive coefficient of the prototypic phase,  $P_3$  the polarization, and  $\epsilon_{33}$  the relative dielectric constant. For any system, the electrostrictive constants do not vary much with either composition or temperature, and thus the piezoelectric response depends primarily on the level of polarization and permittivity. Since the films have comparable values of  $P_3$  and  $\epsilon_{33}$  with that of the bulk ceramic, the consistency in the magnitude of the transverse piezoelectric coefficient with the bulk is not surprising.

The electromechanical coupling factors are a measure of the proportion of the electrical energy that can be stored elastically, and are dimensionless measures of the strength of the piezoelectric effects. The transverse electromechanical coupling factor,  $k_{31}$ , derived from the equations of state [9], is given by

$$k_{31} = d_{31} / (\epsilon_0 \epsilon_{33}^T s_{11}^E)^{0.5}$$

The dielectric and piezoelectric constants for the films are known from the discussion above. On the assumption that the elastic coefficient of the bulk PZT holds for the films ( $s_{11}^E = 13.8 \times 10^{-12} \text{ m}^2/\text{N}$ ),  $k_{31}$  was calculated from the equation above to be 0.22.

#### MICROMOTOR DEVELOPMENT

An extensive description of the major advantages of ultrasonic drives for micromotors, and the initial design for the stators of linear and rotary motors has been presented by Flynn et al. [12]. They are essentially based on the principles of commercially available ultrasonic motors in Japan that convert electrical energy to mechanical energy through piezoelectric interaction [13,14]. Our contribution has been to realize that with PZT thin films, these motors could be driven at lower voltages. With the addition of lithography techniques, the features could also be much finer, with the ensuing possibilities for batch fabrication. Ultrasonic motors require alternately driven segments arranged in such a way that the application of two high frequency waveforms shifted in phase both spatially and temporally generates a bending traveling wave in the body.

Traveling waves in beams induce particle motion at the surface which is elliptical. Any rotor or carriage frictionally pressed against such a vibratory stator is dragged away. A SEM cross section of the micromotor stator structure is shown in Figure 2. To fabricate this,  $1\ \mu\text{m}$  of low-stress silicon-rich silicon nitride, that acts as both a membrane and the mask for the tetra methyl ammonium hydroxide (TMAH) anisotropic etch, was deposited on silicon wafers. These wafers were back-side etched to form diaphragms over several millimeters square. A  $0.46\ \mu\text{m}$ -thick platinum layer was then deposited on these diaphragms to form a nonoxidizing ground plane, with a 20-nm-thick titanium layer for the adhesion of Pt to the nitride diaphragm. The PZT films were then fabricated by the sol-gel spin-on technique. The upper stator electrodes were gold, patterned by the standard lift-off process. The whole assembly of the stator electrode pattern, along with a 1.5-mm-diameter plano-convex glass lens as the rotor, is shown in Figure 3. No rotors or bearings were etched in place.

Although designed to require four-phase excitation, rotary motion of the glass rotor was demonstrated with single-phase excitation for a 3 to 5 V peak-to-peak drive signal at approximately 90 kHz. Typical rotational velocities of the glass lens were on the order of 100-300 rpm. Preliminary results yield a net normalized torque, based on the net acceleration of the rotor, of  $1.6 \times 10^{-12}\ \text{N}\cdot\text{m}/\text{V}^2$ ; this is significantly larger in comparison with  $1.4 \times 10^{-15}\ \text{N}\cdot\text{m}/\text{V}^2$ , a value reported for some electrostatic micromotors [15]. We used only single-phase excitation due to yield problems in the films when needing to cover the large areas required for motor electrodes. This rotary motion is assumed to be the result of coupling to the standing wave vibration patterns. It is believed that the coupling will improve significantly when a true traveling wave excitation can be applied. Furthermore, gravity is the only normal force acting between the rotor and the stator in this system, again yielding nonoptimized mechanical coupling.

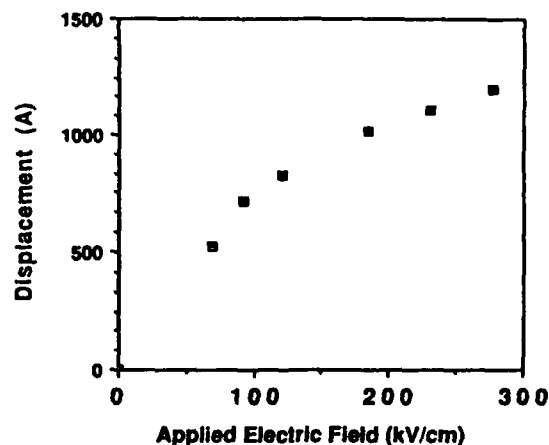


Fig. 1 The film is used as a piezoelectric flexure element to measure  $d_{31}$ . Recorded above is the displacement of the bimorph on application of an ac field, constituting the raw data for calculating  $d_{31}$ .

## CONCLUSIONS

In this work, based on demonstrated high energy density, accruing from the high relative dielectric constant (1300) and breakdown strength (1 MV/cm), we set out to examine the magnitude of the piezoelectric strain that generates an elastic traveling wave in

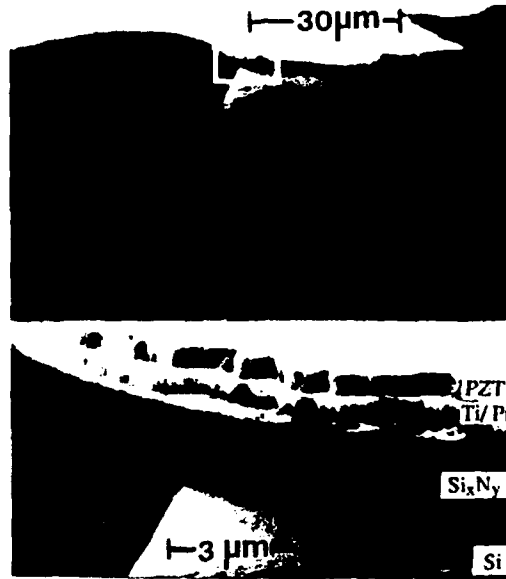


Fig. 2 The SEM photograph above is a cross section of the PZT micromotor structure. Note that the bottom portion of the micrograph is the enlarged view of the top portion.

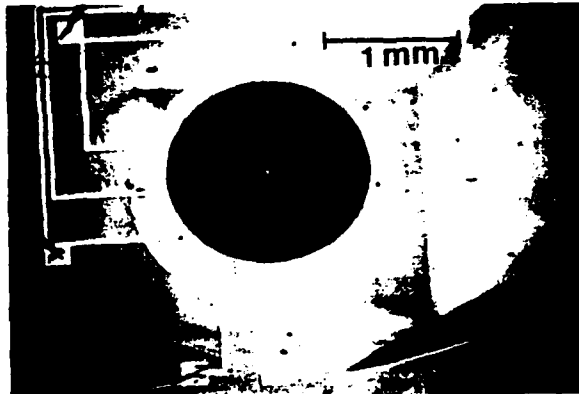


Fig. 3 A plano-convex lens of 1.5 mm diameter placed atop the 8-pole rotary stator, as shown in this figure, spins at a velocity of 100-300 rpm for a 3-5 V peak to peak drive signal at approximately 90 kHz.

the film. It was found that the transverse piezoelectric coefficient of  $-88 \text{ pC/N}$  closely parallels that of the bulk ceramic of equivalent composition; the corresponding electromechanical coupling factor was 0.22. We incorporated these sol-gel PZT films into a prototype microstator for an ultrasonic motor, and observed rotational velocities of 100-300 rpm in a glass lens, that served as a rotor, at low drive voltages. This investigation has shown that the ferroelectric thin films in combination with silicon micromachining are very promising for micromotor development. The next phase of our study will focus on device design, boundary conditions, new material systems and methods of increasing yield for the large areas required for actuators.

#### ACKNOWLEDGMENTS

The authors gratefully acknowledge the financial support received in part from the Gnat Robot Corporation and in part from the University Research Initiative under Office of Naval Research contract N00014-86-K-0685. The Lincoln Laboratory portion of this work was supported by the Department of the Air Force, in part by a specific program from the Air Force Office of Scientific Research. We are indebted to Chester A. Bukowski, who performed much of the metallization and other fabrication at Lincoln Laboratory.

#### References

- [1] K.R. Udayakumar, J. Chen, S.B. Krupanidhi, and L.E. Cross, Proceedings of the 7th International Symposium on Application of Ferroelectrics (in press)
- [2] S.F. Bart, T.A. Lober, R.T. Howe, J.H. Lang, and M.F. Schlecht, *Sensors and Actuators*, **14** (3), 269 (1988).
- [3] M.J. Haun, E. Furman, S.J. Jang, and L.E. Cross, *Ferroelectrics*, **99**, 13 (1989)
- [4] W.Y. Pan, Q.M. Zhang, A. Bhalla, and L.E. Cross, *J. Amer. Cer. Soc.*, **72** (4), 571 (1989)
- [5] J. Chen, K.R. Udayakumar, K.G. Brooks, and L.E. Cross, this Symposium Proceedings
- [6] K.G. Brooks, J. Chen, K.R. Udayakumar, and L.E. Cross, this Symposium Proceedings
- [7] J.F. Nye, *Physical Properties of Crystals* (Oxford University Press, Oxford, 1985), p.296
- [8] K.R. Udayakumar, S.F. Bart, A.M. Flynn, J. Chen, L.S. Tavrow, L.E. Cross, R.A. Brooks, and D.J. Ehrlich, Proceedings of the 4th IEEE Workshop on Micro Electro Mechanical Systems, edited by H. Fujita and M. Esashi (IEEE, NY, 1991), p. 109
- [9] B. Jaffe, W.R. Cook and H. Jaffe, *Piezoelectric Ceramics* (Academic Press, NY, 1971), p. 29, 146
- [10] Q.M. Zhang, W.Y. Pan, and L.E. Cross, *J. Appl. Phys.*, **63** (8) 2492 (1988)
- [11] J.M. Herbert, *Ferroelectric Transducers and Sensors*, vol. 3 (Gordon and Breach Science Publishers, NY, 1982), p. 227
- [12] A.M. Flynn, L.S. Tavrow, S.F. Bart, R.A. Brooks, D.J. Ehrlich, K.R. Udayakumar, and L.E. Cross, Proceedings of the IEEE Ultrasonics Symposium, edited by B.R. McAvoy (IEEE, NY, 1990), p. 1163
- [13] R. Inaba, A. Tokushima, O. Kawasaki, Y. Ise and H. Yoneno, Proceedings of the IEEE Ultrasonics Symposium, 747 (1987)
- [14] Y. Akiyama, *JEE*, April 1987
- [15] S.F. Bart, M. Mehregany, L.S. Tavrow, J.H. Lang, and S.D. Senturia, *Microstructures, Sensors and Actuators*, ASME, DSC-vol. 19, 19 (1990).